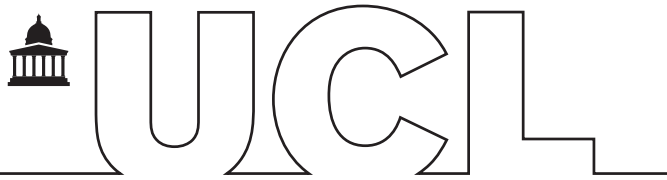

Correlated three-electron ionization in strongly-driven atoms and molecules

Matthew Peters

A dissertation submitted in partial fulfillment

of the requirements for the degree of

Doctor of Philosophy

of

University College London.

Department of Physics and Astronomy

University College London

October 2023

I, Matthew Peters, confirm that the work presented in this thesis is my own. Where information has been derived from other sources, I confirm that this has been indicated in the work.

Abstract

We develop a theoretical model to study correlated three-electron ionization. We examine the strongly-driven linear triatomic molecule HeH_2^+. To account for unphysical autoionization where one bound electron collapses into the nucleus exchanging infinite energy with another bound electron, we turn off the Coulomb force between any pair of bound electrons. Also, we construct an algorithm to determine on the fly during time propagation when an electron is bound or quasifree. This model can address double and triple ionization but cannot describe processes involving two bound electrons. Hence, we cannot address frustrated double ionization with one ionizing electron, one deeply bound electron and another electron in a Rydberg state. These limitations led us to develop a sophisticated model that accounts for the interaction of any pair of bound electrons via effective potentials. The interaction between any pair of quasifree and bound electrons as well as between quasifree electrons is described by the full Coulomb forces. We do so by introducing a set of criteria that identifies on the fly during time propagation when an electron is bound or quasifree. The results provided by our model for the momenta distributions for triple and double ionization of strongly driven Ar and Ne have very good to excellent agreement with experimental results, unlike previous models. Currently our model is the most accurate one for describing multi-electron ionization in strongly driven atoms. Finally, we investigate non-dipole effects in the correlated multi-electron ionization of Ar and Ne. We identify a positive momentum offset in the average sum of the final electron momenta along the direction of light propagation. We find that the magnitude of this momentum offset probes the strength of a recollision, i.e. the strength of electron-electron correlation, during multi-electron

ionization.

Impact Statement

This dissertation studies the interaction of intense ultra-fast laser pulses with three-electron atoms and molecules. Theoretical models that allow for the study of three electrons in strongly driven systems are few and involve approximations such as using soft-core potentials or accounting for only one dimension. In order to avoid such approximations, we develop a sophisticated 3D model that fully accounts for the Coulomb singularity while propagating any number of electrons in atoms driven by laser fields. In this work, we demonstrate the accuracy of our new model that employs an effective Coulomb potential for bound-bound electrons (ECBB model) by comparing it to the existing Heisenberg core potential method (H Model). We provide evidence for the superiority of the ECBB model compared to the H model by examining Ar and Ne driven by intense laser fields. That is, we compare the triple and double ionization momenta distributions obtained using both these models against experiment and find that the ECBB model has very good agreement with experiment. Furthermore, we employ our model to investigate non-dipole effects in strongly driven Ar and Ne. Our results show that non-dipole effects are present in correlated multi-electron ionization even at intermediate laser intensities. That is, we find a positive momentum offset in the average sum of the final electron momenta along the direction of light propagation. This momentum offset is related to the magnetic field of the laser pulse and its value depends on the strength of electron-electron recollisions. In summary, studying strongly driven atoms and molecules with three or more electrons is currently out of reach for 3D quantum mechanical techniques. Therefore, this work provides a solid foundation for the theoretical study of strongly driven systems with three of more electrons that can-

not yet be accurately addressed by other theoretical techniques. Furthermore, most of our results can be experimentally measured and tested and therefore our work will motivate future studies of strongly driven systems.

Acknowledgements

Firstly, I would like to thank my supervisor Prof. Agapi Emmanouilidou, for her help in keeping me focused on my own project and not getting sidetracked into a completely different field. I would also like to thank all the members past and present of our research group for many discussions, which were always entertaining and sometimes productive. I am thankful to all my friends in Ireland and in London for putting up with me these last four years. Finally, I am grateful to my family for supporting and encouraging me throughout my entire academic journey.

List of Publications

This dissertation is based on the following publications.

[1] Peters, M. B. and Majety, V. P. and Emmanouilidou, A. Triple ionization and frustrated triple ionization in triatomic molecules driven by intense laser fields. *Physical Review A*, **103**, 043109 (2021).

[2] Peters, M. B. and Katsoulis, G. P. and Emmanouilidou, A. General model and toolkit for the ionization of three or more electrons in strongly driven atoms using an effective Coulomb potential for the interaction between bound electrons. *Physical Review A*, **105**, 043102 (2022).

[3] Emmanouilidou, A. and Peters, M. B. and Katsoulis, G. P. Singularity in the electron-core potential as a gateway to accurate multielectron ionization spectra in strongly driven atoms. *Physical Review A*, **107**, L041101 (2023).

[4] Katsoulis, G. P and Peters, M. B. and Emmanouilidou, A. Nondipole electron momentum offset as a probe of correlated three electron ionization in strongly driven atoms. *arXiv*, (2023). (Recently accepted by Physical Review A)

Contents

List of Figures

List of Tables

Chapter 1

Introduction

Attosecond science has grown rapidly in recent years since the advent of the experimentally obtainable attosecond pulse. The ability to produce attosecond pulses [1] [5–7] has enabled experimentalists to begin investigating the motion of electrons on their natural timescale. Numerous review articles have been published detailing the advances of this field over recent years [8–11]. These reviews highlight how attosecond pulses can be used for investigating many electron systems, electron correlation effects, electronic motion in complex systems and ultrafast charge migration in complex molecules. Such advances in experimental technology are a motivation for this current work. That is, theoretical models to accurately account for multi-electron effects in strongly driven systems are currently out of reach for quantum mechanical studies. Hence, this work is focused on developing and testing an accurate semi-classical model which can account for multi-electron ionization in strongly driven atoms.

Our work is based on the theoretical foundation which underlies Attosecond science [12], namely, the three-step model. This model, as per its name, describes light-matter interaction in a series of three steps. In step one, an electron escapes from its parent ion either via tunnel ionization through the field lowered Coulomb potential barrier or above-the-barrier ionization, i.e. the field lowered Coulomb barrier is sufficiently low for the electron to scape without tunnelling. In the second step, the electron is driven by the laser field and can be described classically. Finally,

[1] 1 attosecond (as) = 10^{-18} second.

in step three, the electron moves under the influence of the laser field possibly returning to the parent ion and multiple outcomes can occur. Namely, (i) the electron recombines with the parent ion resulting in the emission of photons, which is known as high-order harmonic generation (HHG) [12]; (ii) the electron recollides with the parent ion and transfers energy to a bound electron leading to multi-electron ionization. This results in nonsequential ionization [13], the main process that is examined in our model.

While nonsequential double ionization (NSDI) has been studied extensively both theoretically and experimentally [14, 15], three-dimensional (3D) quantum mechanical studies still remain quite challenging [16–18]. For nonsequential triple ionization (NSTI), only few theoretical studies exist, mostly formulated in the dipole approximation. For NSTI, most studies employ lower dimensionality classical [19, 20] and quantum mechanical [21, 22] models to reduce the complexity and computational resources required. However, lower dimensionality results in a non accurate description of electron-electron interaction during triple ionization. Currently, only classical or semiclassical 3D models of NSTI are available [20, 23–26]. In this thesis, we argue that the main disadvantage of available classical and quantum models of NSTI is their softening of the interaction of each electron with the core. This results in ionization spectra that differ from experimental ones obtained, for instance, for driven Ne and Ar [27–33]. Indeed, the ratio of the scattering amplitude for the soft-core potential over the one for the Coulomb potential decreases exponentially with increasing momentum transfer [34, 35]. For recollisions [12], this implies that soft potentials are quite inaccurate for high energy recolliding electrons that backscatter. Hence, it is no surprise that classical models that include the singularity in the Coulomb electron-core potential result in accurate double ionization spectra. Indeed, with a classical model for driven two-electron atoms [36], the predecessor of the model of nonsequential multi-electron ionization (NSMI) discussed here, it was shown that backscattering of the recolliding electron from the core gives rise to the finger-like structure in the two electron correlated momenta of driven He [16, 37, 38]. This same model was used to obtain double ionization spectra in very

good agreement with an *ab initio* quantum mechanical calculation for driven He [39] and with an experiment for Ar driven by near-single cycle laser pulses [40]. Moreover, this model was used to identify the striking slingshot-NSDI mechanism where the exact treatment of the electron-core interaction is of paramount importance [41].

Concerning NSTI, for quantum mechanical models, softening the Coulomb potential of each electron with the core affords a computationally tractable problem. For classical and semiclassical models, the reason is fundamental and concerns unphysical autoionization. By unphysical autoionization we mean the following: classically there is no lower energy bound. Hence, when a bound electron undergoes a close encounter with the core, the singularity in the Coulomb potential allows this electron to acquire a very negative energy. This can lead to the artificial escape of another bound electron through the Coulomb interaction between bound electrons. Despite this, we choose to account for the singularity in the Coulomb potential between each electron and the core. To avoid autoionization we use effective Coulomb potentials to account for the interaction of a bound-bound electron pair [2]. The Coulomb potential between each pair of a quasifree and a bound electron and hence the transfer of energy from a quasifree to a bound electron is treated exactly. Here, we have assigned two possible states to electrons, quasifree or bound. Quasifree refers to a recolliding electron or an electron escaping to the continuum, whereas bound refers to an electron attached to a nucleus. In our calculations, propagation begins with one tunnel ionized electron which is set to be quasifree and two bound electrons. We decide on the fly with a set of sophisticated criteria whether an electron changes state from quasifree to bound or vice-versa. Hence, we allow the interaction between pairs of electrons to change smoothly during time propagation between the Coulomb potential and effective potentials. In our initial work on HeH_2^+ [1] we avoided autoionization by turning off the force between pairs of bound electrons. However, this did not account for electron-electron screening, and our results were limited to only accurately describing the cases where one or less electrons remained bound at the end of time propagation.

In this thesis, we provide a general three-dimensional (3D) classical model of NSMI developed in the nondipole framework. Taking also into account the spatial dependence of the vector potential $\mathbf{A}(\mathbf{r},t)$ and consequently accounting for the magnetic field, $\mathbf{B}(\mathbf{r},t) = \nabla \times \mathbf{A}(\mathbf{r},t)$, adds to the computational difficulty. Hence, most theoretical studies are formulated in the dipole approximation. However, to fully explore ionization phenomena and identify nondipole effects in driven atoms and molecules one needs to account for the Lorentz force $\mathbf{F_B} = q\mathbf{v} \times \mathbf{B}$ exerted on particles of charge q moving with velocity $\mathbf{v}$. Magnetic field effects have been previously identified in a wide range of processes. For example, in stabilization [42], in high-harmonic generation [43–45], and in multielectron ionization probabilities of Ne [46], with observable effects found only for intensities two orders of magnitude larger than the ones considered in the current work. For the largest intensity we consider in this thesis, we find that the amplitude $\beta_0 \approx U_p/(2\omega c)$ of the electron motion due to $\mathbf{F_B}$ is roughly 0.2 a.u., instead of the expected 1 a.u. [47, 48], where U_p is the ponderomotive energy.

Using this model, for nonsequential triple ionization of strongly driven Ne, we obtain triple ionization spectra [3] in excellent agreement with experiment [28]. Moreover, we find a significant positive momentum offset of the average sum of the final electron momenta along the direction of light propagation. This offset is found to be much larger than what we would have expected in single ionization. We identify the change in momentum due to the magnetic field as the main source for this positive momentum offset. Furthermore, for the recolliding electron, we find that the momentum change due to the magnetic field is related with the sharp change in momentum during recollision. Also, for both the recolliding and bound electrons, we find that the momentum change due to the magnetic field is related to the time that the recollision takes place. This differs from what has been previously encountered in nonsequential double ionization of strongly driven atoms [49, 50]. In these latter studies, the magnetic field jointly with a recollision act as a gate that allows for double ionization to occur only for a subset of the initial momenta of the recolliding electron along the direction of light propagation. For the case of strongly driven

He at high intensities, it has been shown that the recollisions involved are glancing ones. As a result, the recolliding electron just before recollision is accelerated by the Coulomb attraction from the core resulting in the light-propagation-direction component of the average sum of the final electron momenta being large and positive [49, 50]. Our studies on dipole-effects will also hopefully motivate new studies about how momentum is shared between the nuclei and electrons during tunnelling as this is needed when using our model to set up the initial conditions.

Our model is currently set up for atoms with any number of electrons, however it can be extended to molecules. It should have a strong impact, since there are no other models in this field which result in good agreement with experiment.

Chapter 2

Triple ionization and frustrated triple ionization in the triatomic molecule HeH_2^+ driven by intense laser fields

In this chapter, we formulate a three-dimensional semiclassical model to treat three-electron escape dynamics in a strongly driven linear triatomic molecule, HeH_2^+ [1]. Our model includes the Coulomb singularities. Hence, to avoid unphysical autoionization, we employ two criteria to switch off the Coulomb repulsive force between two bound electrons and switch it on when the motion of one electron is mostly determined by the laser field. Thus, we do not account for screening when two electrons are bound. In the following chapters we present a more general model which takes this screening into account. Here, we investigate triple and "frustrated" triple ionization. In the latter process two electrons escape while one electron remains bound in a Rydberg state. We find that two pathways prevail in "frustrated" triple ionization, as in "frustrated" double ionization [51]. We also find that the electron that remains in a Rydberg state is more likely to be attached to He^{2+} compared to H^+. Our results indicate that in triple and "frustrated" triple ionization electronic correlation is weak, when He^{2+} is driven by long pulses, such as the 40fs pulse considered in this chapter. Moreover, we compute the sum of the kinetic energies as well as the angular patterns of the final ion fragments in triple and "frustrated" triple ionization. These patterns suggest that the fragmenting molecule deviates from its

initial linear configuration.

2.1 Introduction

Correlated multi-electron escape dynamics arising in systems driven by intense infrared and mid-infrared laser fields is a problem of fundamental interest. The complexity of the problem, currently, limits ab-initio quantum mechanical computations in three dimensions to two-electron escape in strongly-driven atoms [16, 17, 52, 53]. This latter problem has also been addressed by three-dimensional quantum mechanical [17] and semiclassical techniques [36, 36, 54] that include the Coulomb singularity. Given the even larger degree of complexity, strongly-driven three-electron dynamics has been addressed in few theoretical [19, 21, 24, 55] and experimental studies [27, 31]. More relevant to the current work is the classical study of driven trimers in ref. [55] with three atoms placed far apart and each electron being bound to a different atom. The work in ref. [55] does not address the unphysical autoionization that occurs in a classical treatment of two bound electrons when the Coulomb singularities are included. One electron can acquire a very negative energy and release energy that leads to the escape of the other bound electron. This does not occur quantum mechanically, since the energy of an electron has a lower bound. This unphysical autoionization is addressed in this semiclassical work that includes the Coulomb singularities and involves two bound electrons.

Here, we develop a three-dimensional (3D) semiclassical model to investigate three electron dynamics in strongly-driven triatomic molecules. We do so in the context of the strongly-driven linear molecule HeH_2^+. This model is an extension to the 6-body Coulomb problem of the model that was developed to describe, first, H_2 [51, 56], and, then, D_3^+ [57] when driven by intense laser fields. Treating unphysical autoionization is an aspect of our model introduced in this work. The latter arises since we fully account for the Coulomb singularities and in HeH_2^+ more than one electron can be bound.

Using this 3D semiclassical model, we account for triple and double ionization as well as for "frustrated" triple ionization. "Frustrated" ionization involves the

formation of Rydberg states. Namely, an electron first tunnel ionizes in the driving laser field. Then, due to the electric field, this electron is recaptured by the parent ion in a Rydberg state [58]. In "frustrated" double ionization (FDI) an electron is ionized while another one remains bound in a Rydberg state at the end of the laser pulse. "Frustrated" double ionization accounts for roughly 10% of all ionization events. Hence, FDI is a major process in the breakup of strongly-driven molecules. It has been addressed in experimental studies of H_2 [59], D_2 [60] and of the two-electron triatomic molecules D_3^+ and H_3^+ [61–63].

Two pathways account for "frustrated" double ionization in strongly-driven two-electron diatomic and triatomic molecules [51, 56, 64]. In both pathways, one electron tunnel ionizes early on (first step), while the remaining bound electron ionizes later in time (second step). In pathway A it is the second step that is frustrated, i.e. the initially bound electron does not escape but remains bound in a Rydberg state [51]. In pathway B it is the first step that is frustrated, i.e. the initially tunneling electron is captured in a Rydberg state [56]. Also, electron-electron correlation, which can underlie pathway B [51, 64], can be controlled with orthogonally polarised two-color linear laser fields [65, 66]. Furthermore, significant enhancement of pathway B of FDI with no electronic correlation is achieved when driving triatomic molecules with counter-rotating two-color circular laser fields [67]. It was shown that this is due to the electron that tunnel-ionizes first "hovering" around the nuclei. This feature is most prevalent when 800 nm and 400 nm laser fields are employed with a field-strength ratio equal to two [67]. In addition, fingerprints of nuclear motion on the electron dynamics have been previously identified in "frustrated" double ionization [68, 69]. Such a signature includes an oscillation in the principal n quantum number [68].

In this chapter, we address "frustrated" triple ionization (FTI) where two electrons escape while one remains bound in a Rydberg state. We identify the pathways of "frustrated" triple ionization and compute the principle n quantum number in FTI. Moreover, we compute triple as well as double ionization and discuss the role that correlation plays in the three- and two-electron escape. We also compute the

MRCI	CI	HF	Literature MRCI [70]		Units
-3.518	-3.518	-3.471	-3.519	electronic energy	a.u.
2.075	2.075	2.068	2.075	H-H equilibrium distance	a.u.
1.935	1.934	2.055	1.931	H-He equilibrium distance	a.u.

Table 2.1: Geometric positions of the nuclei at the equilibrium distance of the ground state of H_2He^+ using the Hartree-Fock SCF, CI and MRCI methods. These positions are obtained using MOLPRO with the aug-cc-pV5Z basis set. Our results are compared to the results given in Ref. [70] which employs the MRCI method with a cc-pV5Z basis set.

distributions of the kinetic energy release and of the angles of the final ion fragments in all three ionization processes.

2.2 Model

In this section, we describe in detail the different steps required to set up the initial conditions for a given classical trajectory as well as propagate all particles involved using Hamilton's equations of motion [1]. In what follows, the three nuclei are labelled as particles 1,2 and 3, and the three electrons as particles 4,5 and 6.

2.2.1 Electric field

We use a linearly polarized electric field along the z axis. This is given below

$$\mathbf{E}(t) = E_0 \exp\left[-2\ln 2\left(\frac{t}{\tau}\right)^2\right]\cos\omega t\,\hat{z}, \tag{2.1}$$

where τ is the full width at half maximum of the pulse duration in intensity, E_0 is the electric field strength and ω is the frequency of the laser pulse.

2.2.2 Initial conditions of the three electrons

2.2.2.1 Nuclei

In the initial state of HeH_2^+, all three atoms are placed along the z-axis. The two hydrogen atoms are at -3.09 a.u. and -1.02 a.u., respectively, and the helium atom is at 1.04 a.u. We refer to H farther away from He as left H and the one closest to He as middle H. We find these distances by using MOLPRO [71], a quantum chemistry package, by trying various methods to minimize the energy of HeH_2^+. A comparison between the different methods can be seen in Tab. 2.1. These methods include,

Hartree-Fock, Configuration Interaction(CI) and Multireference Configuration interaction (MRCI). We have used the Hartree-Fock method with the aug-cc-pV5Z basis set. The Hartree-Fock method overestimates by a small amount the distance between the hydrogen and the helium atoms, while the distances we find using the CI and MRCI methods are very close to the ones obtained in Ref. [70]. However, we employ the Hartree-Fock method for consistency with the Hartree-Fock wavefunctions that we use in the potential energy terms involved in computing the exit point of the tunnel-ionizing electron [56]. We initialise the nuclei at rest. Our studies suggest that an initial predissociation does not significantly alter the ionization dynamics [56].

2.2.2.2 Ionization rates

A quantum-mechanical technique is employed to compute this ionization rate. Specifically, the alignment-dependent tunnel-ionization rate for HeH_2^+ is obtained by employing the hybrid anti-symmetrized coupled channels (haCC) method described in ref. [72, 73]. In haCC, the system is represented in a basis of neutral and single ionization channel functions. The ground state of HeH_2^+ and the energetically lowest few HeH_2^+ states are obtained from the quantum chemistry package COLUMBUS [74]. A purely numerical basis is used to represent the tunneling electron, while anti-symmetrization is fully enforced. Exterior complex scaling is employed in order to obtain tunnel-ionization rates.

2.2.2.3 Importance sampling

We start each trajectory at time t_0, the time at which an electron has tunnel ionized through the field-lowered Coulomb potential. We find t_0, using importance sampling [75] in the time interval [-2τ,2τ] where the electric field is non-zero; τ is the full width at half maximum of the pulse duration in intensity. The integral of the field dependent ionization rate $\Gamma(E(t))$, which is obtained with the haCC method [72, 73], over the partial duration of the pulse is

$$W(t) = \int_{-2\tau}^{t} \Gamma(E(t))dt. \tag{2.2}$$

We obtain t_0 by sampling a random weight, W_{sample}, in the interval $[0, W(2\tau)]$ and then numerically solving the equation $W(t_0) = W_{sample}$ for t_0.

2.2.2.4 Exit Point

In the three-step model, an electron first tunnel ionizes at time t_0. We assume that the electron tunnel ionizes along the direction of the field [56] . We compute, $I_{p,1}$, the first ionization energy of HeH_2^+ with MOLPRO and find it equal to 1.02 a.u. We find that the threshold of the field strength for over-the-barrier ionization is equal to 0.087 a.u. Thus, in what follows, we only consider below the barrier ionization. The exit point is found by solving the equation below for $r_{4,||}$ the component of $\mathbf{r}_4$ along the direction of the field, while setting equal to zero the component of $\mathbf{r}_4$ perpendicular to the field

$$\begin{aligned} V\left(r_{4,||}, t_0\right) = & \frac{Q_1 Q_4}{|\mathbf{r}_4 - \mathbf{r}_1|} + \frac{Q_2 Q_4}{|\mathbf{r}_4 - \mathbf{r}_2|} + \frac{Q_3 Q_4}{|\mathbf{r}_4 - \mathbf{r}_3|} + 2\int \frac{|\Psi(\mathbf{r}_5)|^2}{|\mathbf{r}_4 - \mathbf{r}_5|} d\mathbf{r}_5 \\ & + \mathbf{r}_4 \cdot \mathbf{E}(t_0) = -I_{p,1} \end{aligned} \tag{2.3}$$

where $\mathbf{r}_i$ is the position vector of particle i, Q_i is the charge of particle i, $\Psi(\mathbf{r}_5)$ is the $1\sigma_g$ wave function of HeH_2^{++} at the equilibrium distances of HeH_2^+ which we obtain via MOLPRO [71]. Note that labels 1,2,3 are used for the ion cores, while label 4 is used for the electron that tunnels in the initial state and 5 for the electron that is bound in the initial state. We use the Hartree-Fock method with the aug-cc-pVTZ basis to expand the wavefunction $\Psi(\mathbf{r}_5)$ in terms of s-symmetry Gaussian functions. This is a very good approximation for the tunneling distances considered in the below the barrier regime for this molecule. The factor of 2 in the electron coulomb interaction term is present since there are two bound electrons in the $1\sigma_g$ orbital with opposite spin. The electron momentum is taken to be equal to zero along the polarisation direction of the laser field. The transverse momentum is given by a Gaussian distribution which represents the Gaussian-shaped filter with an intensity-dependent width arising from standard tunneling theory [76–78]. The weight for the recolliding electron to have a transverse velocity equal to $v_\perp$ at time

t_0 is denoted by W_i and is given by

$$W_i \propto \frac{v_\perp}{|\mathbf{E}(t_0)|} \exp\left(-\frac{v_\perp^2\,\kappa}{|\mathbf{E}(t_0)|}\right). \tag{2.4}$$

with $\kappa = \sqrt{2I_{p,1}}$.

2.2.2.5 Microcanonical distribution

We use a microcanonical distribution to determine the initial positions and momenta of the bound electrons (electrons 5 and 6). The technique used here is the same as that in Ref. [79]. For the molecule HeH_2^+ the only difference is that we consider a linear triatomic molecule, and also that we have two bound electrons rather than one. In this case, we begin propagation with the Coulomb force turned off between the pair of bound electrons. Therefore, the microcanonical distributions for the two electrons are independent of each other and each reduces to the microcanonical for a single electron given below, see [79],

$$f(\mathbf{r},\mathbf{p}) = \mathcal{N}\delta\left[-I_{p,2} - \frac{\mathbf{p}^2}{2} - W(\mathbf{r},\mathbf{p})\right] \tag{2.5}$$

with $\mathcal{N}$ a normalisation constant and $W(\mathbf{r},\mathbf{p})$ the total potential felt by a bound electron with respect to the three nuclei of HeH_2^+. Each electron is assigned an energy equal to 2.21 a.u. ($-\frac{I_{p,2}+I_{p,3}}{2}$) which is half the ground state energy of HeH_2^{2+}. Hence, in the initial state, electronic correlation is only indirectly taken into account via the energies considered in the microcanonical distributions.

2.2.3 Tunneling during propagation

We employ the Wentzel-Kramers-Brillouin approximation to allow each electron to tunnel during time propagation at the classical turning points along the axis of the field with a quantum-mechanical probability [51, 56, 64, 68]. Hence, in our otherwise classical model, we allow for tunneling with a semiclassical formula. This is the reason that we refer to our model as semiclassical. Allowing for tunneling during time propagation ensures that we accurately compute enhanced ionization [80–84]. Indeed, in enhanced ionization of molecules at a critical distance between

the nuclei a double potential well is formed which allows for an electron to tunnel more effectively from the higher potential well to the lower one and then to the continuum. The WKB transmission probability allows us to describe the tunneling that takes place from the higher potential to a lower potential well in enhanced ionization. This probability through a potential barrier is given below

$$\mathrm{T} \approx \exp\left(-2\int_{\mathrm{r_a}}^{\mathrm{r_b}} \left[2\left(\mathrm{V_{tun}}\left(\mathrm{r},\mathrm{t_{tun}}\right)-\varepsilon_{\mathrm{n}}\right)\right]^{1/2}\mathrm{dr}\right) \tag{2.6}$$

with $\mathrm{V_{tun}}\left(\mathrm{r},\mathrm{t_{tun}}\right)$ the potential along the field direction of each electron in the presence of the nuclei and the laser field, ε_n the energy of an electron at the time of tunneling, $\mathrm{t_{tun}}$, and $\mathrm{r_a}$ and $\mathrm{r_b}$ the classical turning points. Regarding enhanced ionization, when the nuclei are at a critical distance, a double-potential well is formed such that it is easier for an electron bound to the higher potential well to tunnel to the lower potential well and then ionize.

2.2.4 Global regularisation

We perform a global regularisation to avoid any numerical issues arising from the Coulomb singularities [85]. For strongly-driven H_2, this regularisation scheme was previously used to study double and "frustrated" double ionization within the dipole approximation [56] as well as non-dipole effects in non-sequential double ionization [86]. In this scheme, we define the relative position between two particles i and j as

$$\mathbf{q}_{\mathrm{ij}} = \mathbf{r}_{\mathrm{i}} - \mathbf{r}_{\mathrm{j}} \tag{2.7}$$

and

$$\boldsymbol{\rho}_{\mathrm{ij}} = \frac{1}{\mathrm{N}}\left(\mathbf{p}_{\mathrm{i}} - \mathbf{p}_{\mathrm{j}} - \frac{\mathrm{m_i}-\mathrm{m_j}}{\mathrm{M}}\langle\boldsymbol{\rho}\rangle\right), \tag{2.8}$$

where

$$\langle\boldsymbol{\rho}\rangle = \sum_{\mathrm{i}=1}^{\mathrm{N}} \mathbf{p}_{\mathrm{i}} \;\text{ and }\; \mathrm{M} = \sum_{\mathrm{i}=1}^{\mathrm{N}} \mathrm{m_i}. \tag{2.9}$$

The inverse transformation is given by

$$\mathbf{r}_i = \frac{1}{M}\sum_{j=i+1}^{N} m_j \mathbf{q}_{ij} - \frac{1}{M}\sum_{j=1}^{i-1} m_j \mathbf{q}_{ji} + \langle \mathbf{q} \rangle, \tag{2.10}$$

and

$$\mathbf{p}_i = \sum_{j=i+1}^{N} \boldsymbol{\rho}_{ij} - \sum_{j=1}^{i-1} \boldsymbol{\rho}_{ji} + \frac{m_i}{M}\langle \boldsymbol{\rho} \rangle, \tag{2.11}$$

where

$$\langle \mathbf{q} \rangle = \frac{1}{M}\sum_{i=1}^{N} m_i \mathbf{r}_i. \tag{2.12}$$

Next, we define a fictitious particle k for each pair of particles i, j as follows

$$k(i,j) = (i-1)N - \frac{i(i+1)}{2} + j, \tag{2.13}$$

with j>i and the total number of fictitious particles being equal to $K = N(N-1)/2$. In addition, we define the parameters α_{ik} and β_{ik}, as $\alpha_{ik} = 1, \beta_{ik} = m_j/M$ and $\alpha_{jk} = -1, \beta_{jk} = -m_i/M$ when $k = k(i,j)$, otherwise $\alpha_{ik} = \beta_{ik} = 0$. Given the above, Eqs. (2.10) and (2.11) take the following simplified form

$$\mathbf{p}_i = \sum_{k=1}^{K} \alpha_{ik} \boldsymbol{\rho}_k + \frac{m_i}{M}\langle \boldsymbol{\rho} \rangle, \tag{2.14}$$

and

$$\mathbf{r}_i = \sum_{k=1}^{K} \beta_{ik} \mathbf{q}_k + \langle \mathbf{q} \rangle. \tag{2.15}$$

To obtain α_{ik} in Eq. (2.14) we need to check whether k satisfies Eq. (2.13) with one of the particles in Eq. (2.13) equal to i.

2.2.5 Propagation

The Hamiltonian of the strongly driven six-body system is given by

$$H = \sum_{i=1}^{N} \frac{\mathbf{p}_i^2}{2m_i} + \sum_{i=1}^{N-1}\sum_{j=i+1}^{N} \frac{Q_i Q_j}{|\mathbf{r_i} - \mathbf{r_j}|} - \sum_{i=1}^{N} Q_i \mathbf{r_i} \cdot \mathbf{E}(t), \tag{2.16}$$

where Q_i is the charge, m_i is the mass, $\mathbf{r}_i$ is the position vector and $\mathbf{p}_i$ is the momentum vector of particle i. Here, N=6 and K=15. We denote the three electrons as particles 4,5 and 6. The nuclei are particles 1,2 and 3. The Hamiltonian of the system is described within the dipole approximation. This is justified since nondipole effects are not significant for the intensities and wavelengths considered throughout this chapter. Substituting Eqs. (2.7) and (2.14) in Eq. (2.16), we find the Hamiltonian in regularized coordinates to be given by

$$H = \sum_{k,k'=1}^{K} T_{kk'}\boldsymbol{\rho}_k\boldsymbol{\rho}_{k'} + \frac{\langle\boldsymbol{\rho}\rangle^2}{2M} + \sum_{k=1}^{K}\frac{U_k}{q_k} + \sum_{i=1}^{N} Q_i\langle\mathbf{q}\rangle - \sum_{k=1}^{K} L_k\mathbf{q}_k \tag{2.17}$$

with $T_{kk'} = \sum_{i=1}^{N}\frac{\alpha_{ik}\alpha_{ik'}}{2m_i}$, $U_k = Q_iQ_j$ and $L_k = \frac{Q_im_j - Q_jm_i}{M}$. Once the initial conditions are specified at time t_0, we propagate in time the positions and momenta of each of the six particles. To do so, we use Hamilton's equations of motion

$$\begin{aligned} \frac{d\mathbf{q}_k}{dt} &= \frac{\partial H}{\partial\boldsymbol{\rho}_k}\ , \quad \frac{d\boldsymbol{\rho}_k}{dt} = -\frac{\partial H}{\partial\mathbf{q}_k} \\ \frac{d\langle\mathbf{q}\rangle}{dt} &= \frac{\partial H}{\partial\langle\boldsymbol{\rho}\rangle}\ , \quad \frac{d\langle\boldsymbol{\rho}\rangle}{dt} = -\frac{\partial H}{\partial\langle\mathbf{q}\rangle} \end{aligned} \tag{2.18}$$

with Hamiltonian (2.17), resulting in

$$\begin{aligned} \frac{d\mathbf{q}_k}{dt} &= 2\sum_{k'=1}^{K} T_{kk'}\boldsymbol{\rho}_{k'}\ , \quad \frac{d\langle\mathbf{q}\rangle}{dt} = \frac{1}{M}\langle\boldsymbol{\rho}\rangle, \\ \frac{d\boldsymbol{\rho}_k}{dt} &= \frac{U_k\mathbf{q}_k}{q_k^3} + L_k\mathbf{E}(t)\ , \quad \frac{d\langle\boldsymbol{\rho}\rangle}{dt} = \sum_{i=1}^{N} Q_i\mathbf{E}(t). \end{aligned} \tag{2.19}$$

These are of the exact same form as in [56] with the only exception being that in this work we have six particles rather than four. We use the leapfrog method in conjunction with the Bulirsch-Stoer technique to propagate in time. This technique is described in more detail in [56].

2.2.6 Criteria for turning on and off the Coulomb forces between pairs of electrons

In this model, the interaction between a pair of electrons where at least one is quasifree is described with Coulomb forces. The interaction between bound electrons is turned off. Hence, we need to define during time propagation, i.e. on the fly, if an electron is quasifree or bound. At the start of propagation, the electron that tunnel ionizes (electron 4) is considered quasifree and the other two (electrons 5 and 6) are bound. At times $t > t_0$, a quasifree electron i transitions to bound if the following condition is satisfied: in less than half a period of the laser pulse, there are two or more peaks of its position coordinate along the field axis . A bound electron transitions to quasifree at time $t > t_0$ if either one of the following two conditions is satisfied: (i) at time t the compensated energy of electron i converges to a positive value or (ii) there are less than two peaks of its position coordinate along the field axis in half a period of the laser pulse. Practically this is achieved through the use of the switching functions c_k. The rate of change of regularized momentum from Hamiltons equations of motion (2.19) with this addition becomes

$$\frac{d\boldsymbol{\rho}_k}{dt} = (1 - c_k)\frac{U_k \mathbf{q}_k}{q_k^3} + L_k \mathbf{E}(t) \tag{2.20}$$

with $c_{k(i,j)}$ a binary function which is set to one for a given pair of electrons when both are bound and is zero otherwise.

2.2.6.1 Convergence of the compensated energy

The compensated energy of electron i is given by

$$\varepsilon_i^{comp}(t) = \frac{\tilde{\mathbf{p}}_i^2}{2m_i} + \sum_{j=1}^{3} \frac{Q_j Q_i}{|\mathbf{r}_j - \mathbf{r}_i|} \tag{2.21}$$

with the canonical momentum $\tilde{\mathbf{p}}_i$ given by

$$\tilde{\mathbf{p}}_i = \mathbf{p}_i + Q_i \mathbf{A}(t), \tag{2.22}$$

and the vector potential $\mathbf{A}(t)$ given by

$$\mathbf{A}(t) = -\int_{\infty}^{t} \mathbf{E}(t)dt \tag{2.23}$$

We consider the compensated energy as having converged if all of the following steps are true: (i) the compensated energy becomes positive at time t_1, (ii) starting from t_1, we count the number of steps where the slope of the compensated energy with respect to time is 1/50 of the slope at time t_1 and the slope has not changed sign. If this number of consecutive steps is 100 or higher, then we consider that the electron becomes quasifree at the last of these time steps. If the slope changes sign, or no longer satisfies the 1/50 rule or if the compensated energy becomes negative, then the counter for the time steps is reset to 0. We also assume that 1/50 of the slope during the 100 consecutive time steps is less than the threshold value of 0.01. This accounts for a large slope at t_1 as a result of a sudden change in the compensated energy of the electron.

2.2.7 Probabilities for ionization processes

We propagate the system until a time t_f where the electrons as well as the nuclei are significantly far apart from each other. At this time, for each trajectory, we check the energies of the three electrons. If the energy of n electrons are positive, we classify the trajectory as having n electrons ionized. The probability for n electrons to ionize is given by $P_n = N_n / N$, where N_n and N are the n-ionised and all events, respectively. To find the ionization time of each electron, t_i, $i = 1, 2$, we register the compensated energy [87]. We define as time of ionisation the time where the compensated energy, see Eq. (2.21) becomes positive and remains positive thereafter [87]. This is not equivalent to the time where an electron becomes quasifree, which is determined on the fly during time propagation, see Sec. 2.2.6.1.

2.3 Results

Using the 3D model described above, we focus on triple ionization, "frustrated" triple ionization and double ionization [1]. The electric field strength E_0 is taken

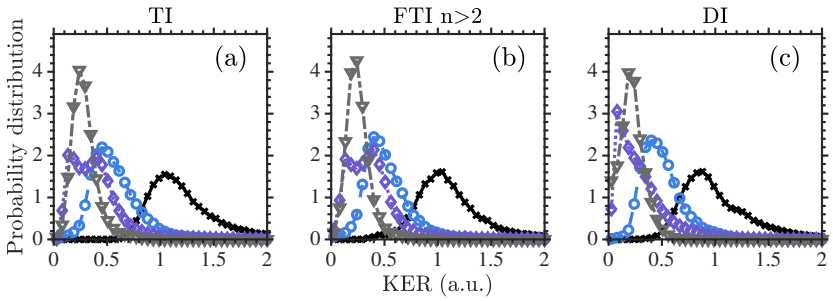

Figure 2.1: Distribution of the sum of the final kinetic energies (black solid lines with crosses) of the ion fragments produced in (a) triple ionization, (b) "frustrated" triple ionization and (c) double ionization. The dashed light grey lines and downwards triangles depict the distribution of the final kinetic energy of the He^{2+} ion fragment for TI, He^{+*} for FTI and He^{+} for DI. The dashed purple lines and diamonds (dashed blue lines and circles) depict the distribution of the final kinetic energy of the middle (left) H^{+} ion fragment for TI, FTI and DI. All curves are normalized to one.

equal to 0.08 a.u. The frequency ω corresponds to a wavelength of 800 nm and τ is taken to be 40 fs. We find that out of all ionization events roughly 3.5% are TI events, 1% are FTI events while 25% are DI events. In triple ionization the resulting fragments are He^{2+} and two H^{+} ions. In "frustrated" triple ionization, one electron stays in a Rydberg state either on H^{+} or He^{2+}. However, for FTI, we find that the formation of He^{+*} and two H^{+} ions is three times more likely than the formation of He^{2+}, H^{*} and H^{+}. Hence, in what follows we focus on the most probable channel of FTI. Moreover, we consider FTI events in high Rydberg states with $n > 2$. The reason we ignore FTI events with $n = 2$ is the same as for previous work on HeH^{+} [68]. Namely, an electron from the $n = 1$ state of H^{+} tunnels to the $n = 2$ state of He^{2+}. As a result, we obtain a large number of $n = 2$ states. Moreover, for DI it is significantly more likely for the final fragments to be He^{+} and two H^{+} ions rather than He^{2+}, H^{+} and H. Hence, in what follows we focus on the most probable channel of DI as we do for FTI, unless we indicate otherwise.

2.3.1 Distributions of the kinetic energy release of the nuclei

In Fig. 2.1, we plot the kinetic energy release (KER) distributions of the final ion fragments for triple ionization, "frustrated" triple ionization and double ionization.

We find that the KER distribution peaks around 1 a.u. for TI and FTI, while it peaks around 0.8 a.u. for DI. These peak values are consistent with the peak values of the distributions of the inter-nuclear distances at the time an electron tunnel-ionizes last. Indeed, we find (not shown) for TI and FTI (DI) that the most probable inter-nuclear distances are around 5 (3) a.u. between He and middle H, around 7 (5) a.u. between He and left H and around 3 (3) a.u. between the two H atoms. Thus, the peak of the KER distribution for TI and FTI is given roughly by 2/7+ 2/5+1/3 $\approx$ 1. For DI, where the bound electron is mostly attached on He resulting in He^+, the peak of the KER distribution is roughly given by 1/5+1/3+1/3 $\approx$ 0.87.

Also, in Fig. 2.1 we show that left H^+ is the faster fragment in all three processes. The slowest fragments are the middle H^+ for all three processes and He^{2+} for TI, He^{+*} for FTI and He^+ for DI. This is consistent with the two Coulomb repulsive forces on the left H^+ ion pointing along 180° with respect to the +z-axis. The repulsive forces on He^{2+} for TI, He^{+*} for FTI and He^+ for DI also add up towards 0° from the +z-axis. However, the mass of He compared to H is four times larger. As a result, He ends up with a smaller acceleration and hence smaller final kinetic energy compared to the left H^+. In addition, the repulsive forces on the middle H^+ which are exterted from He^{2+} for TI, He^{+*} for FTI and He^+ for DI and from left H^+ point in the opposite direction than the repulsive force exerted from the left H^+ nucleus. As a result, the kinetic energy of the middle H^+ ion is smaller compared to the left H^+ ion.

Moreover we find that the KER distribution of middle H^+ has a double peak structure for TI and FTI. This double peak is associated with middle H^+ escaping mainly either along or at an angle with respect to the molecular axis away from He^{2+} for TI and He^{+*} for FTI. The lower (higher) peak in the KER distribution of middle H^+ corresponds to the middle H^+ escaping along (at an angle with) the molecular axis. The lower peak is more pronounced for DI, since the force on middle H^+ from He^+ in DI is smaller than the force from He^{2+} in TI and He^{+*} in FTI.

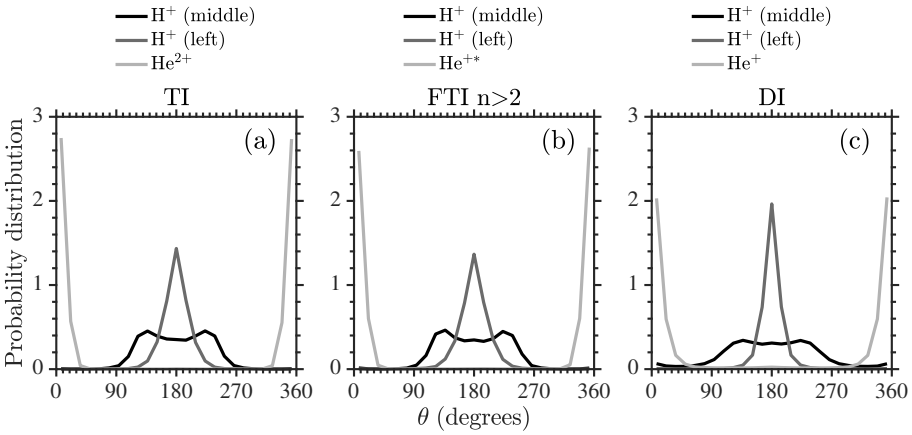

Figure 2.2: Angular distributions of the ion fragments produced in (a) triple ionization, (b) "frustrated" triple ionization and (c) double ionization. The escape along the +z axis corresponds to 0°. All curves are normalized to one.

2.3.2 Angular distributions of the nuclei

In Fig. 2.2, we plot the angular distribution of the final ion fragments for triple ionization as well as for the most probable channels of "frustrated" triple ionization and double ionization. For TI and FTI, we find that the angular distribution of middle H^+ is broader compared to left H^+. As discussed above, this is consistent with the Coulomb repulsive force on the middle H^+ ion being smaller compared to the left H^+ ion. We expect that another factor contributing to the broader angular distribution of the middle H^+ ion is that the two electrons that tunnel-ionize last mostly move between He and middle H^+, before they both (one) escape for TI (FTI). This is due to He having a higher nuclear charge. The difference between the two angular distributions of the H^+ ions is even more pronounced for DI. Indeed, the full screening of He^{2+} by the electron bound in the $n = 1$ state results in He^+ exerting a force towards 180° on the middle H^+ ion that roughly cancels out the force towards 0° from the left H^+ ion.

2.3.3 Pathways of frustrated triple ionization

Next, we investigate the distribution of the principal n quantum number of the two main pathways of FTI. We find that both pathways A and B with $n > 2$ contribute roughly the same to FTI. As already discussed, we find that formation of a Rydberg state is three times more likely for He versus H attachment. This is shown in Fig. 2.3 where we plot the distribution of the principal quantum number n for pathways A and B of FTI. We also find that the distribution of the principal quantum number n peaks around 20 when the electron remains bound in a Rydberg state of He^{2+} versus 10 following attachment on H^{+}. This is expected. One assumes that the electron that tunnel-ionizes last and remains bound in a Rydberg state has roughly the same energy for attachment on He or H. Then, given the dependence of the energy of a hydrogenic atom on the nuclear charge Z and the n number, it follows that an n number for attachment on H is equivalent to a 2n number for attachment on He. Moreover, we find that the distribution of the n number peaks at higher n values for pathway B versus pathway A. This is consistent with the electron that remains bound in a Rydberg state in pathway B being the electron that tunnel-ionizes in the initial state. As a result, this electron upon its return to the nuclei has higher energy compared to the energy that an initially bound electron has when it tunnel-ionizes for the last time and remains in a Rydberg state in pathway A.

2.3.4 Correlated electron dynamics in triple ionization

Our results suggest a weak effect of the correlated electron dynamics in triple ionization during fragmentation of the strongly-driven triatomic molecule HeH_2^+. Specifically, we find that for roughly 20% of triple ionization events a re-collision takes place where electron 4 transfers energy to both initially bound electrons 5 and 6 at the same time. For these events, the distribution of the maximum of the potential energy between electrons 4 and 5 or electrons 4 and 6 as a function of time extends up to 2 a.u. (not shown). For the rest of the TI events this maximum of the potential energy peaks overwhelmingly around very small values.

The weak electronic correlation in TI of strongly-driven HeH_2^+ is also supported by the distribution of the difference in ionization times of the fastest and

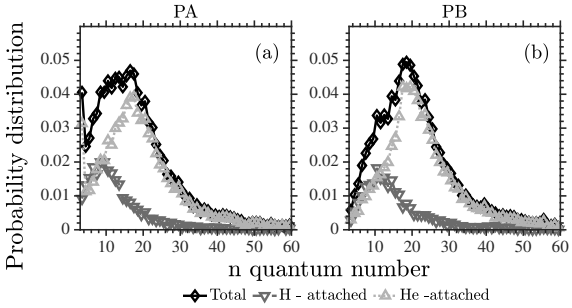

Figure 2.3: Distribution of the principal n quantum number for pathway A (a) and B (b) of FTI (black solid lines with diamonds). For pathway A and B of FTI the distribution of the n quantum number is also plotted separately when the electron remains attached to He^{2+} (light grey lines with upwards pointing triangles) and when it remains attached on H^{+} (dark grey lines with downwards pointing triangles).

second fastest electron as well as the fastest and slowest electron. These two distributions are shown in Fig. 2.4. We find that the electron that ionizes second has a significant probability to do so with a small time difference from the fastest one. It also has a significant probability to do so with time differences extending from one to four periods of the laser field. In contrast, the last electron to ionize does so with a distribution of time differences that roughly peaks around four periods of the laser field. This suggests, that the second but mostly the last to ionize electrons escape mainly due to enhanced ionization and not due to a re-collision. This is expected for molecules that are fragmenting when driven by long duration and intense pulses. We find this to also be the case for FTI and DI. Indeed, in Fig. 2.4 the distribution of the time differences between the two electrons that escape in FTI and DI extends up to roughly five periods of the laser field, suggesting that FTI and DI take place mostly due to enhanced ionization.

2.4 Conclusions

In this chapter, we formulate a 3D semi-classical model for a strongly-driven 6-body Coulomb problem to address three-electron dynamics in strongly-driven triatomic molecules. Since we include the Coulomb singularities, we address how to avoid

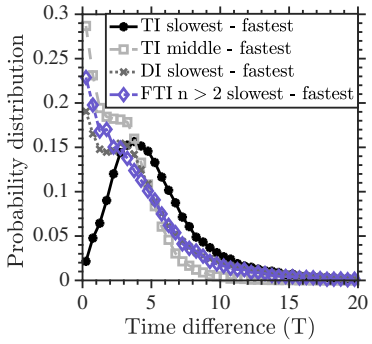

Figure 2.4: Distribution of the time differences between the fastest and second fastest electron as well as the fastest and slowest electron in TI and between the fastest and slowest electrons in FTI and DI.

unphysical autoionization between two bound electrons. To do so, we develop two criteria that allow us to switch off the Coulomb force between two bound electrons and switch it on when one of the two electrons ionizes or becomes quasifree. In our current formulation, the two bound electrons screen each other only indirectly via their interaction with the three nuclei and the other electron. We expect that this is a very good approximation for processes involving electrons in highly excited states before the electrons actually ionize. In this case the electrons screen each other less. Hence, we expect the current formulation to accurately describe mostly TI and FTI and less so DI. Indeed, in DI one electron remains bound in the $n = 1$ state resulting in higher screening of the nuclear charge during the time that it takes for the last electron to ionize.

Using this 3D semiclassical model, we address triple and double ionization as well as "frustrated" triple ionization in a strongly-driven linear triatomic molecule, namely, HeH_2^+. We find that the electronic correlation in all three ionization processes is weak. Moreover, we find that, as for "frustrated" double ionization, pathways A and B of FTI both contribute to the formation of Rydberg states at the end of the laser field. We also find that the electron that remains bound in FTI is roughly three times more likely to be attached to He^{2+} compared to H^+. Computing the angular distributions of the final ion fragments in all three ionization processes we find that middle H^+ escapes with a broader range of angles compared to left H^+ and He^{2+} for TI, He^{+*} for FTI and He^+ for DI. This is mainly due to the Coulomb

repulsive forces on the middle H^+ ion from the other two ions pointing in opposite directions. Thus, the resultant force has a smaller magnitude compared to the forces on the other two ions. For DI these opposite pointing Coulomb forces on the middle H^+ are even more comparable in magnitude. This is due to the screening of He^{2+} from the $n = 1$ bound electron. As a result, the angular distribution of the middle H^+ ion is even broader for DI compared to TI and FTI.

With this model we could not describe "frustrated" double ionization due to the inability of our model to describe the interaction between bound electrons. This motivates the work in the following chapter. That is, we focus on generalizing our current formulation to include effective potentials that will account for the electronic repulsion between two bound electrons. In this thesis, we do so in the context of driven atoms. However, we expect that in the future the model in the next chapter will be generalized to account for driven molecules.

Chapter 3

A general model and toolkit for the ionization of three or more electrons in strongly driven atoms using an effective Coulomb potential for the interaction between bound electrons

In this chapter, we formulate a three-dimensional semi-classical model to address triple and double ionization in three-electron atoms driven by intense infrared laser pulses [2]. Significantly improving on our previous model in Chapter 2, we now account for the interaction between bound electrons, which allows us to consider more ionization processes. During time propagation, our model fully accounts for the Coulomb singularities, the magnetic field of the laser pulse and for the motion of the nucleus at the same time as for the motion of the three electrons. The framework we develop is general and can account for multi-electron ionization in strongly-driven atoms with more than three electrons. To avoid unphysical autoionization arising in classical models of three or more electrons, we replace the Coulomb potential between pairs of bound electrons with effective Coulomb potentials. The Coulomb forces between electrons that are not both bound are fully accounted for. We develop a set of criteria to determine when electrons become bound during time

propagation. We compare ionization spectra obtained with the model developed here and with the Heisenberg model [88] that includes a potential term restricting an electron from closely approaching the core. Such spectra include the sum of the electron momenta along the direction of the laser field as well as the correlated electron momenta. We also compare these results with experimental ones [30, 31].

3.1 Introduction

For three-electron escape, due to the larger degree of complexity involved, only few theoretical studies exist that have a number of approximations. These studies include classical models with reduced-dimensionality [19] and with soft core Coulomb potentials [20, 23, 24, 89, 90], reduced-dimensionality quantum mechanical treatments [21, 22, 91] and semi-classical models with Heisenberg potentials [25]. On the experimental front, several studies have addressed multi-electron ionization in strongly-driven Ar and Ne [27–33]. For weak fields, striking angular patterns of three-electron escape and the underlying collision mechanisms were identified with 3D semi-classical models and ab-initio quantum mechanical techniques [92–95].

The main challenge facing quantum mechanical studies of triple ionization in strongly-driven systems is the significant amount of computational resources. This explains the development of reduced dimensionality quantum mechanical models [21, 22, 91]. On the other hand, the main difficulty encountered by 3D semi-classical studies of multi-electron ionization that include the Coulomb singularity is unphysical autoionization. Namely, one of the bound electrons can undergo a close encounter with the core and acquire a very negative energy leading to the escape of another bound electron. This is avoided in quantum mechanical treatments of multi-electron systems due to the lower energy bound of an electron. Adding a Heisenberg potential is an approach adopted to exclude unphysical autoionization in 3D semi-classical treatments [88]. This potential amounts to adding a potential barrier that mimics the Heisenberg uncertainty principle and prevents each electron from a close encounter with the core. The addition to the Hamiltonian of an extra

momentum and position dependent term results in the momentum of a particle being no longer directly related to the rate of change of its position, $\mathbf{p} \neq m\dot{\mathbf{r}}$ [96, 97]. In what follows, we refer to this model as H model. An advantage of this model is that electronic interactions are accounted for with Coulomb forces at all times during propagation. However, due to the Heisenberg potential, each electron accesses a reduced phase space resulting in a less accurate description of the interaction of each electron with the core. Indeed, in what follows we show that the H model gives rise to "softer" re-collisions upon the return of an electron to the core.

In this thesis, we take another approach to addressing unphysical autoionization in 3D semi-classical models that include the Coulomb singularity. We develop a 3D semi-classical model that describes the interaction between a pair of bound electrons via an effective Coulomb potential [98]. The interaction between all other pairs of electrons are described with Coulomb forces. This model advances our previous work of triple ionization in strongly-driven H_2He^+, where we switched off the Coulomb force between bound electrons, see Chapter 2. In the current work, we develop an efficient set of criteria to determine on the fly, i.e. during time-propagation whether an electron is bound or quasifree. Hence, we determine on the fly whether the interaction between two electrons is described by the Coulomb or the effective Coulomb potential. We refer to this model as ECBB—effective Coulomb potential for bound-bound electrons. We show that the ECBB model accurately describes three- and two-electron ionization spectra in strongly-driven three-electron atoms.

We compare the ECBB model with the H model motivated by a recent study on the performance of different classical models concerning double ionization of strongly driven two-electron Ar in Ref. [99]. This study has shown that the two-electron classical model that includes the full Coulomb force between the two electrons [40] and the H model results in observables that agree much better with experimental results compared to the soft core Coulomb potential models.

Our motivation for developing the ECBB-model is the accurate description at all times of the Coulomb interaction of each electron with the core, unlike the H model. The importance of this interaction has been demonstrated in the finger-like

structure in the correlated electron momenta in double ionization of strongly-driven Helium. This structure was predicted theoretically [16], observed experimentally [37, 38] and explained theoretically within a classical framework [36, 100]. On the other hand, the H model accurately accounts for the interaction between all pairs of electrons with Coulomb forces. The ECBB model does so for pairs of electrons where at least one electron is quasifree. In the ECBB model the interaction between two bound electrons is described by effective Coulomb potentials and is thus less accurate. However, bound electrons have a restricted dynamics compared to quasifree electrons. Hence, one can argue that it is more important to accurately describe the interaction of each electron with the core rather than the interaction between bound electrons.

In this thesis, we formulate the ECBB model and employ the H model fully accounting for both the motion of the core and all three electrons and for the magnetic field component of the Lorentz force. That is, we formulate both models in the non-dipole approximation. This is unlike previous theoretical studies of strongly-driven atoms. Our formalism is general and can be applied to treat multi-electron ionization in more than three-electron strongly-driven atoms. Here, we employ both models in the context of strongly-driven Ar. We note that the 3D semi-classical model for two-electron atoms that is a predecessor of the 3D model developed in this chapter previously yielded very good agreement with experimental observables for double ionization in strongly-driven Ar driven by few-cycles laser pulses [40]. In this latter model of double ionization, there was no need to address unphysical autoionization. Moreover, we discuss in detail the differences of the ECBB and H model concerning triple and double ionization observables. Such spectra include the probability distribution of the sum of the electron momenta components along the direction of the laser field and the correlated electron momenta. Also, we compare our results for the sum of the momenta with experimental ones [30, 31]. Finally, we obtain the probability distributions of the angle of escape between two electrons and between an electron and the core.

3.2 Model

In what follows, we describe in detail the formulation of the ECBB model [2] and the H model [88] that address multi-electron escape in strongly-driven atoms. The two methods resolve in a different way unphysical autoionization in 3D semi-classical models that fully account for the Coulomb singularity. We formulate both methods in the non-dipole approximation fully accounting for the magnetic field component of the laser field. The Hamiltonian of a N-body system in the non-dipole approximation is given by

$$H = \sum_{i=1}^{N} \frac{[\tilde{\mathbf{p}}_i - Q_i \mathbf{A}(\mathbf{r}_i, t)]^2}{2m_i} + \sum_{i=1}^{N-1} \sum_{j=i+1}^{N} \frac{Q_i Q_j}{|\mathbf{r_i} - \mathbf{r_j}|}, \tag{3.1}$$

where Q_i is the charge, m_i is the mass, $\mathbf{r}_i$ is the position vector and $\tilde{\mathbf{p}}_i$ is the canonical momentum vector of particle i. The mechanical momentum $\mathbf{p}_i$ is given by

$$\mathbf{p}_i = \tilde{\mathbf{p}}_i - Q_i \mathbf{A}(\mathbf{r}_i, t), \tag{3.2}$$

where $\mathbf{A}(\mathbf{r}_i, t)$ is the vector potential and $\mathbf{E}(\mathbf{r}_i, t) = -\frac{\partial \mathbf{A}(\mathbf{r}_i, t)}{\partial t}$ is the electric field. Modifying Eq. (3.1), in the following sections, we formulate the Hamiltonian for the ECBB and the H model.

3.2.1 Global regularisation

In both methods, we perform a global regularisation to avoid any numerical issues arising from the Coulomb singularities. We use the same scheme as in Sec. 2.2.4 except here it is the canonical momenta which is regularized rather than the mechanical momenta. In this chapter, the following equations are expressed in terms of the canonical momenta.

$$\boldsymbol{\rho}_{ij} = \frac{1}{N} \left(\tilde{\mathbf{p}}_i - \tilde{\mathbf{p}}_j - \frac{m_i - m_j}{M} \langle \boldsymbol{\rho} \rangle \right), \tag{3.3}$$

where

$$\langle \boldsymbol{\rho} \rangle = \sum_{i=1}^{N} \tilde{\mathbf{p}}_i, \tag{3.4}$$

and

$$\tilde{\mathbf{p}}_i = \sum_{k=1}^{K} \alpha_{ik} \boldsymbol{\rho}_k + \frac{m_i}{M} \langle \boldsymbol{\rho} \rangle. \tag{3.5}$$

3.2.2 Effective Coulomb potential between bound electrons method (ECBB model)

3.2.2.1 Derivation of the effective Coulomb potential

In what follows, we formulate a method that avoids unphysical autoionization between two bound electrons. To do so, we describe the interaction between two bound electrons with an effective Coulomb potential. However, we describe the interaction between a quasifree and a bound electron as well as between two quasifree electrons with the full Coulomb potential. In the next subsection, we define the time when an electron transitions from bound to quasifree and from quasifree to bound.

The effective Coulomb potential that electron i experiences due to the charge ζ_j of electron j, denoted by $V_{eff}(\zeta_j, |\mathbf{r}_1 - \mathbf{r}_i|)$, is derived as follows [98]. We approximate the wavefunction of a bound electron j with a 1s hydrogenic wavefunction

$$\psi(\zeta_j, |\mathbf{r}_1 - \mathbf{r}_j|) = \left(\frac{\zeta_j^3}{\pi}\right)^{1/2} e^{-\zeta_j |\mathbf{r}_1 - \mathbf{r}_j|}, \tag{3.6}$$

where the parameter ζ_j is later defined in Eq. (3.13). The electric charge contained within a sphere of radius r from the core is given by

$$\begin{aligned} Q(\zeta_j, r) &= -\int\int\int |\psi(\zeta_j, r)|^2 dV \\ &= 1 - \left[1 + 2\zeta_j r(1 + \zeta_j r)\right] e^{-2\zeta_j r}, \end{aligned} \tag{3.7}$$

where dV is the volume element in spherical coordinates. The electric field produced by a charge $Q(\zeta_j, r)$ that is contained within a spherical shell of radius r from the core is obtained by Gauss's law as follows:

$$\mathbf{E}(\zeta_j, r) = \frac{Q(\zeta_j, r)}{r^2} \hat{r}. \tag{3.8}$$

The work W done on a particle i due to the electric field $\mathbf{E}(\zeta_j, r)$ is equal to minus

the change in potential energy ΔV_{eff}:

$$\begin{aligned} W &= -\Delta V_{eff} \\ &= -\left[V_{eff}(\zeta_j, r) - V_{eff}(\zeta_j, \infty)\right] \\ &= -V_{eff}(\zeta_j, r). \end{aligned} \tag{3.9}$$

where we have used that $V_{eff}(\zeta_j, \infty) = 0$. The work W is also given by

$$\begin{aligned} W &= \int_{\infty}^{r} \mathbf{F} \cdot d\mathbf{r}' \\ &= -\int_{\infty}^{r} \mathbf{E} \cdot d\mathbf{r}' \\ &= -\int_{\infty}^{r} E(\zeta_j, r') \left(\hat{r}' \cdot \hat{r}'\right) dr' \\ &= \int_{\infty}^{r} \left[\frac{1}{r'^2} - \frac{e^{-2\zeta_j r'}(1 + 2\zeta_j r')}{r'^2} - 2\zeta_j^2 e^{-2\zeta_j r'}\right] dr' \\ &= \left(-\frac{1}{r'} + \frac{e^{-2\zeta_j r'}}{r'} + \zeta_j e^{-2\zeta_j r'}\right)\Bigg|_{\infty}^{r} \\ &= -\frac{1 - (1 + \zeta_j r)e^{-2\zeta_j r}}{r}, \end{aligned} \tag{3.10}$$

where we have used that particle i is an electron and hence $\mathbf{F} = -\mathbf{E}$ as well as that particle j is an electron and $Q(\zeta_j, r)$ is given by Eq. (3.7). Using Eqs. (3.9) and (3.10), we find

$$V_{eff}(\zeta_j, r) = \frac{1 - (1 + \zeta_j r)e^{-2\zeta_j r}}{r}, \tag{3.11}$$

which is the potential energy that an electron i has at a distance r from the core due to the charge of a bound electron j. Thus, the effective Coulomb potential that an electron i experiences at a distance $|\mathbf{r}_1 - \mathbf{r}_i|$ from the core due to the charge distribution of electron j is equal to

$$V_{eff}(\zeta_j, |\mathbf{r}_1 - \mathbf{r}_i|) = \frac{1 - (1 + \zeta_j |\mathbf{r}_1 - \mathbf{r}_i|)e^{-2\zeta_j |\mathbf{r}_1 - \mathbf{r}_i|}}{|\mathbf{r}_1 - \mathbf{r}_i|}. \tag{3.12}$$

$V_{eff}(\zeta_j, |\mathbf{r}_1 - \mathbf{r}_i|)$ is a repulsive potential which has limiting values of ζ_j when $|\mathbf{r}_1 - \mathbf{r}_i| = 0$ and 0 when $|\mathbf{r}_1 - \mathbf{r}_i| \to \infty$. If the effective charge $\zeta_j(t)$ is zero then

the effective potential $V_{eff}(\zeta_j, |\mathbf{r}_1 - \mathbf{r}_i|)$ is zero.

3.2.2.2 Definition of the effective charge

The effective charge $\zeta_j(t)$, at any time during the propagation of the four-body system, is proportional to the energy $\mathcal{E}_j(t)$ of electron j, assuming electron j is bound with an energy greater than a lower limit [98]. We set this lower limit to be equal to the ground state energy $\mathcal{E}_{1s}$ of a hydrogenic atom with core charge equal to Q_1, i.e. $\mathcal{E}_{1s} = -\frac{Q_1^2}{2}$. Moreover, when the energy of electron j, $\mathcal{E}_j(t)$, is greater than zero, we set $\zeta_j(t)$ equal to zero, while if the energy is less than the lower limit $\mathcal{E}_{1s}$ we set $\zeta_j(t)$ equal to Q_1. Hence, we define $\zeta_j(t)$ as follows

$$\zeta_j(t) = \begin{cases} Q_1 & \mathcal{E}_j(t) \leq \mathcal{E}_{1s} \\ (Q_1/\mathcal{E}_{1s})\,\mathcal{E}_j(t) & \mathcal{E}_{1s} < \mathcal{E}_j(t) < 0 \\ 0 & \mathcal{E}_j(t) \geq 0, \end{cases} \tag{3.13}$$

where the energy $\mathcal{E}_j(t)$ of electron j is given by

$$\begin{aligned} \mathcal{E}_j(t) = &\frac{\left[\tilde{\mathbf{p}}_j - Q_j \mathbf{A}(\mathbf{r}_j, t)\right]^2}{2m_j} + \frac{Q_j Q_1}{|\mathbf{r}_1 - \mathbf{r}_j|} - Q_j \mathbf{r}_j \cdot \mathbf{E}\left(\mathbf{r}_j, t\right) \\ &+ \sum_{\substack{i=2 \\ i \neq j}}^{N} c_{i,j}(t) V_{eff}(\zeta_i, |\mathbf{r}_1 - \mathbf{r}_j|). \end{aligned} \tag{3.14}$$

3.2.2.3 Definition of the functions $c_{i,j}(t)$

The functions $c_{i,j}(t)$ determine whether the full Coulomb interaction or the effective $V_{eff}(\zeta_i, |\mathbf{r}_1 - \mathbf{r}_j|)$ and $V_{eff}(\zeta_j, |\mathbf{r}_1 - \mathbf{r}_i|)$ potential interactions are on or off for any pair of electrons i and j during time propagation. Specifically, the limiting values of $c_{i,j}(t)$ are zero and one. The value zero corresponds to the full Coulomb potential being turned on while the effective Coulomb potentials are off. This occurs for a pair of electrons i and j where either i or j is quasifree. The value one corresponds to the effective Coulomb potentials $V_{eff}(\zeta_i, |\mathbf{r}_1 - \mathbf{r}_j|)$ and $V_{eff}(\zeta_j, |\mathbf{r}_1 - \mathbf{r}_i|)$ being turned on while the full Coulomb potential is off. This occurs for bound electrons i and j. For simplicity, we choose $c_{i,j}(t)$ to change linearly with time between the

limiting values zero and one. Hence, $c_{i,j}(t)$ is defined as follows

$$c_{i,j}(t) = \begin{cases} 0 & c(t) \leq 0 \\ c(t) & 0 < c(t) < 1 \\ 1 & c(t) \geq 1, \end{cases} \tag{3.15}$$

where $c(t) = \beta(t - t_s^{i,j}) + c_0$, and c_0 is the value of $c_{i,j}(t)$ just before a switch at time $t_s^{i,j}$. A switch at time $t_s^{i,j}$ occurs if the interaction between electrons i, j changes from full Coulomb to effective Coulomb potential or vice versa. At the start of the propagation at time t_0, $t_s^{i,j}$ is equal to t_0 and c_0 is one for pairs of electrons that are bound and zero otherwise. To allow for a smooth switch on or switch off of the effective Coulomb potential we choose β equal to ± 0.1; plus corresponds to a switch on and minus to a switch off of the effective Coulomb potential.

3.2.2.4 Derivation of the time derivative of the effective charges

Including the effective Coulomb potentials, the Hamiltonian of the four-body system is given by

$$\begin{aligned} H = &\sum_{i=1}^{N} \frac{[\tilde{\mathbf{p}}_i - Q_i \mathbf{A}(\mathbf{r}_i, t)]^2}{2m_i} + \sum_{i=2}^{N} \frac{Q_i Q_1}{|\mathbf{r_1} - \mathbf{r_i}|} \\ &+ \sum_{i=2}^{N-1} \sum_{j=i+1}^{N} \left[1 - c_{i,j}(t)\right] \frac{Q_i Q_j}{|\mathbf{r_i} - \mathbf{r_j}|} \\ &+ \sum_{i=2}^{N-1} \sum_{j=i+1}^{N} c_{i,j}(t) \left[V_{\text{eff}}(\zeta_j, |\mathbf{r}_1 - \mathbf{r}_i|) + V_{\text{eff}}(\zeta_i, |\mathbf{r}_1 - \mathbf{r}_j|)\right] \end{aligned} \tag{3.16}$$

The dipole term $-Q_j \mathbf{r}_j \cdot \mathbf{E}\left(\mathbf{r}_j, t\right)$ of Eq. (3.14) involving the electric field does not appear in the Hamiltonian (3.16). There is no contradiction. Indeed, the gauge-invariant energy of a particle does not always coincide with the gauge-dependent Hamiltonian, as discussed in Ref. [101, 102]. We note that the Hamiltonian in Eq. (3.16) depends not only on positions, momenta and time but also on the effective charges. Since the effective charge ζ_j is proportional to the energy $\mathcal{E}_j(t)$, see Eq. (3.13), it follows that we must obtain the derivative with time of $\mathcal{E}_j(t)$. We note that this is necessary at any time during propagation if at least two electrons are

bound. To do so, we apply the chain rule in Eq. (3.14) and obtain

$$\dot{\mathcal{E}}_j(t) = \frac{\partial \mathcal{E}_j(t)}{\partial \mathbf{r}_j} \cdot \dot{\mathbf{r}}_j + \frac{\partial \mathcal{E}_j(t)}{\partial \tilde{\mathbf{p}}_j} \cdot \dot{\tilde{\mathbf{p}}}_j + \frac{\partial \mathcal{E}_j(t)}{\partial \mathbf{r}_1} \cdot \dot{\mathbf{r}}_1 + \sum_{\substack{l=2 \\ l \neq j}}^{N} \frac{\partial \mathcal{E}_j(t)}{\partial \zeta_l} \dot{\zeta}_l + \frac{\partial \mathcal{E}_j(t)}{\partial t} \tag{3.17}$$

To simplify Eq. (3.17), we use Hamilton's equations of motion:

$$\dot{\mathbf{r}}_j = \frac{\partial H}{\partial \tilde{\mathbf{p}}_j} \quad , \quad \dot{\tilde{\mathbf{p}}}_j = -\frac{\partial H}{\partial \mathbf{r}_j} \tag{3.18}$$

Using

$$\frac{\partial H}{\partial \tilde{\mathbf{p}}_j} = 2\frac{\tilde{\mathbf{p}}_j - Q_j \mathbf{A}(\mathbf{r}_j, t)}{2m_j} = \frac{\mathbf{p}_j}{m_j} = \frac{\partial \mathcal{E}_j}{\partial \tilde{\mathbf{p}}_j} = \dot{\mathbf{r}}_j \tag{3.19}$$

we find that the second term in Eq. (3.17) which is given by $\frac{\partial \mathcal{E}_j(t)}{\partial \tilde{\mathbf{p}}_j} \cdot \dot{\tilde{\mathbf{p}}}_j$ can be written as $-\frac{\partial H}{\partial \mathbf{r}_j} \cdot \dot{\mathbf{r}}_j$. Thus, Eq. (3.17) takes the form

$$
\begin{aligned}
\dot{\mathcal{E}}_j(t) &= \frac{\partial \left[\mathcal{E}_j(t) - H\right]}{\partial \mathbf{r}_j} \cdot \dot{\mathbf{r}}_j + \frac{\partial \mathcal{E}_j(t)}{\partial \mathbf{r}_1} \cdot \dot{\mathbf{r}}_1 + \sum_{\substack{l=2 \\ l\neq j}}^{N} \frac{\partial \mathcal{E}_j(t)}{\partial \zeta_l} \dot{\zeta}_l + \frac{\partial \mathcal{E}_j(t)}{\partial t} \\
&= \frac{\partial \left[-Q_j \mathbf{r}_j \cdot \mathbf{E}\left(\mathbf{r}_j, t\right) - \sum_{i=2}^{N-1} \sum_{m=i+1}^{N} \left[1 - c_{i,m}(t)\right] \frac{Q_i Q_m}{|\mathbf{r_i} - \mathbf{r_m}|} \right]}{\partial \mathbf{r}_j} \cdot \dot{\mathbf{r}}_j \\
&+ \left[-\frac{Q_1 Q_j (\mathbf{r}_1 - \mathbf{r}_j)}{|\mathbf{r}_1 - \mathbf{r}_j|^3} + \sum_{\substack{i=2 \\ i\neq j}}^{N} c_{i,j}(t) \frac{\partial V_{\text{eff}}(\zeta_i, |\mathbf{r}_1 - \mathbf{r}_j|)}{\partial \mathbf{r}_1} \right] \cdot \dot{\mathbf{r}}_1 + \sum_{\substack{i=2 \\ i\neq j}}^{N} c_{i,j}(t) \frac{\partial V_{\text{eff}}(\zeta_i, |\mathbf{r}_1 - \mathbf{r}_j|)}{\partial \zeta_i} \dot{\zeta}_i \\
&+ \sum_{\substack{i=2 \\ i\neq j}}^{N} \dot{c}_{i,j}(t) V_{\text{eff}}(\zeta_i, |\mathbf{r}_1 - \mathbf{r}_j|) - 2 \frac{\tilde{\mathbf{p}}_j - Q_j \mathbf{A}(\mathbf{r}_j, t)}{2 m_j} \cdot Q_j \frac{\partial \mathbf{A}(\mathbf{r}_j, t)}{\partial t} - Q_j \mathbf{r}_j \cdot \frac{\partial \mathbf{E}\left(\mathbf{r}_j, t\right)}{\partial t} \\
&= \sum_{i=2}^{N-1} \sum_{m=i+1}^{N} \left[1 - c_{i,m}(t)\right] \frac{Q_i Q_m (\mathbf{r}_i - \mathbf{r}_m)}{|\mathbf{r}_i - \mathbf{r}_m|^3} \left(\delta_{i,j} - \delta_{m,j}\right) \cdot \dot{\mathbf{r}}_j \\
&+ \left[-\frac{Q_1 Q_j (\mathbf{r}_1 - \mathbf{r}_j)}{|\mathbf{r}_1 - \mathbf{r}_j|^3} + \sum_{\substack{i=2 \\ i\neq j}}^{N} c_{i,j}(t) \frac{\partial V_{\text{eff}}(\zeta_i, |\mathbf{r}_1 - \mathbf{r}_j|}{\partial \mathbf{r}_1} \right] \cdot \dot{\mathbf{r}}_1 \\
&+ \sum_{\substack{i=2 \\ i\neq j}}^{N} \left[c_{i,j}(t) \frac{\partial V_{\text{eff}}(\zeta_i, |\mathbf{r}_1 - \mathbf{r}_j|)}{\partial \zeta_i} \dot{\zeta}_i + \dot{c}_{i,j}(t) V_{\text{eff}}(\zeta_i, |\mathbf{r}_1 - \mathbf{r}_j|) \right] \\
&- Q_j \dot{\mathbf{r}}_j \cdot \mathbf{E}\left(\mathbf{r}_j, t\right) - Q_j \left(\mathbf{r}_j \cdot \frac{\partial \mathbf{E}\left(\mathbf{r}_j, t\right)}{\partial \mathbf{r}_j} \right) \cdot \dot{\mathbf{r}}_j + Q_j \dot{\mathbf{r}}_j \cdot \mathbf{E}\left(\mathbf{r}_j, t\right) - Q_j \mathbf{r}_j \cdot \frac{\partial \mathbf{E}\left(\mathbf{r}_j, t\right)}{\partial t} \\
&= \sum_{i=2}^{N-1} \sum_{m=i+1}^{N} \left[1 - c_{i,m}(t)\right] \frac{Q_i Q_m (\mathbf{r}_i - \mathbf{r}_m)}{|\mathbf{r}_i - \mathbf{r}_m|^3} \left(\delta_{i,j} - \delta_{m,j}\right) \cdot \dot{\mathbf{r}}_j \\
&+ \left[-\frac{Q_1 Q_j (\mathbf{r}_1 - \mathbf{r}_j)}{|\mathbf{r}_1 - \mathbf{r}_j|^3} + \sum_{\substack{i=2 \\ i\neq j}}^{N} c_{i,j}(t) \frac{\partial V_{\text{eff}}(\zeta_i, |\mathbf{r}_1 - \mathbf{r}_j|}{\partial \mathbf{r}_1} \right] \cdot \dot{\mathbf{r}}_1 \\
&+ \sum_{\substack{i=2 \\ i\neq j}}^{N} \left[c_{i,j}(t) \frac{\partial V_{\text{eff}}(\zeta_i, |\mathbf{r}_1 - \mathbf{r}_j|)}{\partial \zeta_i} \dot{\zeta}_i + \dot{c}_{i,j}(t) V_{\text{eff}}(\zeta_i, |\mathbf{r}_1 - \mathbf{r}_j|) \right] \\
&- Q_j \mathbf{r}_j \cdot \dot{\mathbf{E}}\left(\mathbf{r}_j, t\right)
\end{aligned}
\tag{3.20}
$$

where we use $\frac{\partial \mathbf{A}(\mathbf{r}_j,t)}{\partial t} = -\mathbf{E}(\mathbf{r}_j,t)$ and $-Q_j\left(\mathbf{r}_j \cdot \frac{\partial \mathbf{E}(\mathbf{r}_j,t)}{\partial \mathbf{r}_j}\right)\cdot \dot{\mathbf{r}}_j - Q_j\mathbf{r}_j \cdot \frac{\partial \mathbf{E}(\mathbf{r}_j,t)}{\partial t} = -Q_j\mathbf{r}_j \cdot \dot{\mathbf{E}}\left(\mathbf{r}_j,t\right)$, see Sec. D.2. The above expression can be finally written as

$$\dot{\mathcal{E}}_j(t) = f_j + \sum_{\substack{i=2 \\ i\neq j}}^{N} c_{i,j}(t)\frac{\partial V_{\text{eff}}(\zeta_i, |\mathbf{r}_1 - \mathbf{r}_j|)}{\partial \zeta_i}\dot{\zeta}_i, \tag{3.21}$$

where $f_j(\mathbf{r},\mathbf{p},t,\mathcal{E})$ are all the terms in Eq. (3.20) that do not depend on $\dot{\zeta}_i(t)$. $\mathbf{r}$ includes the positions of all particles and $\mathbf{p}$ includes the mechanical momenta of all particles. The time derivative of ζ_i is given by

$$\dot{\zeta}_i = \begin{cases} 0 & \mathcal{E}_i(t) \leq \mathcal{E}_{1s} \\ (Q_1/\mathcal{E}_{1s})\,\dot{\mathcal{E}}_i(t) & \mathcal{E}_{1s} < \mathcal{E}_i(t) < 0. \\ 0 & \mathcal{E}_i(t) \geq 0, \end{cases} \tag{3.22}$$

We obtain an equation similar to Eq. (3.21) for each electron. Hence, at any time during propagation, we have a system of three equations (for three electron atoms) where the time derivative of the energy of each electron depends on the time derivatives of the energies of the remaining electrons. Hence, we have to solve a system of three equations to obtain the time derivative of the energy of each electron. The process of solving this system of equations is described in more detail in Appendix F. As a result, we express each $\dot{\mathcal{E}}$ as a function of $(\mathbf{r},\mathbf{p},t,\mathcal{E})$ with no dependence on the derivatives of the energies of the remaining electrons.

3.2.2.5 Hamilton's equations of motion

Substituting Eqs. (2.7) and (3.5) in Eq. (3.16), we find the Hamiltonian in regularized coordinates to be given by

$$\begin{aligned} H = &\sum_{k,k'=1}^{K} T_{kk'}\boldsymbol{\rho}_k\boldsymbol{\rho}_{k'} + \frac{\langle \boldsymbol{\rho}\rangle^2}{2M} + \sum_{k=1}^{K}[1-c_k(t)]\frac{U_k}{q_k} \\ &+ \sum_{i=1}^{N}\frac{Q_i^2}{2m_i}\mathbf{A}^2(\mathbf{r}_i,t) - \sum_{i=1}^{N}\frac{Q_i}{m_i}\tilde{\mathbf{p}}_i\cdot\mathbf{A}(\mathbf{r}_i,t) \\ &+ \sum_{k=1}^{K} c_k(t)V_k, \end{aligned} \tag{3.23}$$

where

$$V_{k(i,j)} = V_{eff}(\zeta_j, |\mathbf{r}_1 - \mathbf{r}_i|) + V_{eff}(\zeta_i, |\mathbf{r}_1 - \mathbf{r}_j|), \tag{3.24}$$

and $\tilde{\mathbf{p}}$, $\mathbf{r}$, are expressed in terms of $\boldsymbol{\rho}$ and $\mathbf{q}$ via Eqs. (3.5) and (2.15). In what follows, we refer to the core as particle 1, and the electrons as particles 2,3 and 4. Moreover, for k=1,2,3 $\mathbf{q}_k$ corresponds to the relative distance between each one of the three electrons and the core. Since, the Coulomb force between each of the three electrons and the core is always on, we set $c_k(t) = 0$, for k=1,2,3. Using Eq. (3.23), we find that Hamilton's equations of motion are given by

$$\begin{aligned}
\frac{d\mathbf{q}_k}{dt} &= 2\sum_{k'=1}^{K} T_{kk'}\boldsymbol{\rho}_{k'} - \sum_{i=1}^{N}\frac{Q_i}{m_i}\alpha_{ik}\mathbf{A}(\mathbf{r}_i,t) \\
\frac{d\langle\mathbf{q}\rangle}{dt} &= \frac{1}{M}\langle\boldsymbol{\rho}\rangle - \sum_{i=1}^{N}\frac{Q_i}{M}\mathbf{A}(\mathbf{r}_i,t) \\
\frac{d\boldsymbol{\rho}_k}{dt} &= [1-c_k(t)]\frac{U_k\mathbf{q}_k}{q_k^3} - \sum_{k'=1}^{K} c_{k'}(t)\frac{\partial V_{k'}}{\partial \mathbf{q}_k} \\
&\quad + \sum_{i=1}^{N}\frac{Q_i}{m_i}[\tilde{\mathbf{p}}_i - Q_i\mathbf{A}(\mathbf{r}_i,t)]\cdot\frac{\partial\mathbf{A}(\mathbf{r}_i,t)}{\partial\mathbf{q}_k} \\
\frac{d\langle\boldsymbol{\rho}\rangle}{dt} &= \sum_{i=1}^{N}\frac{Q_i}{m_i}[\tilde{\mathbf{p}}_i - Q_i\mathbf{A}(\mathbf{r}_i,t)]\cdot\frac{\partial\mathbf{A}(\mathbf{r}_i,t)}{\partial\langle\mathbf{q}\rangle},
\end{aligned} \tag{3.25}$$

where using Eq. (3.24) we obtain

$$\frac{\partial V_{k'}}{\partial \mathbf{q}_k} = \frac{\partial V_{k'(i',j')}}{\partial \mathbf{q}_{k(i,j)}}\delta_{i,1}\delta_{j,i'} + \frac{\partial V_{k'(i',j')}}{\partial \mathbf{q}_{k(i,j)}}\delta_{i,1}\delta_{j,j'}, \tag{3.26}$$

where $\tilde{\mathbf{p}}, \mathbf{r}$ are expressed in terms of $\boldsymbol{\rho}$ and $\mathbf{q}$ via Eqs. (3.5) and (2.15). We use the chain rule and Eq. (2.15) to express the derivatives of the vector potential as

$$\frac{\partial\mathbf{A}(\mathbf{r}_i,t)}{\partial\mathbf{q}_k} = \frac{\partial\mathbf{A}(\mathbf{r}_i,t)}{\partial\mathbf{r}_i}\frac{\partial\mathbf{r}_i}{\partial\mathbf{q}_k} = \frac{\partial\mathbf{A}(\mathbf{r}_i,t)}{\partial\mathbf{r}_i}\beta_{ik} \tag{3.27}$$

and

$$\frac{\partial\mathbf{A}(\mathbf{r}_i,t)}{\partial\langle\mathbf{q}\rangle} = \frac{\partial\mathbf{A}(\mathbf{r}_i,t)}{\partial\mathbf{r}_i}\frac{\partial\mathbf{r}_i}{\partial\langle\mathbf{q}\rangle} = \frac{\partial\mathbf{A}(\mathbf{r}_i,t)}{\partial\mathbf{r}_i} \tag{3.28}$$

More detail as to the derivatives of the vector potential can be found in Appendix D. From Eqs. (3.25) and (3.26) it follows that the term $\sum_{k'=1}^{K} c_{k'}(t)\frac{\partial V_{k'}}{\partial \mathbf{q_k}}$ is non zero for k = 1,2,3 and has the following form, where we have used that k=4 corresponds to (i,j) = (2,3), k=5 corresponds to (i,j) = (2,4) and k=6 corresponds to (i,j) = (3,4).

$$\sum_{k'=1}^{K} c_{k'}(t)\frac{\partial V_{k'}}{\partial \mathbf{q_1}} = c_4(t)\frac{\partial V_{\mathrm{eff}}(\zeta_3,|\mathbf{r}_1-\mathbf{r}_2|)}{\partial \mathbf{q_1}} + c_5(t)\frac{\partial V_{\mathrm{eff}}(\zeta_4,|\mathbf{r}_1-\mathbf{r}_2|)}{\partial \mathbf{q_1}}$$
$$= c_4(t)\frac{-1+[1+2\zeta_3 q_1(1+\zeta_3 q_1)]\,e^{-2\zeta_3 q_1}}{q_1^3}\mathbf{q_1} + c_5(t)\frac{-1+[1+2\zeta_4 q_1(1+\zeta_4 q_1)]\,e^{-2\zeta_4 q_1}}{q_1^3}\mathbf{q_1}$$
$$\sum_{k'=1}^{K} c_{k'}(t)\frac{\partial V_{k'}}{\partial \mathbf{q_2}} = c_4(t)\frac{\partial V_{\mathrm{eff}}(\zeta_2,|\mathbf{r}_1-\mathbf{r}_3|)}{\partial \mathbf{q_2}} + c_6(t)\frac{\partial V_{\mathrm{eff}}(\zeta_4,|\mathbf{r}_1-\mathbf{r}_3|)}{\partial \mathbf{q_2}}$$
$$= c_4(t)\frac{-1+[1+2\zeta_2 q_2(1+\zeta_2 q_2)]\,e^{-2\zeta_2 q_2}}{q_2^3}\mathbf{q_2} + c_6(t)\frac{-1+[1+2\zeta_4 q_2(1+\zeta_4 q_2)]\,e^{-2\zeta_4 q_2}}{q_2^3}\mathbf{q_2}$$
$$\sum_{k'=1}^{K} c_{k'}(t)\frac{\partial V_{k'}}{\partial \mathbf{q_3}} = c_5(t)\frac{\partial V_{\mathrm{eff}}(\zeta_2,|\mathbf{r}_1-\mathbf{r}_4|)}{\partial \mathbf{q_3}} + c_6(t)\frac{\partial V_{\mathrm{eff}}(\zeta_3,|\mathbf{r}_1-\mathbf{r}_4|)}{\partial \mathbf{q_3}}$$
$$= c_5(t)\frac{-1+[1+2\zeta_2 q_3(1+\zeta_2 q_3)]\,e^{-2\zeta_2 q_3}}{q_3^3}\mathbf{q_3} + c_6(t)\frac{-1+[1+2\zeta_3 q_3(1+\zeta_3 q_3)]\,e^{-2\zeta_3 q_3}}{q_3^3}\mathbf{q_3}.$$

In addition to Eq. (3.25), we have three more equations for $\dot{\mathcal{E}}(\mathbf{q},\boldsymbol{\rho},t,\mathcal{E})$ that are solved during time propagation.

3.2.2.6 Propagation technique

In our formulation, we fully account for the Coulomb singularities. Hence, an electron can approach infinitely close to the nucleus during time propagation. To ensure the accurate numerical treatment of the N-body problem in the laser field, we perform a global regularisation. This regularisation was introduced in the context of the gravitational N-body problem [85]. Here, we integrate the equations of motion using a leapfrog technique [103, 104] jointly with the Bulirsch-Stoer method [105, 106]. This leapfrog technique allows integration of Hamilton's equation when the derivatives of the positions and the momenta depend on the quantities themselves. This technique was previously employed in our studies of non-dipole effects in non-sequential double ionization of strongly driven H_2 in Ref. [86]. The difference between the leapfrog technique employed in this work and the one previously

employed in [86] is that the former is more involved. Indeed, in the current leapfrog technique we also need to propagate in time the energies $\mathcal{E}(\mathrm{t})$, see Eq. (3.20). The steps involved in this leapfrog technique are as follows.

First, we perform a time transformation $\mathrm{t} \to \mathrm{s}$, where

$$\mathrm{ds} = \Omega(\mathbf{q})\mathrm{dt}, \tag{3.29}$$

with $\Omega(\mathbf{q})$ an arbitrary positive function of $\mathbf{q}$. We select the function

$$\Omega(\mathbf{q}) = \sum_{\mathrm{k}=1}^{\mathrm{K}} \frac{1}{|\mathbf{q}_{\mathrm{k}}|}, \tag{3.30}$$

which forces the time step to decrease when two particles undergo a close encounter and to increase when all particles are far away from each other. The equations of motion now take the following form

$$\begin{aligned} \mathbf{q}' &= \dot{\mathbf{q}}(\mathbf{q}, \boldsymbol{\rho}, \mathrm{t})/\Omega(\mathbf{q}) \\ \boldsymbol{\rho}' &= \dot{\boldsymbol{\rho}}(\mathbf{q}, \boldsymbol{\rho}, \mathrm{t}, \mathcal{E})/\Omega(\mathbf{q}) \\ \mathrm{t}' &= 1/\Omega(\mathbf{q}) \\ \mathcal{E}' &= \dot{\mathcal{E}}(\mathbf{q}, \boldsymbol{\rho}, \mathrm{t}, \mathcal{E})/\Omega(\mathbf{q}), \end{aligned} \tag{3.31}$$

with prime denoting the derivative with respect to the new variable s. The integration is based on the leapfrog technique described in Ref. [86] that introduces four auxiliary variables, two vectors $\mathbf{W}^{\mathbf{q}}, \mathbf{W}^{\boldsymbol{\rho}}$ and two scalars $\mathrm{W}^{\mathrm{t}}, \mathrm{W}^{\mathcal{E}}$. As a result, an extended system is obtained where the derivatives of the position, the momenta and the energies no longer depend on the quantities themselves. The extended equations are given by

$$\begin{aligned} \mathbf{q}' &= \dot{\mathbf{q}}(\mathbf{W}^{\mathbf{q}}, \boldsymbol{\rho}, \mathrm{W}^{\mathrm{t}})/\Omega(\mathbf{W}^{\mathbf{q}}) \\ \mathbf{W}^{\boldsymbol{\rho}\prime} &= \dot{\boldsymbol{\rho}}(\mathbf{W}^{\mathbf{q}}, \boldsymbol{\rho}, \mathrm{W}^{\mathrm{t}}, \mathcal{E})/\Omega(\mathbf{W}^{\mathbf{q}}) \\ \mathrm{t}' &= 1/\Omega(\mathbf{W}^{\mathbf{q}}) \\ \mathrm{W}^{\mathcal{E}\prime} &= \dot{\mathcal{E}}(\mathbf{W}^{\mathbf{q}}, \boldsymbol{\rho}, \mathrm{W}^{\mathrm{t}}, \mathcal{E})/\Omega(\mathbf{W}^{\mathbf{q}}), \end{aligned}$$

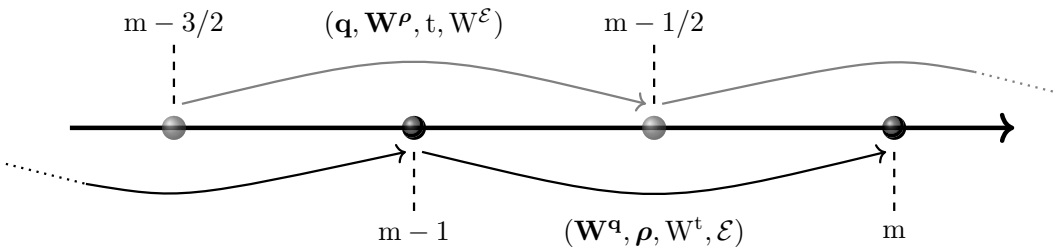

Figure 3.1: Schematic illustration of the propagation of the two quadruplets $(\mathbf{q}, \mathbf{W}^{\boldsymbol{\rho}}, \mathrm{t}, \mathrm{W}^{\mathcal{E}})$ and $(\mathbf{W}^{\mathbf{q}}, \boldsymbol{\rho}, \mathrm{W}^{\mathrm{t}}, \mathcal{E})$ over a sub step of size h, $\mathrm{m}-3/2 \rightarrow \mathrm{m}-1/2$ and $\mathrm{m}-1 \rightarrow \mathrm{m}$ respectively, with m=2,...,n-1.

and

$$\begin{aligned}
\mathbf{W}^{\mathbf{q}'} &= \dot{\mathbf{q}}(\mathbf{q}, \mathbf{W}^{\boldsymbol{\rho}}, \mathrm{t})/\Omega(\mathbf{q}) \\
\boldsymbol{\rho}' &= \dot{\boldsymbol{\rho}}(\mathbf{q}, \mathbf{W}^{\boldsymbol{\rho}}, \mathrm{t}, \mathrm{W}^{\mathcal{E}})/\Omega(\mathbf{q}) \\
\mathrm{W}^{\mathrm{t}'} &= 1/\Omega(\mathbf{q}) \\
\mathcal{E}' &= \dot{\mathcal{E}}(\mathbf{q}, \mathbf{W}^{\boldsymbol{\rho}}, \mathrm{t}, \mathrm{W}^{\mathcal{E}})/\Omega(\mathbf{q}).
\end{aligned}$$

We propagate for a time step, by propagating for half a step each quadruplet of variables $(\mathbf{q}, \mathbf{W}^{\boldsymbol{\rho}}, \mathrm{t}, \mathrm{W}^{\mathcal{E}})$ and $(\mathbf{W}^{\mathbf{q}}, \boldsymbol{\rho}, \mathrm{W}^{\mathrm{t}}, \mathcal{E})$ in an alternating way, see the leapfrog algorithm described in Appendix B. Moreover, to achieve better accuracy, we incorporate the leapfrog method in the Bulirsch-Stoer extrapolation scheme [105, 106]. In this scheme, a propagation over a step H, is split into n sub steps of size $\mathrm{h} = \mathrm{H}/\mathrm{n}$. We use the leapfrog method to propagate over each sub step. In Fig. 3.1, we offer a schematic illustration of the propagation during a time sub step of size h. The detailed algorithm is described in Appendix B. This process is repeated with increasing number of sub steps, i.e. $\mathrm{n} \rightarrow \infty$, until an extrapolation with a satisfactory error is achieved.

3.2.2.7 Definition of quasifree and bound electron

In the ECBB model the interaction between a pair of electrons where at least one is quasifree is described with Coulomb forces. The interaction between bound electrons is described with effective Coulomb potentials. Hence, we need to define during time propagation, i.e. on the fly, if an electron is quasifree or bound. At the start of propagation, the electron that tunnel-ionises (electron 2) is considered

quasifree and the other two (electrons 3 and 4) are bound. We denote the core as particle 1.

At times $t > t_0$, a quasifree electron i transitions to bound if the following conditions are satisfied: (i) the potential of electron i with the core, $V_{i,c}$, is larger than a threshold value, i.e. $V_{i,c} > V_{min}$ at t_1, and $V_{i,c}$ is continuously increasing, i.e. $\frac{dV_{i,c}(t_{n+5})}{dt} > \frac{dV_{i,c}(t_n)}{dt}$ for five times t_n which are five time steps apart with the first one being at time t_1, see Fig. 3.2(a); (ii) the position of electron i along the electric field, i.e. z axis here, has at least two extrema of the same kind, i.e. two maxima or two minima, in a time interval less than half a period of the laser field. The reason we choose this criterion is that if the electron motion was to be completely determined by the laser field along the z axis, then we can at most have two extrema of the same kind in one period of the laser field. However, when in addition to the laser field we also have the influence of a Coulomb field, then two extrema of the same kind along the direction of the field can only happen in a time interval less than one period. Our assumption is that the Coulomb field dominates over the electric field when two extrema of the same kind in the position of the electron along the axis of the field occur in less than half a period of the field. We start checking if condition (ii) is satisfied at time t_2 when electron i has the closest approach to the core, i.e. $V_{i,c}$ is maximum. We stop checking whether condition (ii) is satisfied at time t_3 when $V_{i,c}$ is smaller than the threshold value V_{min} and $V_{i,c}$ is continuously decreasing, i.e. $\frac{dV_{i,c}(t_n)}{dt} < \frac{dV_{i,c}(t_{n-5})}{dt}$ for five times t_n which are five time steps apart with the last one being at time t_3, see Fig. 3.2(a). Note that $V_{i,c}$ is minus the potential energy of electron i with the core. In the current study, we set V_{min} equal to 3/15 which is equal to 0.2 a.u. We find that our results remain almost the same for a range of values of V_{min}. Also, at the end of the laser pulse, we check whether a quasifree electron has positive or negative compensated energy [87]. If the latter occurs, we consider the electron to be bound. Accounting for the effective Coulomb potential, the compensated energy of electron i is given by

$$\varepsilon_i^{comp}(t) = \frac{\tilde{\mathbf{p}}_i^2}{2m_i} + \frac{Q_1 Q_i}{|\mathbf{r}_1 - \mathbf{r}_i|} + \sum_{\substack{j=2 \\ j\neq i}}^{N} c_{i,j}(t) V_{eff}(\zeta_j, |\mathbf{r}_1 - \mathbf{r}_i|). \tag{3.32}$$

A bound electron transitions to quasifree at time $t > t_0$ if either one of the following two conditions is satisfied: (i) at time t the compensated energy of electron i converges to a positive value, see Sec. 2.2.6.1; (ii) at times $t = t_3$, $V_{i,c}$ is smaller than the threshold value V_{min} and $V_{i,c}$ is continuously decreasing, i.e. $\frac{dV_{i,c}(t_n)}{dt} < \frac{dV_{i,c}(t_{n-5})}{dt}$ for five t_n which are five time steps apart, the last one being at t_3.

We illustrate the above criteria in Fig. 3.2(b). We denote the times t_1, t_2 and t_3 with red, grey and blue vertical dashed lines, respectively. In the left column, we plot the position r_z and the potential $V_{i,c}$ of a quasifree electron as it transitions to bound. In the right column, we plot the position r_z, the potential $V_{i,c}$ and the compensated energy of a bound electron as it transitions to quasifree. The black dashed line denotes the time when the compensated energy converges and the electron transitions from bound to quasifree. For this specific trajectory, the compensated energy converges prior to t_3 and hence electron i transitions from bound to quasifree at $t < t_3$.

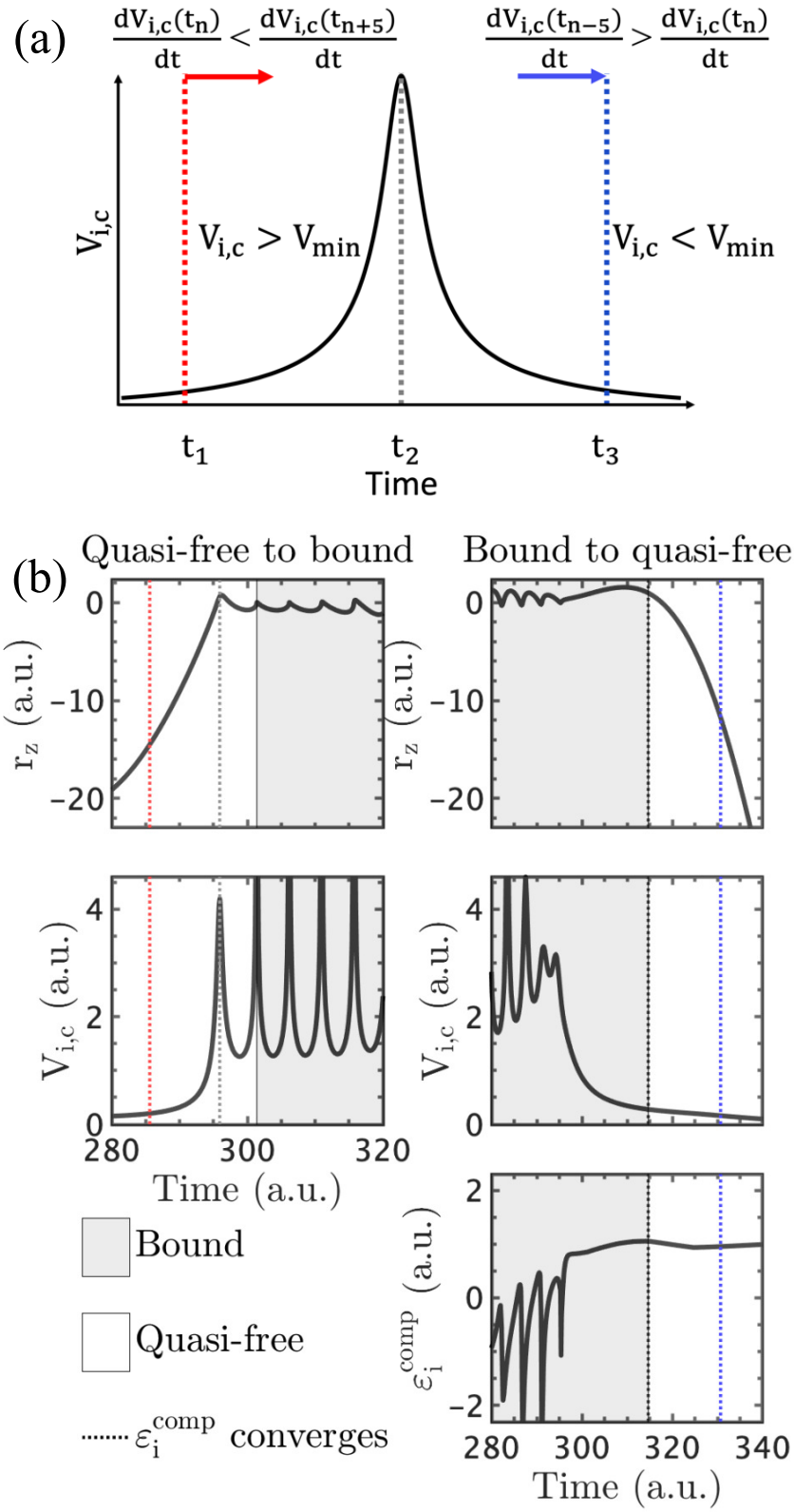

Figure 3.2: Schematic illustration of the criteria to determine when a quasifree electron becomes bound (left column) and when a bound electron becomes quasifree (right column).

We note that the criteria for the convergence of the compensated energy and the number of extrema in the position of the electron along the laser field have been used to determine whether an electron is quasifree or bound in our previous work on strongly-driven three electron triatomic molecules [1], see Sec 2.2.6. However, the criteria presented above are considerably more refined compared to the ones in Ref. [1], allowing for the full Coulomb forces to be turned on for a longer time interval. Moreover, in the ECBB model we account for the interaction between bound electrons with effective Coulomb potentials, while in Ref. [1] this interaction was set equal to zero.

3.2.3 Heisenberg potential method (H model)

3.2.3.1 Description of the model

The Heisenberg potential, originally proposed by Kirschbaum and Wilets in Ref. [88], is given by

$$V_{H,i} = \frac{\xi^2}{4\alpha\mu r_{i,1}^2} \exp\left\{\alpha\left[1-\left(\frac{r_{i,1}p_{i,1}}{\xi}\right)^4\right]\right\}, \tag{3.33}$$

where $\mathbf{r}_{i,1} = \mathbf{r}_1 - \mathbf{r}_i$ is the relative position of each one of the three electrons i=2,3,4 with respect to the core i=1, $\mathbf{p}_{i,1}$ is the corresponding relative momentum

$$\mathbf{p}_{i,1} = \frac{m_i\mathbf{p}_1 - m_1\mathbf{p}_i}{m_1 + m_i}, \tag{3.34}$$

and $\mu = m_1 m_i/(m_i + m_1)$ is the reduced mass of the electron-core system. This potential restricts the relative position and momentum of electron i according to

$$r_{i,1}p_{i,1} \geq \xi. \tag{3.35}$$

Hence, the Heisenberg potential acts as a repulsive potential when the electron is close to the core.

3.2.3.2 Hamilton's equations of motion

Including the Heisenberg potential for each one of the electron-core pairs, the Hamiltonian is given by

$$H = \sum_{i=1}^{N} \frac{[\tilde{\mathbf{p}}_i - Q_i \mathbf{A}(\mathbf{r}_i, t)]^2}{2m_i} + \sum_{i=1}^{N-1} \sum_{j=i+1}^{N} \frac{Q_i Q_j}{|\mathbf{r}_i - \mathbf{r}_j|} + \sum_{i=2}^{N} V_{H,i}. \tag{3.36}$$

Substituting Eq. (2.7) and Eq. (3.5) in Eq. (3.36), we obtain the Hamiltonian in regularized coordinates

$$\begin{aligned} H = & \sum_{k,k'=1}^{K} T_{kk'} \boldsymbol{\rho}_k \boldsymbol{\rho}_{k'} + \frac{\langle \boldsymbol{\rho} \rangle^2}{2M} + \sum_{k=1}^{K} \frac{U_k}{q_k} \\ & + \sum_{i=1}^{N} \frac{Q_i^2}{2m_i} \mathbf{A}^2(\mathbf{r}_i, t) - \sum_{i=1}^{N} \frac{Q_i}{m_i} \tilde{\mathbf{p}}_i \cdot \mathbf{A}(\mathbf{r}_i, t) + \sum_{i=2}^{N} V_{H,i} \\ & , \end{aligned} \tag{3.37}$$

where $\tilde{\mathbf{p}}, \mathbf{r}$ are expressed in terms of $\boldsymbol{\rho}$ and $\mathbf{q}$ via Eqs. (3.5) and (2.15). In addition, $\sum_{i=2}^{N} V_{H,i}$ in regularized coordinates is given by

$$\sum_{i=2}^{N} V_{H,i} = \sum_{i=2}^{N} \frac{\xi^2}{4\alpha\mu q_{i-1}^2} \exp\left\{ \alpha \left[1 - \left(\frac{q_{i-1} p_{i,1}}{\xi} \right)^4 \right] \right\} \tag{3.38}$$

In Eq. (3.37), U_k is equal to $Q_i Q_j$. Using Eq. (3.37) and with

$$\begin{aligned} \frac{d\mathbf{q}_k}{dt} &= \frac{\partial H}{\partial \boldsymbol{\rho}_k} \quad , \quad \frac{d\boldsymbol{\rho}_k}{dt} = -\frac{\partial H}{\partial \mathbf{q}_k} \\ \frac{d\langle \mathbf{q} \rangle}{dt} &= \frac{\partial H}{\partial \langle \boldsymbol{\rho} \rangle} \quad , \quad \frac{d\langle \boldsymbol{\rho} \rangle}{dt} = -\frac{\partial H}{\partial \langle \mathbf{q} \rangle} \end{aligned} \tag{3.39}$$

we obtain Hamilton's equations of motion

$$\begin{aligned}
\frac{d\mathbf{q}_k}{dt} &= 2\sum_{k'=1}^{K} T_{kk'}\boldsymbol{\rho}_{k'} - \sum_{i=1}^{N}\frac{Q_i}{m_i}\alpha_{ik}\mathbf{A}(\mathbf{r}_i,t) + \sum_{i=2}^{N}\frac{\partial V_{H,i}}{\partial \boldsymbol{\rho}_k} \\
\frac{d\langle\mathbf{q}\rangle}{dt} &= \frac{1}{M}\langle\boldsymbol{\rho}\rangle - \sum_{i=}^{N}\frac{Q_i}{M}\mathbf{A}(\mathbf{r}_i,t) \\
\frac{d\boldsymbol{\rho}_k}{dt} &= \frac{U_k\mathbf{q}_k}{q_k^3} + \sum_{i=1}^{N}\frac{Q_i}{m_i}\left[\tilde{\mathbf{p}}_i - Q_i\mathbf{A}(\mathbf{r}_i,t)\right]\cdot\frac{\partial\mathbf{A}(\mathbf{r}_i,t)}{\partial\mathbf{q}_k} - \sum_{i=2}^{N}\frac{\partial V_{H,i}}{\partial\mathbf{q}_k} \\
\frac{d\langle\boldsymbol{\rho}\rangle}{dt} &= \sum_{i=1}^{N}\frac{Q_i}{m_i}\left[\tilde{\mathbf{p}}_i - Q_i\mathbf{A}(\mathbf{r}_i,t)\right]\cdot\frac{\partial\mathbf{A}(\mathbf{r}_i,t)}{\partial\langle\mathbf{q}\rangle} - \sum_{i=2}^{N}\frac{\partial V_{H,i}}{\partial\langle\mathbf{q}\rangle}
\end{aligned} \tag{3.40}$$

where the derivatives of $V_{H,i}$ are given in Appendix E.

3.2.3.3 Propagation technique

To integrate the equations of motion in Eq. (3.40), we use a leapfrog technique [103, 104] jointly with the Bulirsch-Stoer method [105, 106]. This leapfrog technique was previously developed to study non-dipole effects in non-sequential double ionization in strongly driven H_2 [86]. This leapfrog technique allows to solve Hamilton's equations when the derivative of the position and the momentum depends on the quantities themselves. It is an extension of the leapfrog technique that was employed for strongly driven two-electron molecules in the dipole approximation [56]. In the latter case the derivative of the position and the momenta do not depend on themselves.

3.2.4 Vector potential

Here, we employ a vector potential of the form

$$\mathbf{A}(y,t) = -\frac{E_0}{\omega}\exp\left[-2\ln(2)\left(\frac{ct-y}{c\tau}\right)^2\right]\sin(\omega t - ky)\hat{\mathbf{z}}, \tag{3.41}$$

where $k = \omega/c$ is the wave number of the laser field and τ is the full width at half maximum of the pulse duration in intensity. The direction of both the vector potential and the electric field is along the z axis. We take the propagation direction of the laser field to be along the y axis and hence the magnetic field points along the

x axis.

3.2.5 Initial conditions of the three electrons

3.2.5.1 Ionization rates

In both methods, electron 2 tunnel-ionizes at time t_0 through the field-lowered Coulomb-barrier with a rate that is described by the quantum mechanical Ammosov-Delone-Krainov (ADK) formula [76, 107].

$$\begin{aligned} W_{ADK}(E) = & \frac{C_l^2}{2^{|m|}|m|!}\frac{(2l+1)(l+|m|)!}{2(l-|m|)!} \\ & \times \frac{1}{\kappa^{2Z_c/\kappa-1}}\left(\frac{2\kappa^3}{E}\right)^{2Z_c/\kappa-|m|-1}\exp\left(-2\kappa^3/3/E\right) \end{aligned} \tag{3.42}$$

where l and m are the angular and magnetic quantum numbers of the valence electrons, E is the field strength and Z_c is the effective charge seen by the ionizing electron due to the core. We take l=1 for the p orbitals, and since we assume that the electron tunnels from the p orbital along the field axis, we take m=0. Indeed, the m=0 case is more likely to ionize than the m=$\pm$1 by a factor of $\frac{2\kappa^3}{E}$ which is roughly 33 at an intensity of 0.5 PW/cm^2 for Ar. C_l measures the amplitude of the electron wavefunction in the tunneling region and $\kappa = \sqrt{2I_{p,1}}$. The former is derived from the ground-state wavefunction calculated from a model potential, see Tab. 2 in Ref. [108] . With the above choices of m and l, Eq. (3.42) becomes

$$W_{ADK}(E) = \frac{3C_l^2}{2}\frac{1}{\kappa^{2Z_c/\kappa-1}}\left(\frac{2\kappa^3}{E}\right)^{2Z_c/\kappa-1}\exp\left(-2\kappa^3/3/E\right). \tag{3.43}$$

To obtain the ADK rate, we use the value of the energy needed to ionize one electron from Ar, i.e. we use $I_{p,1}$ = 0.579 a.u and Z_c = 1.

3.2.5.2 Importance sampling

We find t_0, using importance sampling [75] in the time interval [-2τ,2τ] where the electric field is non-zero; τ is the full width at half maximum of the pulse duration in intensity; see Sec. 2.2.2.3. The importance sampling distribution is given by the ADK ionization rate.

3.2.5.3 Exit point

The exit point of electron 2 is along the direction of the laser field and is computed using parabolic coordinates [109]; see Appendix. A . The initial momentum of the tunneling electron is the same as in Sec. 2.2.2.4. That is, the momentum of electron 2 is taken to be equal to zero along the laser field. The transverse momentum is given by a Gaussian distribution which represents the Gaussian-shaped filter with an intensity-dependent width arising from standard tunneling theory [76–78].

3.2.5.4 Position and momentum distributions of the bound electrons in the H model

In the Heisenberg potential, see Eq. (3.33), for a given α, we find the value of ξ that ensures that the minimum of the one-electron Hamiltonian

$$H_i = \frac{\mathbf{p}_i^2}{2m_i} + \frac{Q_1 Q_i}{|\mathbf{r}_1 - \mathbf{r}_i|} + \frac{\xi^2}{4\alpha\mu r_{i,1}^2} \exp\left\{\alpha\left[1 - \left(\frac{r_{i,1}p_{i,1}}{\xi}\right)^4\right]\right\} \tag{3.44}$$

corresponds to the third ionization potential of Ar ($I_{p,3} = 1.497$ a.u.) [110–112]. To minimize Eq. (3.44) with respect to the relative distance $r_{i,1}$, we start from the lower limit of the constraint

$$r_{i,1}p_{i,1} = \xi \Rightarrow p_{i,1} = \xi / r_{i,1} \tag{3.45}$$

Since the mass of the core $m_1 \gg m_i$ it follows that $p_{i,1} \approx p_i$. Hence, Eq. (3.45) can be written as $p_i = \xi / r_{i,1}$ and substituting in Eq. (3.44) we obtain

$$H_i = \frac{\xi^2}{2m_i r_{i,1}^2} + \frac{Q_1 Q_i}{r_{i,1}} + \frac{\xi^2}{4\alpha\mu r_{i,1}^2}. \tag{3.46}$$

The minimum of Eq. (3.46) with respect to $r_{i,1}$, occurs at

$$r_{i,1}^{\min} = -\frac{2\alpha\mu + m_i}{2\alpha\mu m_i Q_1 Q_i}\xi^2, \tag{3.47}$$

and the energy is given by

$$H_i^{\min} = -\frac{\alpha\mu m_i (Q_1 Q_i)^2}{(m_1 + 2\alpha\mu)\xi^2}. \tag{3.48}$$

Setting this energy equal to $I_{p,3}$, we find $\xi = 1.55$ a.u for $\alpha = 2$ and $\xi = 1.63$ a.u. for $\alpha = 4$. Hence, for $\alpha = 2$ the electrons access a larger phase space during the time propagation.

To find the initial position and momentum vectors of the two initially bound electrons at time t_0, we apply a trial and error method similar to the one proposed by Cohen [97]. First, we randomly sample the magnitude of the position and the momentum vector for each electron in the intervals $[0, r_{max}], [0, p_{max}]$. The θ, ϕ polar and azimuthal angles of the position and the momentum of electrons 3 and 4 are obtained as uniform random numbers of $\cos\theta$ in the interval [-1,1] and ϕ in the interval $[0,2\pi]$. Using the position and momenta of electrons 3 and 4, we determine the total energy of the two electrons in the absence of the electric field

$$H_{3,4} = \sum_{i=3}^{4} \frac{\mathbf{p}_i^2}{2} + \sum_{i=3}^{4} \frac{Q_1 Q_i}{|\mathbf{r}_1 - \mathbf{r}_i|} + \sum_{i=3}^{4} V_{H,i} + \frac{Q_3 Q_4}{|\mathbf{r}_3 - \mathbf{r}_4|}. \tag{3.49}$$

If the energy $H_{3,4}$ is within 1% of the binding energy $-(I_{p,2} + I_{p,3})$, we accept the initial conditions of electron 3 and 4, otherwise we reject them. For Ar, the energy to ionize a second electron is $I_{p,2} = 1.015$ a.u. We find that to satisfy the above condition, it is sufficient to consider $r_{max} = 3$ a.u. and $p_{max} = 3$ a.u. Using the above procedure, we plot in Fig. (3.3), the probability distribution of the initial position and momentum of electrons 3 and 4 as well as of the Heisenberg potential.

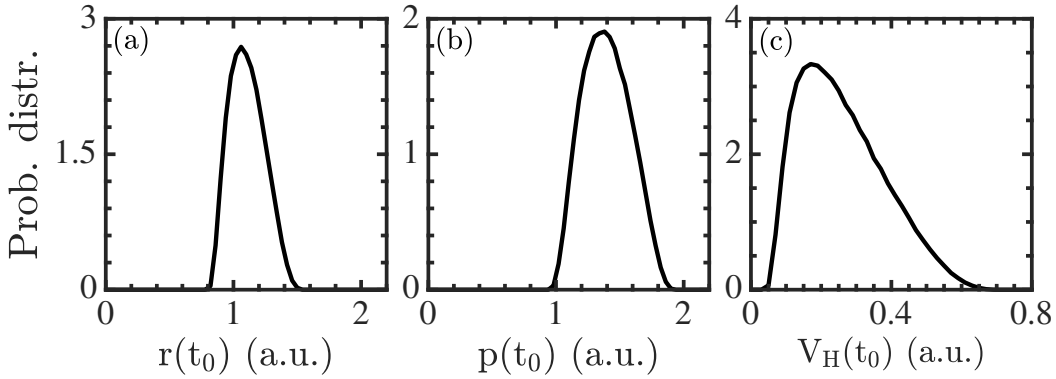

Figure 3.3: Probability distribution of r (a) and p (b) for each of the electrons 3, 4 as well as the Heisenberg potential V_H (c) at time t_0, for $\alpha = 2$.

3.2.5.5 Position and momentum distributions of the bound electrons in the ECBB model

In the ECBB model, we obtain the initial position and momentum of electron 4 at time t_0 using a microcanonical distribution with an energy

$$\mathcal{E}_4(t_0) = \frac{\mathbf{p}_4^2}{2m_4} + \frac{Q_1 Q_4}{|\mathbf{r}_1 - \mathbf{r}_4|} + V_{\text{eff}}(\zeta_3, |\mathbf{r}_1 - \mathbf{r}_4|), \tag{3.50}$$

and similarly for electron 3. We take the energy $\mathcal{E}_3(t_0) = \mathcal{E}_4(t_0) = -I_{p,2}$ and using Eq. (3.13) we find that $\zeta_3(t_0) = \zeta_4(t_0) = (Q_1/\mathcal{E}_{1s})\mathcal{E}_3(t_0)$. The reason we set the initial energy of each electron equal to $-I_{p,2}$ is that $\mathcal{E}_4(t_0)$ and $\mathcal{E}_3(t_0)$ include the interaction with the other electron via V_{eff}. Hence, $\mathcal{E}_3(t_0)$ and $\mathcal{E}_4(t_0)$ correspond to the energy needed to remove an electron from Ar^+. Using the above defined microcanonical distribution, we obtain the initial position and momentum of each bound electron [113]. In Fig. (3.4), we plot the probability distribution for the initial position and momentum of electrons 3 and 4 as well as of the V_{eff}. The microcanonical distribution is obtained in the absence of the electric field. However, at time t_0 the electric field is present and the electron energies change due to the presence of the dipole term $-Q_j \mathbf{r}_j \cdot \mathbf{E}(\mathbf{r}_j, t)$ in Eq. (3.14). Furthermore, the energy of the bound electron i depends on the values of ζ for the other bound electrons. Hence, to allow the electron energies to become self-consistent once the field is turned on, we perform a simple iteration. Namely, we first calculate the energies of the bound electrons using Eq. (3.14) with the charges ζ computed in the absence of the electric field. We then recalculate the charges ζ for all the bound electrons using Eq. (3.14). This procedure is repeated until the difference between all the electron energies from the current to the previous iteration is less than a threshold value and no more than 100 iterations are performed. We take the threshold value to be 1×10^{-16}, which exceeds the precision of double variables in c++. The trajectories where 100 iterations are reached and the difference between the energies is bigger than the threshold value, are not of concern in the studies of Ar and Ne since we have found that the discarded trajectories during time propagation in our codes are

less than 0.03%.

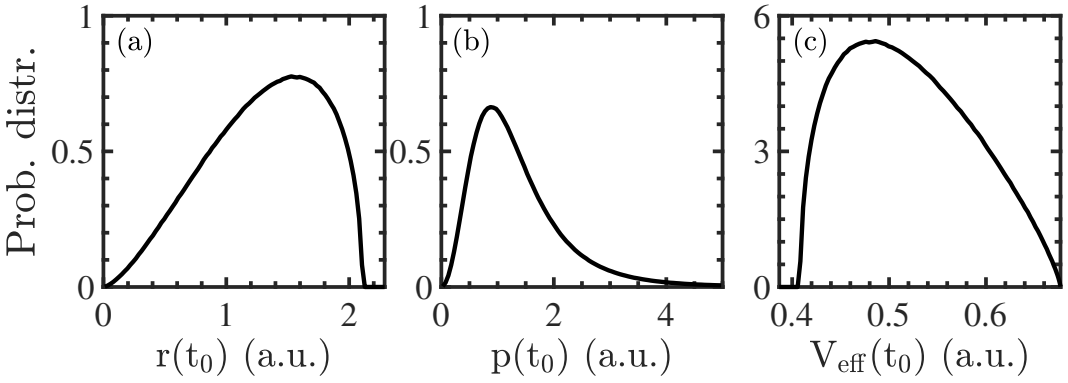

Figure 3.4: Probability distribution of r (a) and p (b) for each of the electrons 3, 4 as well as the effective Coulomb potential V_{eff} (c) at time t_0.

3.2.6 Probabilities for ionization processes

The time propagation of strongly-driven Ar starts at time t_0 and stops at an asymptotically large time t_f. For each trajectory, if the energies of three (two) electrons are positive, we label the trajectory as a triple (double) ionization event. The DI and TI probabilities are

$$P_{DI} = \frac{N_{DI}}{N},\ P_{TI} = \frac{N_{TI}}{N}, \tag{3.51}$$

where N_{DI}, N_{TI} and N are the numbers of doubly-ionized, triply-ionized and all events, respectively. To identify a recollision in either one of the two models, we monitor the Coulomb potential between all pairs of a quasifree and a bound electron. We identify the maxima in the inter-electronic Coulomb potential energy as function of time. We label the times when the inter-electronic distance is minimum as recollision times t_{rec}. Also, we define the ionization time of electron i, t^i_{ion}, to be the time when the compensated energy becomes positive and remains positive thereafter [87]. We used the same definition for t^i_{ion} in all our previous studies, see for instance [36, 39]. The compensated energy is given by

$$\varepsilon_i^{comp}(t) = \frac{\tilde{\mathbf{p}}_i^2}{2m_i} + \frac{Q_1 Q_i}{|\mathbf{r}_1 - \mathbf{r}_i|} + \sum_{\substack{j=2 \\ j\neq i}}^{N} c_{i,j}(t) V_{eff}(\zeta_j, |\mathbf{r}_1 - \mathbf{r}_i|),$$

$$\varepsilon_i^{comp}(t) = \frac{\tilde{\mathbf{p}}_i^2}{2m_i} + \frac{Q_1 Q_i}{|\mathbf{r}_1 - \mathbf{r}_i|} + V_{H,i},$$

for the ECBB and the H model respectively. Moreover, a TI or DI event is labelled as direct if the energy transferred from a recolliding electron to bound electrons suffices for the simultaneous ionization, shortly after recollision, of three or two electrons. A TI or DI event is labelled as delayed if following a recollision, not all electrons ionize shortly after the recollision. If the energy transferred is only enough to ionize two or one electrons shortly after recollision, the TI or DI event is labelled as delayed. Below we outline the algorithm used to label an event as direct.

3.2.6.1 Identifying pathways of TI and DI events

We obtain the TI and DI events with a code that incorporates the formulation of the ECBB model described in Sec. 3.2.2 and a code that incorporates the formulation of the H model described in Sec. 3.2.3. Once we obtain these events, we perform a detailed analysis with a different set of codes. In both analysis codes, i.e. one for each model, we use the framework we developed in Sec. 3.2.2.7 to determine on the fly during propagation if an electron is quasifree or bound. We register a TI or DI event as direct (delayed) if a recollision is (is not) associated with the simultaneous ionization of three or two electrons. We take the following steps to identify direct events:

1. We find the ionization time of each electron, t_{ion}^i, with i = 2,3,4 for TI and i = 2,3 for DI.

2. We register the maxima in the inter-electronic potential energies as a function of time between electron pairs i,j and i,k and j,k during the time intervals when in these pairs one electron is quasifree and the other is bound. Next, for each electron i, we identify the maximum for each one of the i,j and i,k potential energies that is closest to the time t_{ion}^i. We denote these times as $t_{rec}^{i,j}$ and $t_{rec}^{i,k}$. We obtain at most six such times for TI events and four for DI events.

3. For each time $t_{rec}^{i,j}$ we identify the time t_2 (see Sec. 3.2.2.7) of closest approach to the core of the quasifree electron (either electron i or j) that is closest to $t_{rec}^{i,j}$

and denote it as $t_2^{i,j}$. We obtain at most six such times for TI events and four for DI events.

We label a TI event as direct if four of the times $t_2^{i,j}$ are the same, accounting for one electron being quasifree and the other two bound. That is, if electron i is quasifree during the recollision closest to the ionisation time t_{ion}^{i} then the times $t_2^{i,j}$, $t_2^{i,k}$, $t_2^{j,i}$ and $t_2^{k,i}$ should be the same. The times $t_2^{j,i}$ and $t_2^{k,i}$ are associated with the recollision times $t_{rec}^{j,i}$ and $t_{rec}^{k,i}$ for the bound electron j and k respectively. For the quasifree electron we obtain two recollision times $t_{rec}^{i,j}$ and $t_{rec}^{i,k}$ associated with the ionization time t_{ion}^{i}. We choose the one that has the largest difference from t_{ion}^{i}, guaranteeing a stricter criterion for direct TI events. Next, we check whether $\Delta t_1 = |t_{rec}^{i,j} - t_{ion}^{i}| < t_{diff}$ or $(t_{ion}^{i} < t_{rec}^{i,j}$ & $t_{ion}^{i} < t_{rec}^{i,k})$ and $\Delta t_2 = |t_{rec}^{j,i} - t_{ion}^{j}| < t_{diff}$ and $\Delta t_3 = |t_{rec}^{k,i} - t_{ion}^{k}| < t_{diff}$. If the latter conditions are satisfied then we label the event as direct TI. The condition $(t_{ion}^{i} < t_{rec}^{i,j}$ & $t_{ion}^{i} < t_{rec}^{i,k})$ has also been used in previous studies [40, 41] to account for a quasifree electron ionising significantly earlier before recollision. This happens mostly at high intensities. We label events as delayed pathway TI with only one electron ionizing shortly after recollision, if two out of the three times Δt_1, Δt_2 and Δt_3 are larger than t_{diff} and one is less than t_{diff}. We also label delayed pathway TI with two electrons ionizing shortly after recollision, if one out of the three times Δt_1, Δt_2 and Δt_3 is larger than t_{diff} and two are less than t_{diff}. A similar process is followed to identify direct and delayed DI events. The time t_{diff} is determined by the time interval where the interelectronic potential energy undergoes a sharp change due to a recollision. For the intensities considered here, we find $t_{diff} \approx T/8$, with T being the period of the laser field.

3.3 Results for strongly driven Ar

In what follows, we compare observables for triple ionization (TI) and double ionization (DI) obtained with the ECBB model and the H model. If available, we also compare these observables with experimental results [30, 31]. In our formulation both the ECBB model and the H model fully account for non-dipole effects and treat the motion of the electrons and the core on an equal footing. We study Ar driven by

a laser pulse with intensities ranging from $2\times10^{14}\mathrm{W/cm^2}$ to $5\times10^{14}\mathrm{W/cm^2}$ and durations of $\tau = 20$ fs, 25 fs and 30 fs at 800 nm.

Here, we mainly focus on non-sequential double ionization (NSDI) and on non-sequential triple ionization (NSTI) events. NSDI and NSTI involve an electron accelerating in the laser field and coming back to the core to transfer energy to bound electrons via a recollision. This energy transfer can lead to the escape of two electrons (NSDI) or three electrons (NSTI). Electronic correlation, a fundamental interaction, underlies this field-assisted recollision [12, 114].

3.3.1 Triple and double ionization probabilities

We find that the DI and TI probabilities are consistently larger for the H model for both $\alpha = 2,4$ compared to the ECBB model. This is consistent with the different initial conditions the bound electrons have in the two models. The initial momenta of the bound electrons are higher in the H model versus the ECBB model, compare Fig. 3.3(b) with Fig. 3.4(b). Also, the repulsive Heisenberg potential reduces the attraction of each electron from the core resulting in higher ionization probabilities. Regarding the DI probability, for the H model, we find that at intensities 2×10^{14} $\mathrm{W/cm^2}$, 4×10^{14} $\mathrm{W/cm^2}$, and 5×10^{14} $\mathrm{W/cm^2}$ and 20 fs pulse duration the DI probability is consistently higher for $\alpha = 4$ compared to $\alpha = 2$. However, while at the two smallest intensities the difference in the DI probability is small for the two values of α, at 5×10^{14} $\mathrm{W/cm^2}$ the DI probability is almost 71 % higher for $\alpha = 4$ compared to $\alpha = 2$. Hence, the DI probability depends significantly on the value of α, a disadvantage of the H model. In what follows, we consider $\alpha = 2$ for the H model, unless otherwise stated, since this value allows the electrons to access a larger phase space. As we increase the intensity from 2×10^{14} $\mathrm{W/cm^2}$ to 5×10^{14} $\mathrm{W/cm^2}$, we find that the ratio of the DI probabilities between the two models, $\mathrm{P_{DI}^{ECBB}/P_{DI}^{H}}$, decreases from 1.1 to 0.4. However, the ratio of the TI probabilities $\mathrm{P_{TI}^{ECBB}/P_{TI}^{H}}$ increases from 0.03 to 0.2. Hence, for the intensities considered here, the DI and TI probabilities are smaller for the ECBB model.

3.3.2 Distribution of the sum of the electron momenta and recollision pathways

In Fig. 3.5, we plot the TI and DI probability distribution of the sum of the p_z momenta of the ionizing electrons at intensities 2×10^{14} W/cm^2, 4×10^{14} W/cm^2 and 20 fs pulse duration and 5×10^{14} W/cm^2 and 25 fs pulse duration. The highest intensity pulse allows for a direct comparison with experimental results [28]. In Figs. 3.5(a1) and 3.5(a2), for the ECBB model, we plot the TI and DI probability distributions of the sum of the p_z momenta of the ionizing electrons. For DI (Fig. 3.5(a2)), we find that the probability distribution is centered around zero and the width decreases with increasing intensity. This is in accord with previous findings for two-electron Ar driven by a 4 fs pulse for intensities from 2×10^{14} W/cm^2 to 5×10^{14} W/cm^2[40]. For TI (Fig. 3.5(a1)), we find similar doubly-peaked distributions for 4×10^{14} W/cm^2 and 5×10^{14} W/cm^2. The TI probability at 2×10^{14} W/cm^2 is very low and we do not consider this intensity in Fig. 3.5(a1).

In Figs. 3.5(b1) and 3.5(b2), for the H model for $\alpha=2,4$, we plot the TI and DI probability distributions of the sum of the p_z momenta of the ionizing electrons. For DI (Fig. 3.5(b2)), we find that the probability distribution is centered around zero and the width decreases with increasing intensity for both α. For TI (Fig. 3.5(b1)), we find that at 2×10^{14} W/cm^2 the distribution is doubly-peaked, while at higher intensities the distribution is centered around zero. Finally, we find that the TI distributions are similar for the two values of α, while the DI distributions are more centered around zero for $\alpha=4$. This is consistent with each electron being less attracted from the core for larger values of α resulting in smaller final momenta. Hence, the probability distributions depend on the value of α.

Comparing the TI (Fig. 3.5(c1)) and DI (Fig. 3.5(c2)) probability distributions of the ECBB and H model for $\alpha=2$, we find that all distributions are more centered around zero for the H model. Moreover, the TI distributions at higher intensities are doubly-peaked for the ECBB model and centered around zero for the H model.

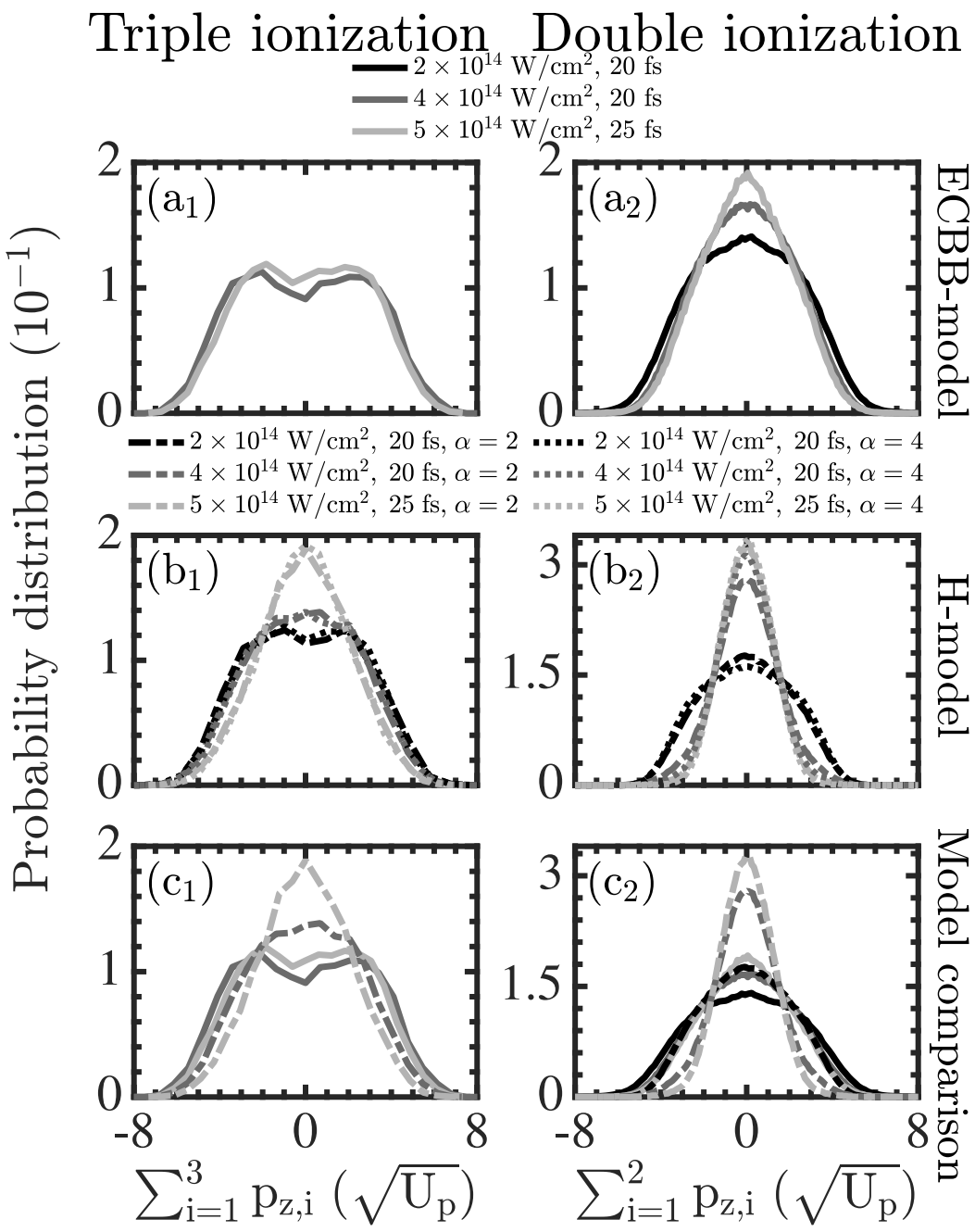

Figure 3.5: Probability distributions of the sum of the electron momentum components parallel to the polarization of the laser field for TI (left column) and DI (right column) at intensities 2×10^{14} W/cm^2 (20 fs), 4×10^{14} W/cm^2 (20 fs) and 5×10^{14} W/cm^2 (25 fs). The ECBB model results are presented in the top row, the H model in the middle row and comparison of the two models in the third row. All probability distributions are normalized to one.

In Fig. 3.6, we plot, the TI and DI distributions of the sum of the p_z electron momenta for the direct (top row) and delayed pathway (bottom row). Only in this

section of this thesis we refer to all non-direct events as delayed pathways for simplicity. Hence, here, the delayed events also include TI and DI no-recollision events. The latter account for roughly 7 % of DI and 4 % of TI events for the H and zero for the ECBB model.

For the direct pathway, we find that the TI (Fig. 3.6(a1)) and DI (Fig. 3.6(a2)) distributions are double-peaked for both the ECBB and the H model. For TI events the distributions have peaks at larger values of momenta compared to DI events, with the peaks for TI being around $\pm 4\sqrt{U_p}$ and for DI around $\pm 2.5\sqrt{U_p}$. The ponderomotive energy $U_p = E_0^2/(4\omega^2)$ is the average energy an electron gains from the laser field. Also, for DI events, the distributions have more events centered around zero for the ECBB compared to the H model. This contribution increases with increasing intensity, which is consistent with our previous results of double ionization of two-electron Ar driven by short pulses [40]. We find the percentage of direct events to be significantly larger for the ECBB compared to the H model. The contribution of direct events to DI is roughly 50 % for the ECBB model, while it decreases from 16 % to 5 % with increasing intensity for the H model. The contribution of direct events to TI is roughly 20 % for the ECBB model while it is roughly 5 % for the H model at the two highest intensities. For the delayed pathway, for DI, the distributions are centered around zero for both models (Fig. 3.6(b2)), while for TI the distributions are less centered around zero for the ECBB model (Fig. 3.6(b1)).

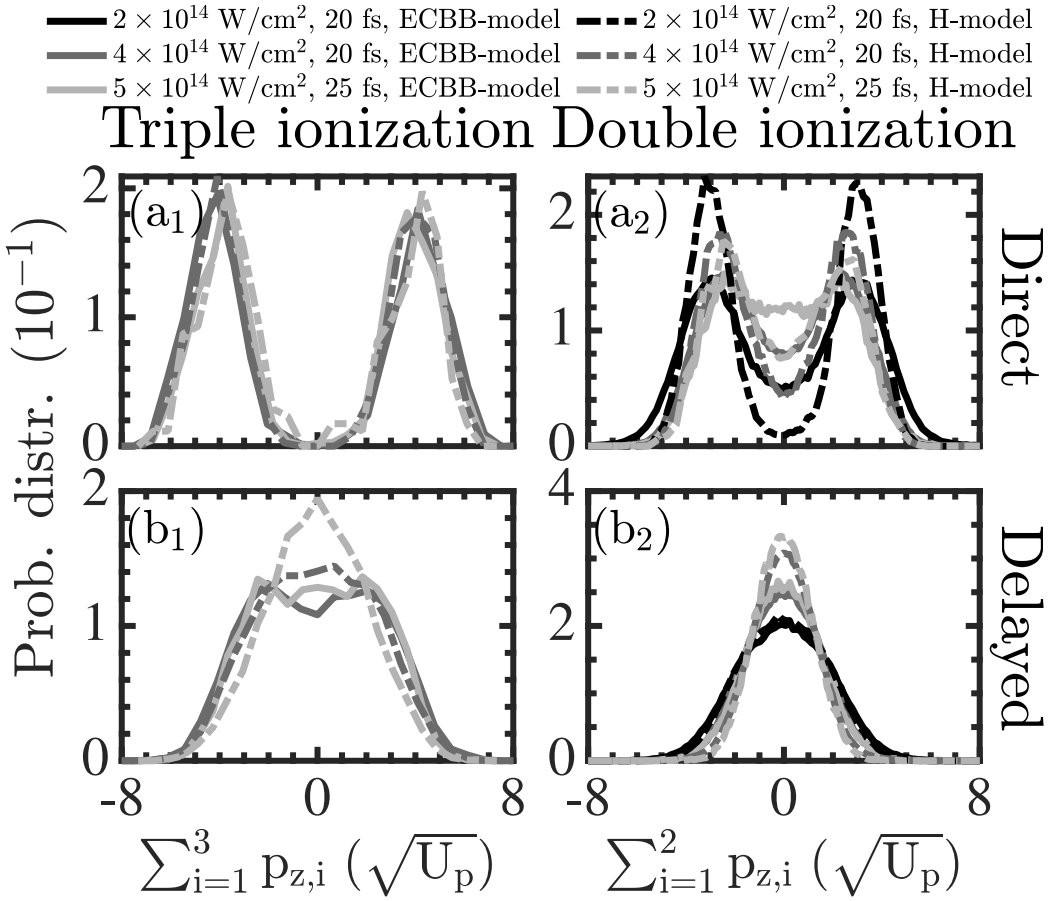

Figure 3.6: Probability distributions of the sum of electron momenta components parallel to the polarization of the laser field for TI (left column) and DI (right column) at intensities 2×10^{14} W/cm^2 (20 fs), 4×10^{14} W/cm^2 (20 fs) and 5×10^{14} W/cm^2 (25 fs). The direct pathway distributions are plotted on the top row and the delayed pathway distributions are plotted on the bottom row. All probability distributions are normalized to one.

Next, we compare with experimental results the findings of the ECBB and H model for the DI distribution of the sum of the p_z electron momenta of Ar at 4×10^{14} W/cm^2 (30 fs) (Fig. 3.7(c)) and 5×10^{14} W/cm^2 (25 fs) (Fig. 3.7(b)) [30, 31] as well as the TI distribution at 5×10^{14} W/cm^2 (25 fs) [31] (Fig. 3.7(a)). The experimental DI distributions have a slight double-peaked structure and agree more with the results of the ECBB model. Indeed, the H model produces DI distributions that are highly centered around zero, which is significantly less the case for the ECBB model. The experimental TI distributions have a slight doubly-peaked structure which is only reproduced by the ECBB model. However, the TI distribution obtained with the ECBB model is wider than the one obtained experimentally.

Hence, for DI the ECBB model better reproduces the experimental results while for TI is not clear whether the ECBB or the H model agree best with experiment. To answer this question a future study needs to compare distributions where intensity averaging has been accounted for in the theoretical results [40, 115].

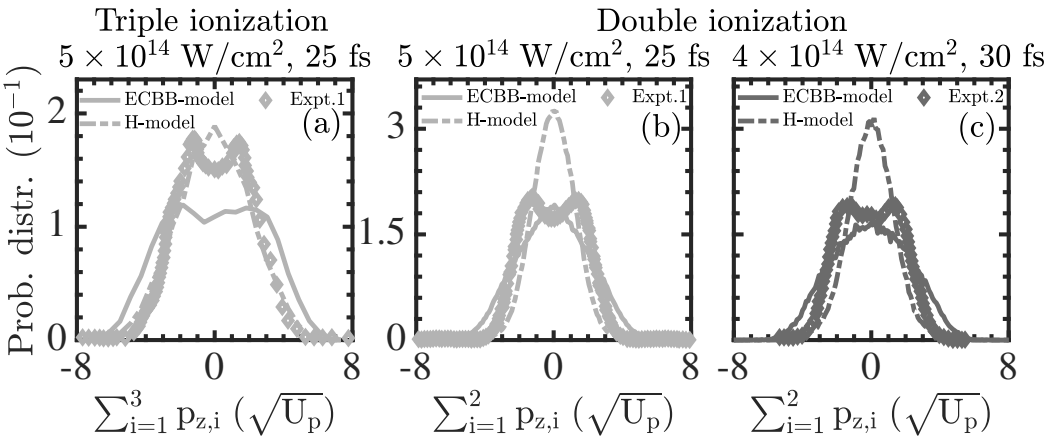

Figure 3.7: Probability distributions of the sum of electron momenta components parallel to the polarization of the laser field for TI (a) and DI (b) and (c) at intensities 5×10^{14} W/cm^2 (25 fs) (a) and (b) and 4×10^{14} W/cm^2 (30 fs) (c). We compare the distributions obtained with the ECBB and H model with experimental ones [30, 31]. All probability distributions are normalized to one.

3.3.3 Strength of the recollision in DI and TI events

For each DI and TI event we register all the maxima of the Coulomb inter-electronic potential energy as a function of time and identify the largest maximum V_{max}. That is, we identify the most important recollision for each event. We plot the distribution of V_{max} for TI (Fig. 3.8(a)) and DI (Fig. 3.8(b)) events. We find that recollisions are significantly stronger for the ECBB model, with the most probable value of V_{max} being roughly 1 a.u. for DI and TI at all intensities. In contrast, for the H model, at the higher intensities, the most probable value of V_{max} is close to 0 a.u. both for DI and TI. For the H model, weaker recollisions are consistent with the DI and TI distributions of the sum of the p_z electron momenta being more centered around zero, see Fig. 3.5.

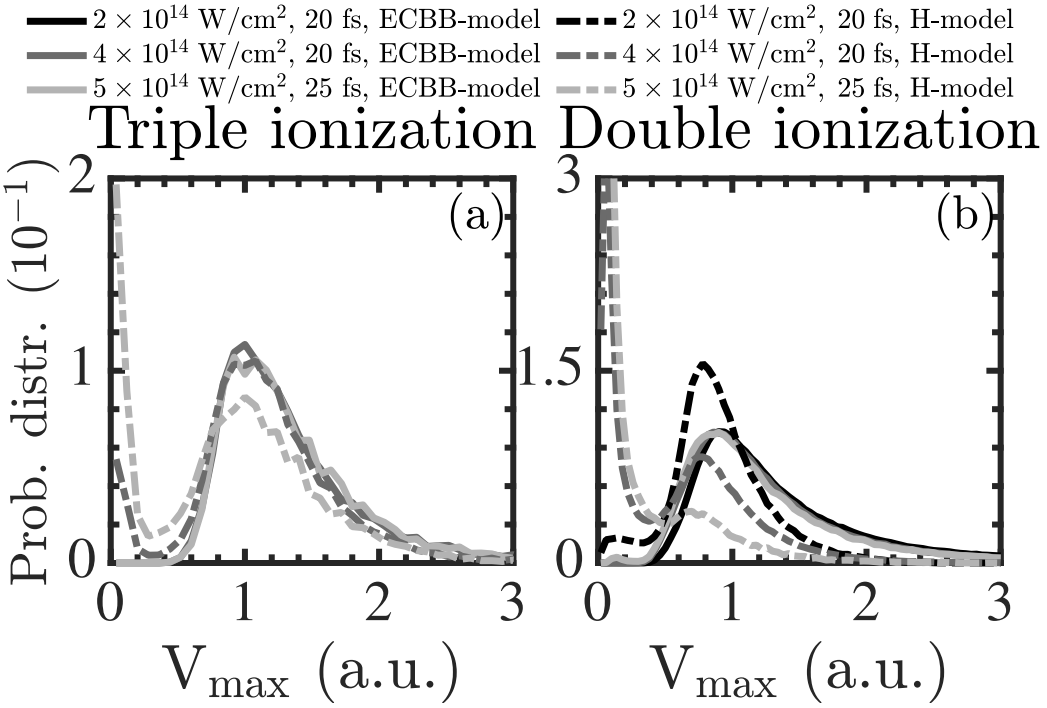

Figure 3.8: Probability distributions of the largest value of the Coulomb inter-electronic potential energy for TI (a) and DI (b) at intensities 2×10^{14} W/cm^2 (20 fs), 4×10^{14} W/cm^2 (20 fs) and 5×10^{14} W/cm^2 (25 fs). All probability distributions are normalized to one.

3.3.4 Correlated electron momenta

In Fig. 3.9, for DI, we plot the correlated electron momenta at intensities 2×10^{14} W/cm^2 (20 fs), 4×10^{14} W/cm^2 (20 fs) and 5×10^{14} W/cm^2 (25 fs) obtained with the ECBB model ((a1)-(a3)) and the H model ((b1)-(b3)). At the three intensities, we find that correlated electron escape prevails mostly for the ECBB model which produces roughly 10 % more correlated events than the H model. Also, at intensities 4×10^{14} W/cm^2 and 5×10^{14} W/cm^2, the electrons escape with considerably higher momenta in the ECBB model, compare Fig. 3.9 (a2) with Fig. 3.9 (b2) and Fig. 3.9 (a3) with Fig. 3.9 (b3). The above are consistent with the ECBB model resulting in more direct events (Sec. 3.3.2) and stronger recollisions (Fig. 3.8) than the H model.

In Fig. 3.10, for TI, we plot the correlated electron momenta at intensities 4×10^{14} W/cm^2 (20 fs) and 5×10^{14} W/cm^2 (25 fs) obtained with the ECBB model ((a1)-(a2)) and the H model (b1)-(b2)). We find that correlated three electron-escape

is clearly prevalent at both intensities for the ECBB model, while this is barely the case for the H model. Moreover, the three electrons escape with significantly smaller momenta for the H model compared to the ECBB model, compare Fig. 3.10 (a1) with Fig. 3.10 (b1) and Fig. 3.10 (a2) with Fig. 3.10 (b2). As for DI, this is consistent with the ECBB model yielding more direct events and stronger recollisions versus the H model.

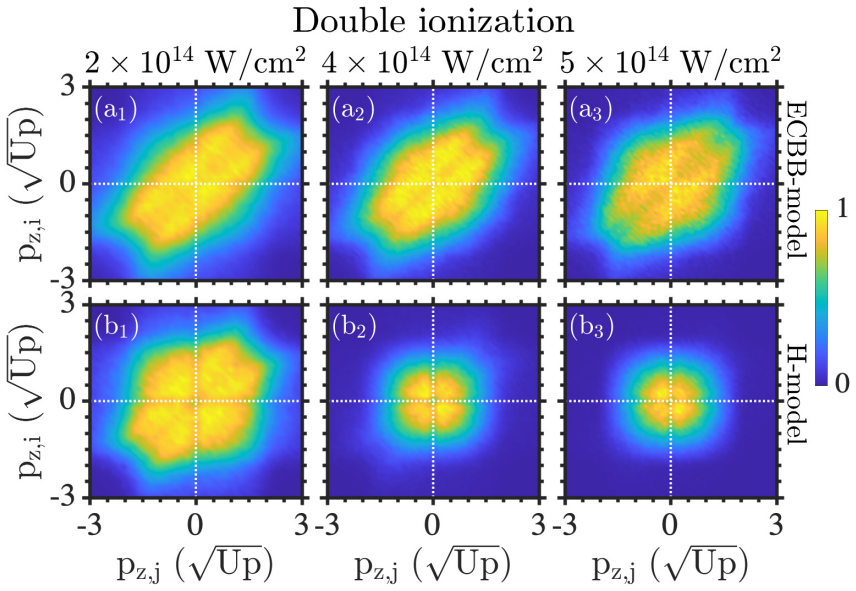

Figure 3.9: Symmetrized correlated momenta of all pairs of escaping electrons for DI for the ECBB model (a1)-(a3) and the H model (b1)-(b3) at intensities 2×10^{14} W/cm^2 (20 fs), 4×10^{14} W/cm^2 (20 fs) and 5×10^{14} W/cm^2 (25 fs). The doubly differential distributions are divided by the peak value.

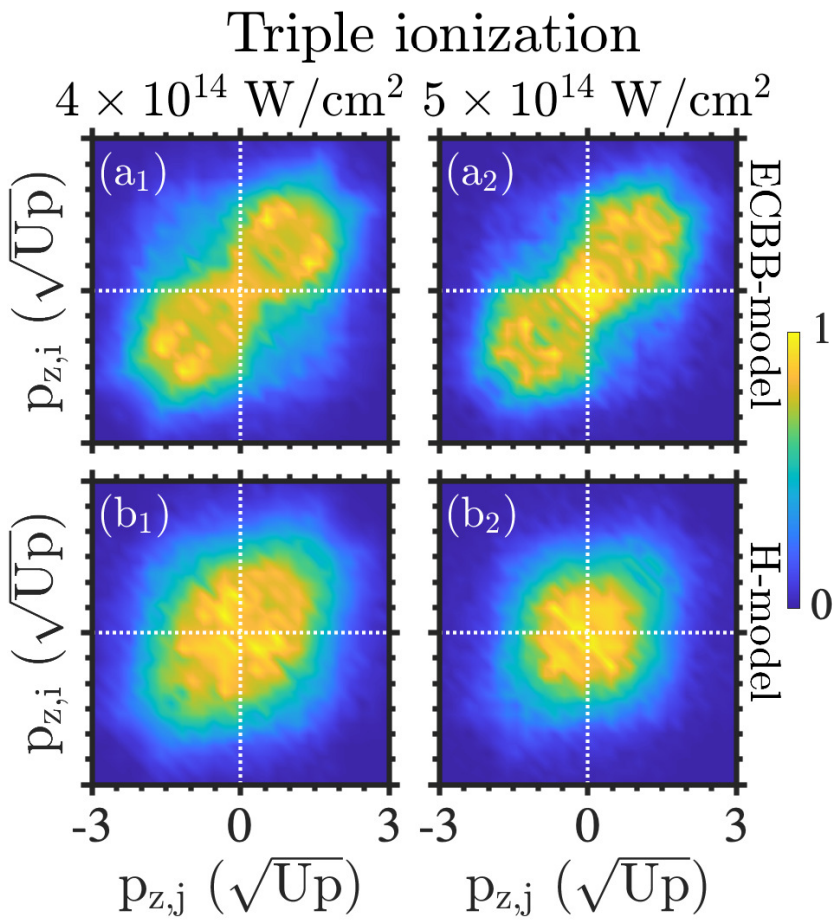

Figure 3.10: Symmetrized correlated momenta of all pairs of escaping electrons for TI for the ECBB model (a1)-(a2) and the H model (b1)-(b2) at intensities 4×10^{14} W/cm^2 (20 fs) and 5×10^{14} W/cm^2 (25 fs). The doubly differential distributions are divided by the peak value.

3.3.5 Angular distributions of the three ionizing electrons

In Fig. 3.11, we plot the TI (left column) and DI (right column) probability distributions of the angles of the ionizing electrons and the core at intensity 4×10^{14} W/cm^2 at 20 fs. We obtain similar results for the other intensities considered in this work (not shown). We find that the angle between any pair of escaping electrons θ_{e-e} (black color) is mostly peaked at small angles indicating a correlated electron escape. For both the ECBB model and the H model, we find that the angle of inter-electronic escape is smaller for TI versus DI. This is consistent with the electron momenta being more correlated for TI versus DI, compare Fig. 3.9 with Fig. 3.10. We also find that a small angle of inter-electronic escape is significantly more favoured

by the ECBB model, which results in more direct events and stronger recollisions.

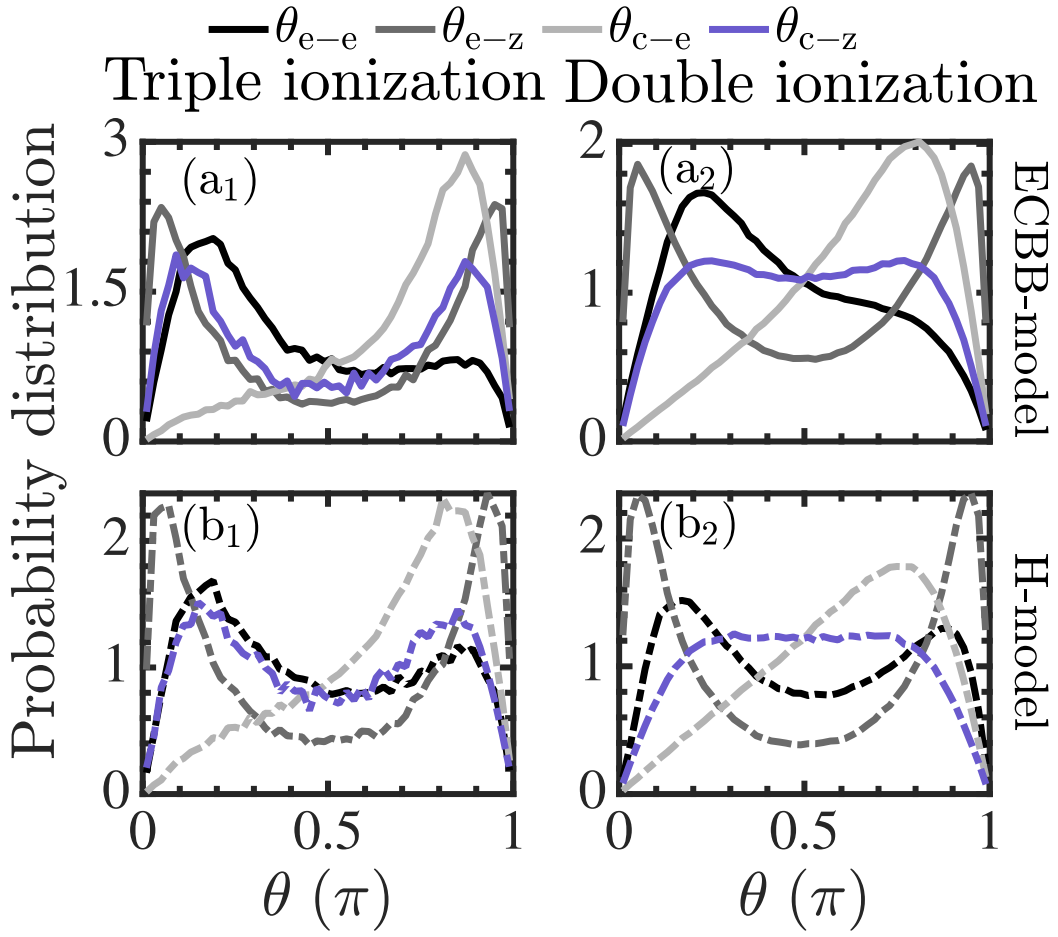

Figure 3.11: Probability distributions of the angles of the ionizing electrons and the core for TI (left column) and DI (right column) at 4×10^{14} W/cm^2 (20 fs). Plots for the ECBB model are denoted with solid lines versus broken lines for the H model. All probability distributions are normalized to one.

We also find that the angle of any escaping electron with the z axis, θ_{e-z}, (dark gray color) peaks at small and large values for TI and DI for both models. That is, the ionizing electrons escape mostly along (0°) or opposite (180°) the direction of the electric field. However, the peaks of the distributions of θ_{e-z} are sharper, i.e. the distributions are less wide, for the H model. This is in accord with our finding that the H model gives rise to a significantly higher number of TI and DI events where no-recollision takes place compared to the ECBB model. As a result, in the H model, the electrons ionize mostly due to the field for a larger number of events, with the electrons escaping more along or opposite the direction of the field.

Moreover, we find that the distributions of the angle of the core with the z axis, θ_{c-z}, (blue color) are wide for both TI and DI for both models. However, the distribution is wider for DI versus TI. This is consistent with the core having a higher charge equal to 3 for TI versus 2 for DI. As a result, the electric field exerts a larger force on the core in TI leading the core to escape more along or opposite the direction of the electric field. Finally, we find that the distribution of the angle θ_{c-e} (light grey color) between an ionizing electron and the core peaks mostly at large angles, that is, the electron and the core escape in opposite directions. This is consistent with the electric field exerting opposite forces to particles of opposite charges. We find that the angle of escape between an electron and the core is larger for TI compared to DI for both models. This is consistent with the larger core charge for TI resulting to the core escaping more along or opposite the field direction.

3.4 Conclusions

We formulate a 3D semi-classical model to address three-electron dynamics in a strongly driven atom where the electron and core dynamics are treated at the same time. Our formulation includes the magnetic field of the laser field as well as the Coulomb singularities. We address unphysical autoionization present in semi-classical models where the Coulomb singularities are accounted for and more than one electron is bound. We do so by substituting the Coulomb repulsion between bound electrons with effective potentials where an effective charge is associated with every bound electron. The interaction between pairs of electrons that are not both bound is accounted for with the full Coulomb potential and all other forces are fully accounted for. This model, developed in this work and referred to as the ECBB model, identifies on the fly during time propagation if an electron is bound or not. We compare the ionization spectra obtained with the ECBB model with the ones obtained with a model previously developed–referred to here as the H model. In the latter model, a potential is added for each electron that mimics the Heisenberg uncertainty principle and restricts the accessible phase space of each electron preventing autoionization. The advantage of the ECBB model is that it accurately

treats the interaction of each electron with the core and all other interactions while it treats less accurately the interaction between bound electrons. The advantage of the H model is that it accurately treats the interaction between all electrons while it treats less accurately the interaction of each electron with the core.

Using these 3D semi-classical models, we address triple and double ionization in a strongly-driven atom, namely Ar. We compare the ionization spectra obtained with the two models as well as with experiment for various pulse durations and intensities. We find that both double and triple ionization probabilities are greater for the H model compared to the ECBB model. We conjecture that this difference in the probabilities is due to the Heisenberg potential resulting in larger initial momenta of the bound electrons as well as in a significant less attraction of each electron from the core. We find that in the H model for a significant number of events the electrons ionize without a recollision, i.e. ionize due to the laser field and the recollisions are significantly weaker compared to the ECBB model. These findings are consistent with our results for the distribution of the sum of the momenta of the ionizing electrons along the direction of the laser field. For all the intensities and pulse durations considered here, we find that these distributions are broader for the ECBB model. For triple ionization, we find that the distributions of the sum of the electron momenta have a double peak for the ECBB model while they are centered around zero for the H model. We find this to be due to the ECBB model producing more direct ionization events than the H model. This is also evident in the correlated electron momenta where the distributions obtained with the ECBB model are consistently more correlated compared to the ones obtained with the H model. Moreover, we identify another disadvantage of the H model, namely, the distributions of the momenta and ionization probabilities depend on the parameter α in the Heisenberg potential. Comparing with experimental distributions of the sum of the momenta we find that the distributions obtained with the ECBB model have a better agreement with experiment mainly for double ionization. Finally, our formulation of the ECBB model and of the H model that account for electron and core motion and for non-dipole effects is general and can be generalized to strongly-driven atoms with

more than three electrons.

Chapter 4

Singularity in electron-core potential as a gateway to accurate multi-electron ionization spectra in strongly driven atoms

We demonstrate our general three-dimensional semiclassical model as a powerful technique for the study of correlated multi-electron escape in atoms driven by infrared laser pulses at intensities where electron-electron correlation prevails. We do so in the context of triple ionization of strongly driven Ne [3]. Our model fully accounts for the singularity in the Coulomb potentials of a recolliding electron with the core and a bound electron with the core as well as for the interaction of a recolliding with a bound electron. To avoid artificial autoionization, our model employs effective potentials to treat the interaction between bound electrons. We show the accuracy of our model by obtaining triple ionization distributions of the sum of the final electron momenta which we find to be in very good agreement with experiments. Also, we explain the main features of these momenta distributions in terms of the prevalent pathways of correlated three-electron escape in Ne. We also show that the different ionization pathways prevailing in three-electron escape in strongly driven Ne versus Ar give rise to different momenta distributions in these two atoms. Our general model may be used to identify novel ultrafast phenomena

and to motivate further experiments in strong field science.

4.1 Introduction

In this chapter, we further demonstrate the accuracy of the ECBB model in the context of correlated three-electron escape in strongly driven Ne. We show that the z-component of the sum of the final electron momenta has excellent agreement with experiment [28]. Here, the electric field is linearly polarized along the z axis. We have used the ECBB model in Chapter 3 to study triple ionization of strongly driven Ar [2]. However, the striking agreement with experiment for strongly driven Ne unveils the ECBB model as a powerful technique for studying correlated multi-electron ionization in driven atoms.

In addition, we compare our results for the sum of the final electron momenta for strongly driven neon with the H model as we did for Ar in Chapter 3. Our results show that, as for Ar, the ECBB model is significantly more accurate than the H model at describing strongly driven Ne. This is consistent with the fact that softening the Coulomb potential fails to accurately describe electron scattering from the core [34, 35]. Indeed, the ratio of the scattering amplitude for the soft-core potential over the one for the Coulomb potential decreases exponentially with increasing momentum transfer [34, 35]. For recollisions [12], this implies that soft potentials are quite inaccurate for high energy recolliding electrons that backscatter. Hence, it is no surprise that classical models that include the singularity in the Coulomb electron-core potential result in accurate double ionization spectra. Indeed, with a classical model for driven two-electron atoms [36], the predecessor of the model of NSMI discussed here, it was shown that backscattering of the recolliding electron from the core gives rise to the finger-like structure in the two electron correlated momenta of driven He [16, 37, 38]. Double ionization spectra were obtained in very good agreement with an *ab initio* quantum mechanical calculation for driven He [39] and with an experiment for Ar driven by near-single cycle laser pulses [40]. The striking slingshot-NSDI mechanism has been identified where the exact treatment of the electron-core interaction is of paramount importance [41].

Finally, we interpret the features of the z-component of the sum of the final electron momenta in terms of the main recollision pathways for driven Ne and Ar. The differences in the ionization spectra of the two atoms are found to be due to direct pathways prevailing triple ionization of Ne.

4.2 Model

We employ the ECBB model, see Sec. 3.2.2, and the H model, Sec. 3.2.3, as described in the previous chapter to describe strongly driven Ne and Ar. However, we use a more sophisticated ionization rate [3] than the one employed in our studies of strongly driven Ar [2].

4.2.1 Empirical correction to ionization rates

The ADK rate overestimates the probability of ionization for larger intensities in Ar and Ne. To correct this we employ the empirical modification to the ADK formula proposed by Tong and Lin [116], see Fig. 4.1,

$$W_{TL}(E) = \exp\left[-\beta\left(Z_c^2/I_p\right)\left(E/\kappa^3\right)\right] W_{ADK}(E) \tag{4.1}$$

where β is a fitted coefficient. These rates are the probability per unit time that a single active electron will ionize from a specified atom and are fitted to the results obtained using the TDSE in order to obtain β.

Atom/Ion	I_p (a.u.)	Z_c	C_l	β
Ar	0.579	1	2.44	9
Ar^+	1.015	2	2.44	8
Ne	0.792	1	2.10	9
Ne^+	1.505	2	2.10	8

Table 4.1: Parameters used in the C.D. Lin empirical formula for ADK ionization rates [108, 116].

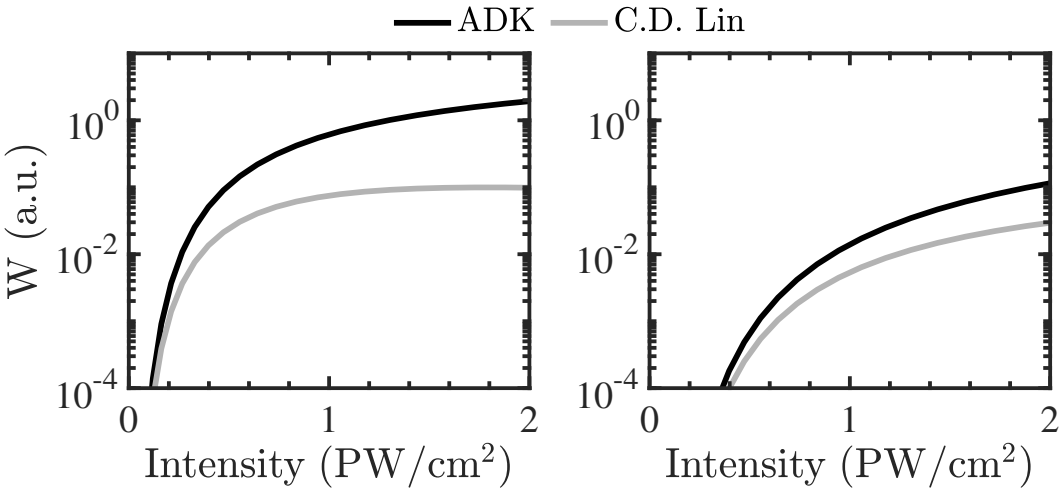

Figure 4.1: We plot the ionization rates for Ar (left) and Ne (right) using the ADK rate and the empirical formula by C.D. Lin

4.2.2 Accounting for depletion of the initial state

A simple model for the description of single and sequential double ionization is given by the rate equations

$$\begin{aligned}
\frac{dN_0(t)}{dt} &= -w_{01}(t)N_0(t) \\
\frac{dN_1(t)}{dt} &= w_{01}(t)N_0(t) - w_{12}N_1(t) \\
\frac{dN_2(t)}{dt} &= w_{12}(t)N_1(t) \\
N_1(t_0) = N_2(t_0) &= 0, \quad N_0(t_0) = 1,
\end{aligned} \tag{4.2}$$

where $N_0(t), N_1(t)$ and $N_2(t)$ are the time dependent populations of Ne, Ne^+ and Ne^{2+} respectively. The modified Ammosov-Delone-Krainov (ADK) rate [76, 107] developed by Tong and Lin [116] describes the transition from ion state i to ion state i+1 with i=0,1 as follows

$$w_{i\,i+1}(t) = w_{ADK}(t) \exp\left[-\beta \frac{Z_c^2 E(t)}{I_p (2I_p)^{3/2}}\right], \tag{4.3}$$

where Z_c is the asymptotic charge the tunneling electron sees when it tunnels from state i, I_p is the ionization potential. For each transition i to i+1 we use the values for the parameters Z_c, I_p, β as listed in Refs. [108, 116] and Tab. 4.1.

Integrating the rate equation for the ground state, we obtain the probability to be in the ground state of Ne as a function of time, i.e the population of this state,

$$N_0(t) = \exp\left[-\int_{t_0}^{t} w_{01}(t')dt'\right], \tag{4.4}$$

where we use the initial condition $N_0(t_0) = 1$. Solving numerically the other two equations, we obtain the probability for sequential double ionization, N_2, at asymptotically large times. That is, we obtain the probability for each of the two electrons to tunnel ionize due to the lowering of the Coulomb barrier by the laser field. For the laser pulse parameters considered in the current work, at intensity $1.6\,\mathrm{PW/cm^2}$ for driven Ne and at $0.4\,\mathrm{PW/cm^2}$ for driven Ar, we find that N_2 is very small compared to the probability for double ionization we obtain with full scale calculations using the ECBB model [2]. In addition, we find that N_2 is very small compared to N_1. This justifies our choice for only one electron tunneling in the initial state.

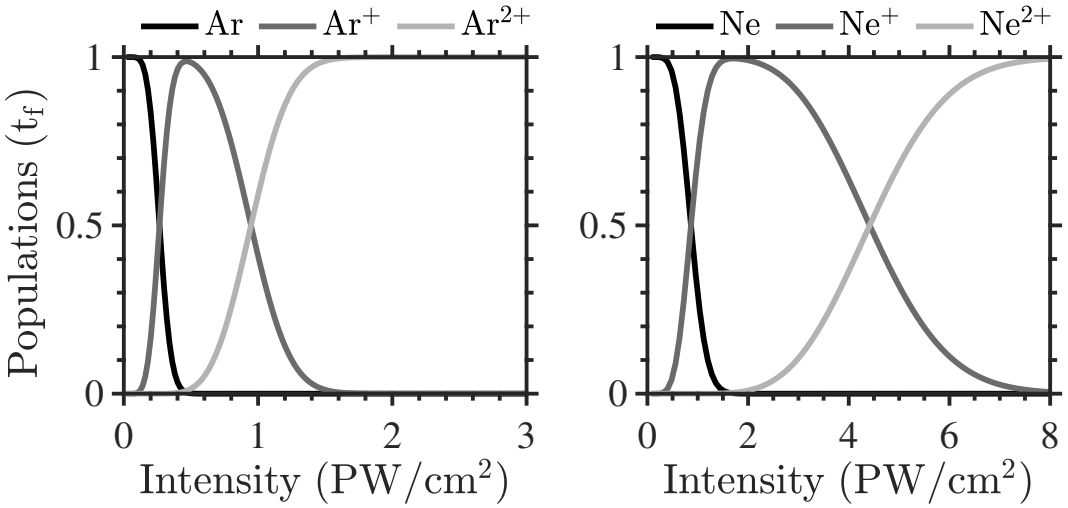

Figure 4.2: We plot the population probabilities N_0 (black line), N_1 (dark grey line), N_2 (light grey line) for a 25 fs pulse as a function of peak intensity for Ar (left) and Ne (right) using the empirical formula by C.D. Lin.

Accounting for the depletion of the initial state, the rate for tunneling from the ground state is obtained as the product of the $w_{01}(t)$ rate times the probability to be in the ground state, that is,

$$w_{01}(t)\exp\left[-\int_{t_0}^{t} w_{01}(t')dt'\right]. \tag{4.5}$$

This is the rate we use in this chapter as the probability distribution in the importance sampling we employ in our full scale calculations with the ECBB model. We account for depletion of the initial ground state for driven Ne and Ar due to the high intensities considered here and the relatively small ionization potentials I_p of Ne and Ar.

4.3 Results of strongly driven Ne

Here, we compare the results obtained with the ECBB model both with experiment and with the H model [3]. This potential depends on a parameter α, with a large value restricting more the phase space an electron can access around the core, see Sec. 3.2.3. Hence, the H model results in an effective softening of the electron-core potential. We do not compare with classical models that explicitly soften the Coulomb potential. The reason is that a previous study of NSDI in Ar [99] has shown that the H model and the model that includes the Coulomb singularity [36, 39, 40] better agree with experiment. We employ the same vector potential as in the previous chapter, with a pulse duration of $\tau = 25$ fs, while the wavelength is 800 nm. For Ne, we consider intensities 1.0, 1.3 and 1.6 PW/cm^2. For Ar, previously covered in Sec. 3.3, we consider only 0.4 PW/cm^2. The highest intensities considered here, 1.6 PW/cm^2 for Ne and 0.4 PW/cm^2 for Ar, are chosen such that the probability for a second electron to tunnel ionize solely due to the laser field is very small, see Fig. 4.2. Hence, electron-electron correlation prevails in TI and DI, with the bound electrons ionizing only due to recollisions. The smaller intensity for Ar is consistent with its smaller first ionization potential.

4.3.1 Ratio of triple and double ionization probabilities

In Fig. 4.3, for driven Ne, we compute the ratio of double to triple ionization probability and compare with experiment [28] and the H model. For all three intensities, we find the probability ratio, P_{DI}/P_{TI}, obtained with the ECBB model (black circles) to be consistently close to experiment (grey squares). In contrast, the H model

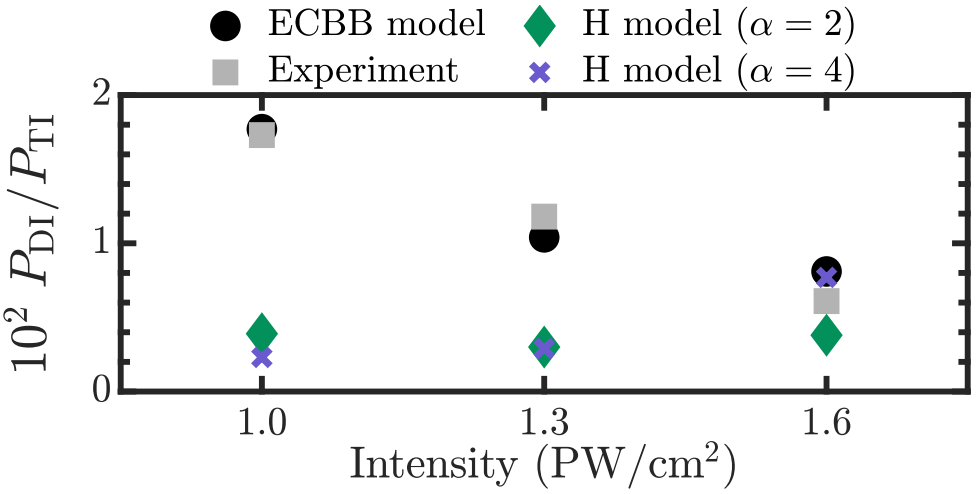

Figure 4.3: For Ne, ratio of DI to TI probability obtained with the ECBB model (black circles), the H model and experiment (grey squares) [28].

for $\alpha = 2$ and $\alpha = 4$ does not agree with experiment for 1.0 and 1.3 PW/cm^2. Also, we find that the DI probability depends on the value of α for driven Ne, see Fig. 4.2, similar to our previous findings for driven Ar in Sec. 3.3.

Double ionization probability H model (%)		
Intensity (PW/cm^2)	$\alpha = 2$	$\alpha = 4$
1.0	0.7	0.4
1.3	0.8	0.6
1.6	1.5	2.3

Table 4.2: Probabilities for double ionization obtained using the H model for Ne interacting with a laser pulse at 800 nm and 25 fs duration for $\alpha = 2$ and $\alpha = 4$.

4.3.2 Distribution of the sum of the electron momenta

Next, we compute the TI probability distribution of the z-component of the sum of the final electron momenta, sum of p_z, see black lines in Fig. 4.4. We compare with measurements (grey lines) [28], smoothed in Fig. 4.4, and with the H model for $\alpha = 2$ (green lines). We find the ECBB distributions to be doubly peaked at all intensities. With increasing intensity, the peaks become less pronounced with an increasing probability for the sum of p_z to be around zero. These features agree well with experiment. Also, the ECBB distributions peak at roughly the same values of the sum of the electron momenta as the experiment. This excellent agreement

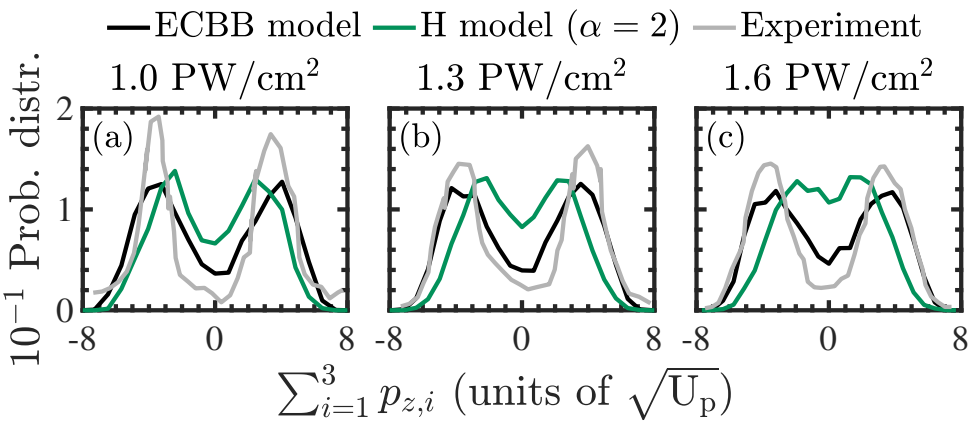

Figure 4.4: For Ne, TI probability distributions of the sum of p_z obtained with the ECBB model (black lines), with the H model (green lines) and measured experimentally [28] (grey lines). Distributions are normalized to one. U_p is the ponderomotive energy equal to $E_0^2/4\omega^2$.

further illustrates the accuracy of the ECBB model. In contrast, the H model distributions have a significantly higher probability for the sum of the final electron momenta to be around zero. Also, they are less wide compared to the ECBB model and experimental distributions. The difference is more pronounced at 1.6 PW/cm^2, [Fig. 4.4 (c)] with the H model distribution peaking around zero and the other two distributions being doubly peaked. This difference shows that in the H model the effective softening of the interaction of the recolliding electron with the core results in electrons escaping with lower energy. This gives rise to less wide distributions that have significant probability for the sum of p_z to be around zero.

4.3.3 Pathways of electron-electron recollisions

Next, using the ECBB model, we analyze the TI events and identify the recollision pathways that prevail in the three-electron escape of driven Ne. In the previous chapter, in Sec. 3.2.6.1, we outline the algorithm we use to identify the recollision pathways. An electron is deemed as ionizing soon after recollision if the difference between the recollision time and the ionization time is less than $t_{diff} = T/8$, where T is the period of the laser pulse. During this time interval, the interpotential energy between the recolliding and a bound electron undergoes a sharp change. The recollision time is identified from the maxima in the interpotential energies between the recolliding and each of the bound electrons, see Sec. 3.2.6.1.

The ionization time of electron i is defined as the time when the compensated energy $\{[\mathbf{p}_i - \mathbf{A}(y,t)]^2 + V(r_i)\}$ of this electron becomes positive and remains positive thereafter [87].

For driven Ne, we find that two are the main recollision pathways contributing to triple ionization, the direct $(e^-, 3e^-)$ and the delayed $(e^-, 2e^-)$. For a recollision to take place, an electron tunnels out through the field-lowered Coulomb barrier [12]. This electron can then return to the parent ion to recollide and transfer energy to the remaining electrons. In the direct pathway, all three electrons ionize soon after recollision, i.e. there are three highly correlated electron pairs. In the delayed $(e^-, 2e^-)$ pathway, the recolliding electron transfers enough energy for only two electrons to ionize soon after recollision, while the other electron ionizes with a delay. Hence, there is only one highly correlated electron pair. At all three intensities, we find that recollisions occur around a zero of the electric field and a maximum of the vector potential, resulting in a large final electron momentum with magnitude $E_0/\omega = 2\sqrt{U_p}$. In the direct pathway, all three electrons escape with large momenta p_z versus two electrons in the delayed $(e^-, 2e^-)$ pathway.

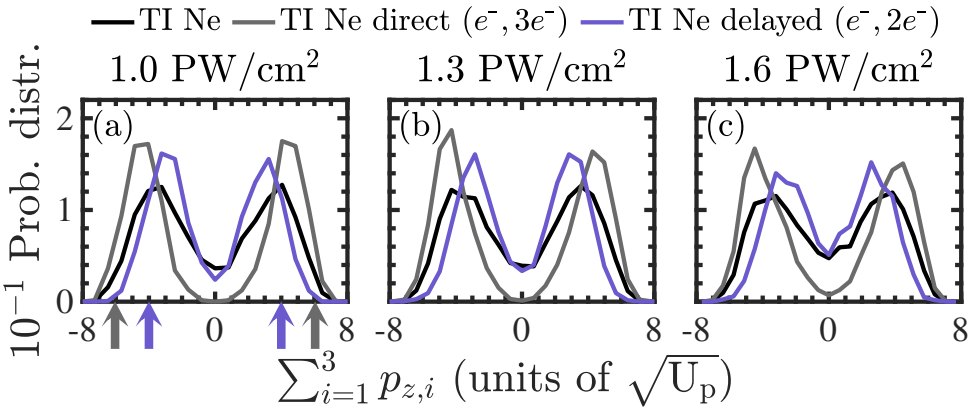

Figure 4.5: For Ne, probability distributions of the sum of p_z for TI obtained with the ECBB model for all (black), direct (dark grey) and delayed (blue) events.

Next, we explain the features of the distribution of the sum of p_z for all TI events, both the experimental and the ECBB model ones (Fig. 4.4), in terms of the direct and delayed $(e^-, 2e^-)$ pathways. In Fig. 4.5, for all three intensities, we show that the distribution of the sum of p_z extends up to roughly $\pm 3 \times 2\sqrt{U_p}$ for the direct

pathway (grey arrows in Fig. 4.5(a)) and up to $\pm 2 \times 2\sqrt{U_p}$ for the delayed $(e^-, 2e^-)$ pathway (blue arrows in Fig. 4.5(a)). This is due to three electrons in the direct and two electrons in the delayed pathway escaping with large momentum $2\sqrt{U_p}$. This is consistent with the distribution of the sum of p_z for all TI events extending up to $\pm\beta \times 2\sqrt{U_p}$, with $2 < \beta < 3$. Also, for both pathways, the distributions are doubly peaked giving rise to the double peaks of the distribution of the sum of p_z for all TI events. Moreover, in the direct pathway the distribution is roughly zero around the sum of p_z being zero. In contrast, in the delayed pathway, with increasing intensity, the peaks become less pronounced with an increasing probability for the sum of p_z to be around zero. Hence, this feature observed in the distribution of the sum of p_z for all TI events (Fig. 4.4) is due to the delayed pathway. For the H model, we find the direct to be a minor pathway, while the delayed $(e^-, 2e^-)$ one contributes the most to TI. This is consistent with soft potentials not accurately describing scattering of a recolliding electron from the core [34].

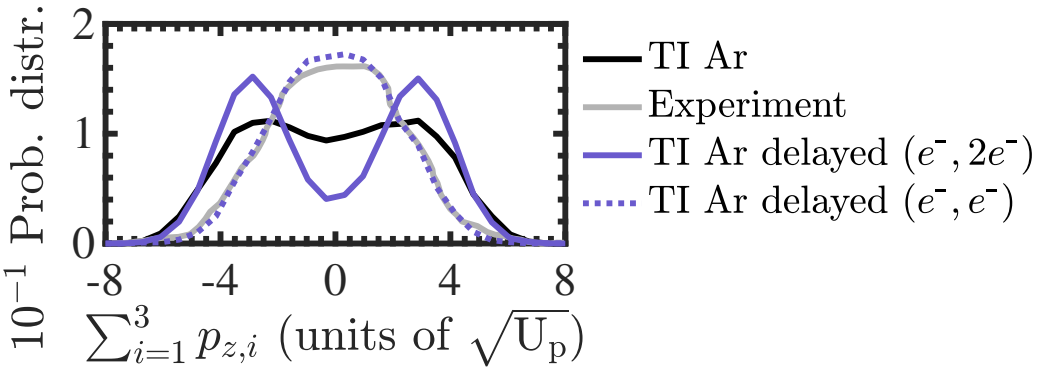

Figure 4.6: For Ar, probability distributions of the sum of p_z for TI obtained experimentally [31] (grey) and with the ECBB model for all (black) and delayed $(e^-, 2e^-)$ (blue) and delayed (e^-, e^-) events (blue dotted).

Finally, for Ar, we find that the delayed $(e^-, 2e^-)$ and (e^-, e^-) pathways prevail at $0.4\,\mathrm{PW/cm^2}$. In the latter pathway, the recolliding electron has enough energy to ionize only one electron soon after recollision. In the (e^-, e^-) pathway electrons escape with very small momenta. The contribution of these pathways to the distribution of the sum of p_z for all TI events is shown in Fig. 4.6. As for TI of Ne, for Ar, the distribution of the sum of p_z corresponding to the $(e^-, 2e^-)$ pathway is doubly

peaked with a non zero value around the sum of p_z being zero (blue line in Fig. 4.6). The distribution corresponding to the (e^-, e^-) pathway (blue dotted line in Fig. 4.6) peaks around the sum of p_z being zero. Interestingly, this distribution of the delayed (e^-, e^-) pathway is in very good agreement with the experimental distribution (grey line) at 0.3 PW/cm^2, with no measurements available at 0.4 PW/cm^2. The ECBB model distribution is more wide compared to the experimental one but also has a significant value around the sum of p_z being zero. Hence, for Ar, the ECBB model overestimates the contribution of the more correlated $(e^-, 2e^-)$ versus the less correlated (e^-, e^-) delayed pathway. Given the above, it is clear that three-electron escape is significantly less correlated in Ar than Ne. This can also be seen from the correlated momenta in Ne (Fig. 4.7) and Ar (Fig. 4.8) .

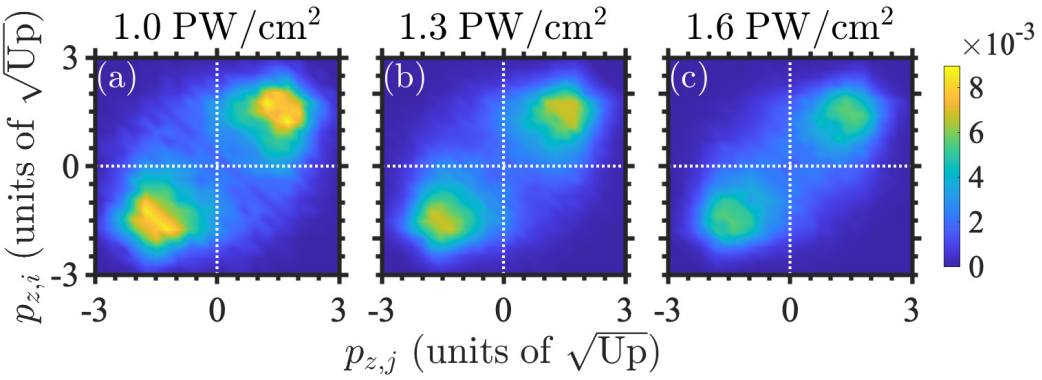

Figure 4.7: Correlated momenta of all three pairs of escaping electrons for triple ionization of driven Ne for the three intensities under consideration.

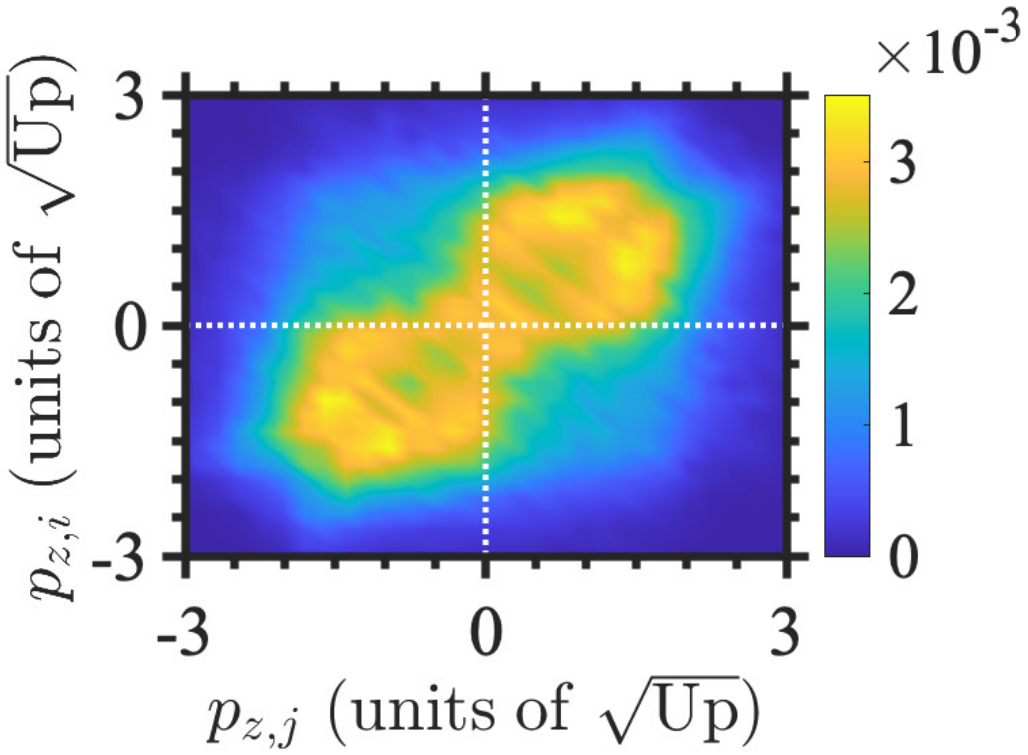

Figure 4.8: Correlated momenta of all three pairs of escaping electrons for triple ionization of driven Ar.

4.4 Conclusions

In conclusion, we demonstrate that the ECBB 3D semiclassical model is a powerful tool to study correlated multi-electron escape in driven atoms. To do so, we study three-electron ionization in Ne driven by infrared pulses. We show that the triple ionization probability distribution of the sum of the final electron momenta obtained with the ECBB model is in very good agreement with experiments. This agreement supports the premise of the ECBB model. That is, to obtain accurate multi-electron ionization spectra it is important during a recollision to accurately account for the interaction between the recolliding and the bound electron and for the interactions of the bound and recolliding electron with the core. The ECBB model is developed in a general framework and can thus be easily extended to address correlated escape of more than three electrons in driven atoms. It can also be extended to address driven molecules. We expect the ECBB model will be employed to study problems currently out of reach, leading to identifying novel ultrafast phenomena and to

motivating additional experiments in strong field science.

Chapter 5

Nondipole electron momentum offset as a probe of correlated three electron ionization in strongly driven atoms

In this chapter, we employ the ECBB three-dimensional semiclassical model to identify nondipole effects in triple ionization of Ne driven by infrared laser pulses at intensities where electron-electron correlation prevails [4]. This model fully accounts for the Coulomb interaction of each electron with the core and avoids artificial autoionization by employing effective Coulomb potentials to describe the interaction between bound electrons (ECBB). Using the ECBB model, we identify a prominent signature of nondipole effects. Namely, the component along the direction of light propagation of the average sum of the final electron momenta is large and positive. That is, we identify a positive momentum offset, absent in the dipole approximation. We find that this positive momentum offset stems mostly from the momentum change due to the magnetic field. To better understand this momentum change, we also develop a simple model for the motion of an electron inside an electromagnetic field. This simple model accounts for the effect of the Coulomb forces only as a sharp change in the momentum of the electron during recollision. We show that the momentum change due to the magnetic field is related with the

sharp change in momentum during recollision for the recolliding electron as well as with the time of recollision for both the recolliding and bound electrons. Hence, we demonstrate that the final electron momentum offset probes the strength of a recollision and hence the degree of correlation in multielectron ionization.

5.1 Introduction

The theoretical study of multielectron ionization of strongly driven systems constitutes a big computational challenge. Accounting also for the spatial dependence of the vector potential $\mathbf{A}(\mathbf{r},t)$ and consequently for the magnetic field, $\mathbf{B}(\mathbf{r},t) = \nabla \times \mathbf{A}(\mathbf{r},t)$, adds to the computational difficulty. Hence, most theoretical studies are formulated in the dipole approximation. However, to fully explore ionization phenomena and identify nondipole effects in driven atoms and molecules one needs to account for the Lorentz force $\mathbf{F_B} = q\mathbf{v} \times \mathbf{B}$ exerted on particles of charge q moving with velocity $\mathbf{v}$.

Magnetic field effects have been previously identified in a wide range of processes. For example, in stabilization [42], in high-harmonic generation [43–45], and in multielectron ionization probabilities of Ne [46], with observable effects found only for intensities two orders of magnitude larger than the ones considered in the current work. For the largest intensity we consider here, we find that the amplitude $\beta_0 \approx U_p/(2\omega c)$ of the electron motion due to $\mathbf{F_B}$ is roughly 0.2 a.u., where U_p is the ponderomotive energy. This is much smaller than $\beta_0 \approx 1$ a.u. where according to Refs. [47, 48] magnetic field effects are expected to arise. Over the last years, there has been an intense interest in nondipole effects [49, 50, 117–127]. Advanced studies [49, 50] have predicted nondipole effects in correlated two-electron ionization, which have been verified experimentally for driven Ar [122]. Nondipole effects in nonsequential double ionization were also studied in a recent experiment on strongly driven Xe [124].

nondipole gated double ionization was previously reported as a prominent mechanism of nondipole effects in nonsequential double ionization of strongly driven atoms [49, 50]. The magnetic field jointly with a recollision act as a gate

that allows for double ionization to occur only for a subset of the initial momenta of the recolliding electron along the direction of light propagation. Namely, the recolliding electron has an average initial momentum that is negative along the direction of light propagation (y axis in this chapter), while it is zero in the dipole approximation. The electric field is linearly polarized along the z axis. This negative initial momentum compensates for the positive momentum shift induced by the Lorentz force, allowing for the recolliding electron to return to the core. As a result, the recolliding electron just before recollision arrives from the -y axis with positive momentum. For the case of strongly driven He at high intensities, it was shown that the recollisions involved are glancing ones. As a result, the recolliding electron just before recollision is accelerated by the Coulomb attraction from the core resulting in the y component of the average sum of the final electron momenta being large and positive [49, 50].

For triple ionization of Ne, for intensities where strong and not glancing recollisions prevail, we find that nondipole gated ionization is still present, i.e., the recolliding electron has a negative average initial momentum. We demonstrate that the strong recollisions involved for driven Ne result in a different physical mechanism, compared to driven He, still giving rise to a large positive y component of the average sum of the final electron momenta.

For driven Ne, using the ECBB model, we identify the change in momentum due to the magnetic field as the main source for the positive momentum offset along the y axis. To better understand this momentum change, we also develop a simple model to describe the motion of an electron inside an electromagnetic field. In this simple model, we take into account the effect of the Coulomb forces via a sharp change in the momentum of each electron during recollision. Using this model, we show that for the recolliding electron the value of the positive momentum offset is analogous to the momentum change along the z axis during recollision. That is, a strong recollision results in a large positive offset. Also, for both a bound and a recolliding electron, we find that the value of the momentum offset depends on the time of recollision. Namely, a strong recollision that takes place around a zero of

the electric field results in a large positive momentum offset.

Hence, in this work we demonstrate that in multielectron ionization the positive momentum offset probes the strength of the recollision involved and hence the degree of correlated electron-electron dynamics. We do so by finding a larger positive momentum offset for triple compared to double ionization and for the direct compared to the delayed recollision pathway of driven Ne. Indeed, we show that triple is more correlated than double ionization and that electron-electron correlation is stronger in the direct compared to the delayed pathway.

5.2 Model

In what follows we employ the ECBB model as in Sec. 4.2 with one minor alteration. In the ECBB model, all electrons and the core are allowed to move [2, 3]. However, it has not yet been fully investigated how the I_p/c momentum due to non-dipole effects during tunneling is split between the core and the tunneling electron as a function of laser intensity. That is, it has not yet been established what we should consider as the momentum of the core in our computations along the y axis in the initial state following tunneling. Hence, we consider the mass of the core to be infinite and effectively fix the core in the computations that follow [4]. We hope that our work will motivate future work that will establish how the momentum I_p/c should be split between the tunneling electron and the core due to tunneling.

5.3 Results for strongly driven Ne

5.3.1 Correlated electron momenta in triple and double ionization

In what follows, we have taken the pulse duration to be $\tau = 25$ fs, while the wavelength is 800 nm [4]. We consider intensities of 1.0, 1.3 and 1.6 $\mathrm{PW/cm^2}$. The highest intensity considered is chosen such that the probability for a second electron to tunnel ionize in Ne solely due to the laser field is very small [3]. In Fig. 5.1, for TI and DI of driven Ne, we plot the symmetrised correlated electron momenta along the direction of the electric field (p_z) for all pairs of escaping electrons. That

is, we plot the correlated momenta for each pair of electrons, irrelevant of the momentum of the third electron, and then superimpose the correlated momenta of all three pairs. We find the ratio of triple to double ionization to be equal to 186, 106 and 81 for 1.0, 1.3 and 1.6 PW/cm^2 [3]. We find that electron-electron dynamics is more correlated in triple compared to double ionization. Specifically, for TI, at all three intensities, we find (not shown) that recollisions occur around a zero of the electric field and hence at an extremum of the vector potential. This results in large final electron momenta in TI, since p_z is roughly equal to minus the vector potential at the time of recollision. Indeed, this is seen in Figs. 5.1(a)-5.1(c), where we have a large concentration of electrons with large momenta in the first and third quadrants. Comparing Figs. 5.1(a)-5.1(c) for TI with Figs. 5.1(d)-5.1(f) for DI, we find that electron-electron dynamics is more correlated for TI. This is particularly the case at

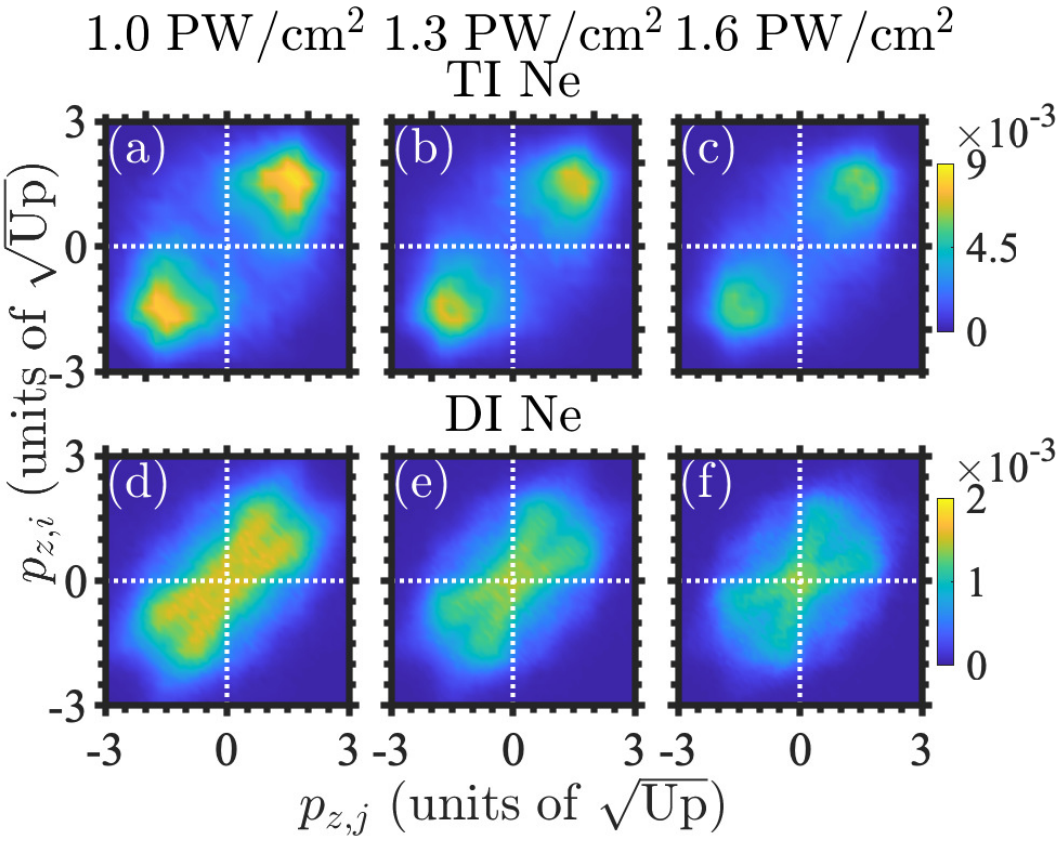

Figure 5.1: For Ne, symmetrized correlated momenta p_z of all three pairs of escaping electrons for triple ionization (top row) and the one pair of escaping electrons for double ionization (bottom row). Each plot is normalized to one.

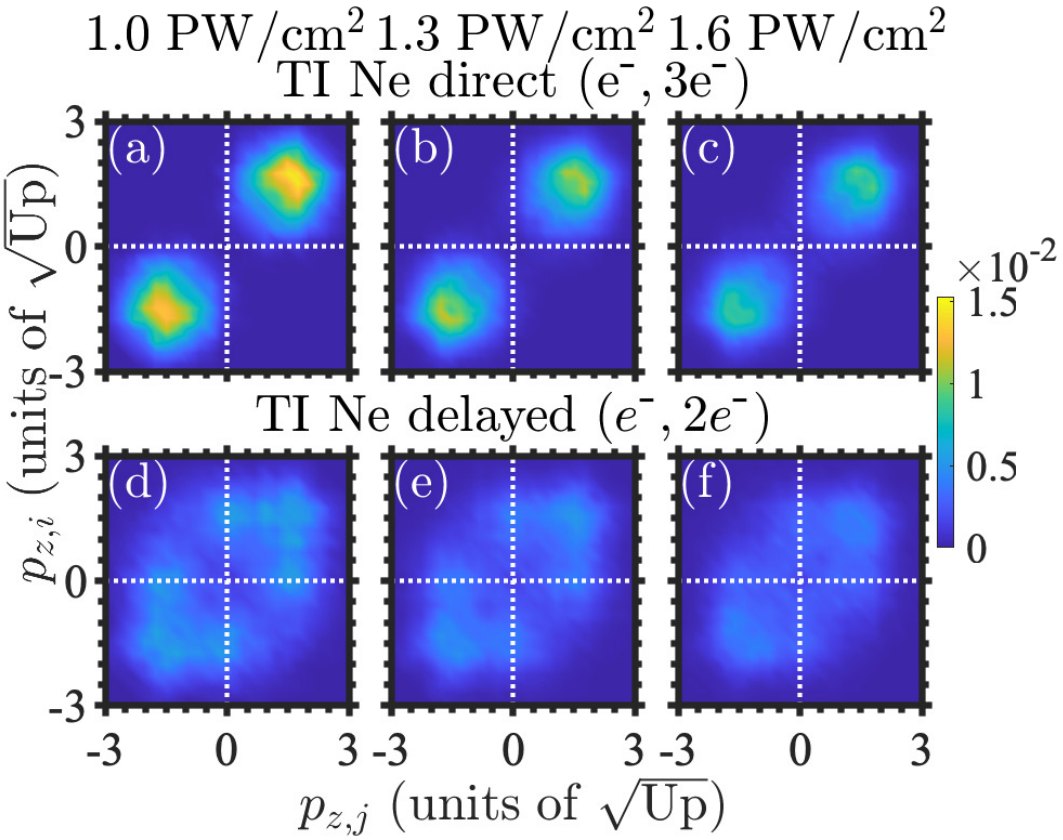

Figure 5.2: For triple ionization of Ne, symmetrized correlated momenta p_z for the direct $(e^-, 3e^-)$ pathway (top row) and for the delayed $(e^-, 2e^-)$ pathway (bottom row). Each plot is normalized to one.

the higher intensity, 1.6 PW/cm^2, where we find that for DI recollisions occur more around an extremum of the field, i.e., a zero of the vector potential. This results in smaller final electron momenta for DI.

Next, for TI and DI, we show that electron-electron dynamics is more correlated for recollision pathways where more electrons ionize soon after recollision. For TI, we find that the prevailing recollision pathways are the direct $(e^-, 3e^-)$ and the delayed $(e^-, 2e^-)$. The notation (e^-, ne^-) denotes n electrons ionizing shortly after recollision. Also, DI proceeds mainly via the direct $(e^-, 2e^-)$ and the delayed (e^-, e^-) pathways. We plot the symmetrized correlated electron momenta p_z for the prevailing recollision pathways for TI in Fig. 5.2 and for DI in Fig. 5.3. In Fig. 5.2, we clearly show that electron-electron correlation is higher in the direct pathway [Figs. 5.2(a)-5.2(c)] compared to the delayed pathway [Figs. 5.2(d)-5.2(f)]. Indeed, in Fig. 5.2, for TI, for the direct pathway the majority of events are concentrated in the

first and third quadrants while for the delayed pathway the events are more spread out. For DI, Fig. 5.3 clearly shows that electron-electron correlation is higher in the direct compared to the delayed pathway at all three intensities. Indeed, for DI, events for the direct pathway are concentrated in the first and third quadrants while for the delayed pathway events are concentrated around zero momentum. Also, we find that electron-electron correlation is higher for the direct (delayed) pathway of TI compared to the direct (delayed) pathway of DI.

5.3.2 Positive momentum offset along the propagation direction in triple ionization

In Fig. 5.4, for TI of driven Ne, to obtain the momentum offset per pair of ionizing electrons, we compute the y component (direction of light propagation) of the average sum of the final electron momenta and we then multiply by a factor of 2/3 as

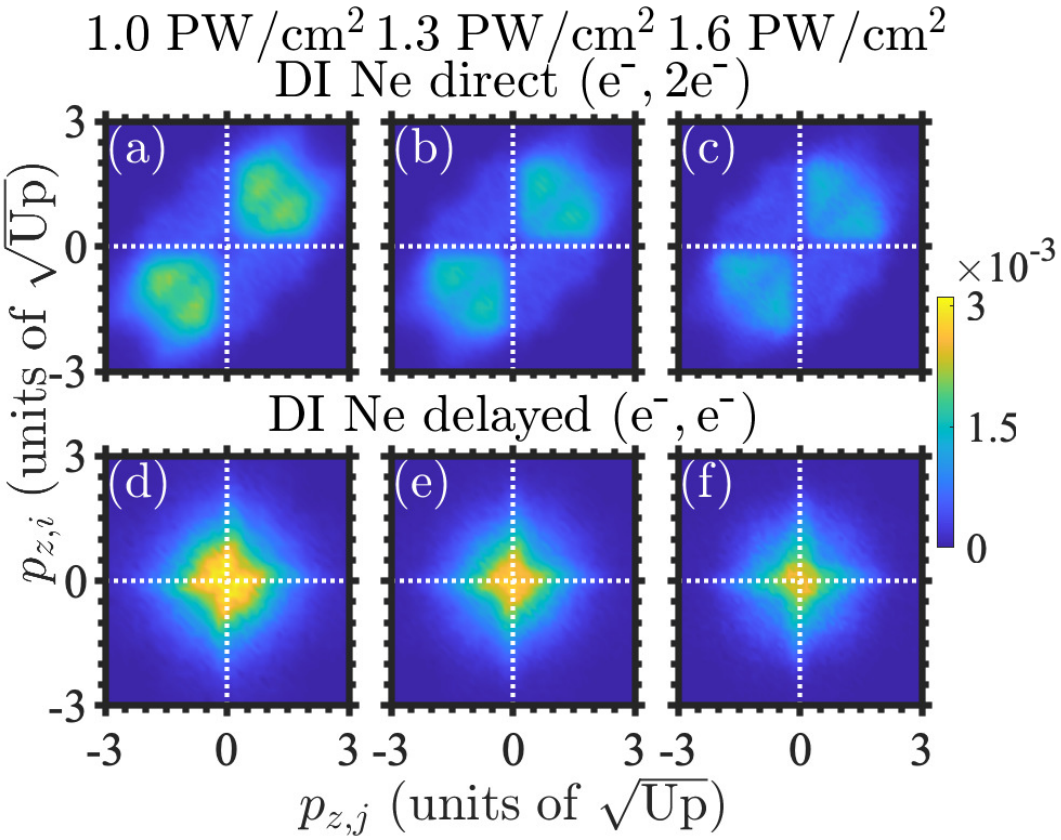

Figure 5.3: For double ionization of Ne, symmetrized correlated momenta for the direct $(e^-, 2e^-)$ pathway (top row) and for the delayed (e^-, e^-) pathway (bottom row). Each plot is normalized to one.

follows

$$\frac{2}{3}\left\langle \sum_{i=1}^{3} p_{y,i} \right\rangle_{TI} = \left\langle \frac{(p_{y,1}+p_{y,2})+(p_{y,1}+p_{y,3})+(p_{y,2}+p_{y,3})}{3} \right\rangle. \tag{5.1}$$

We denote by $p_{y,i}$ the y component of the final momentum of electron i. The reason we compute for TI the momentum offset per pair of electrons is to directly compare with the momentum offset for DI where there is only one pair of ionizing electrons. Note that the momentum offset for both TI and DI is zero in the dipole approximation. For TI, the momentum offset is denoted by the height of the red bars in

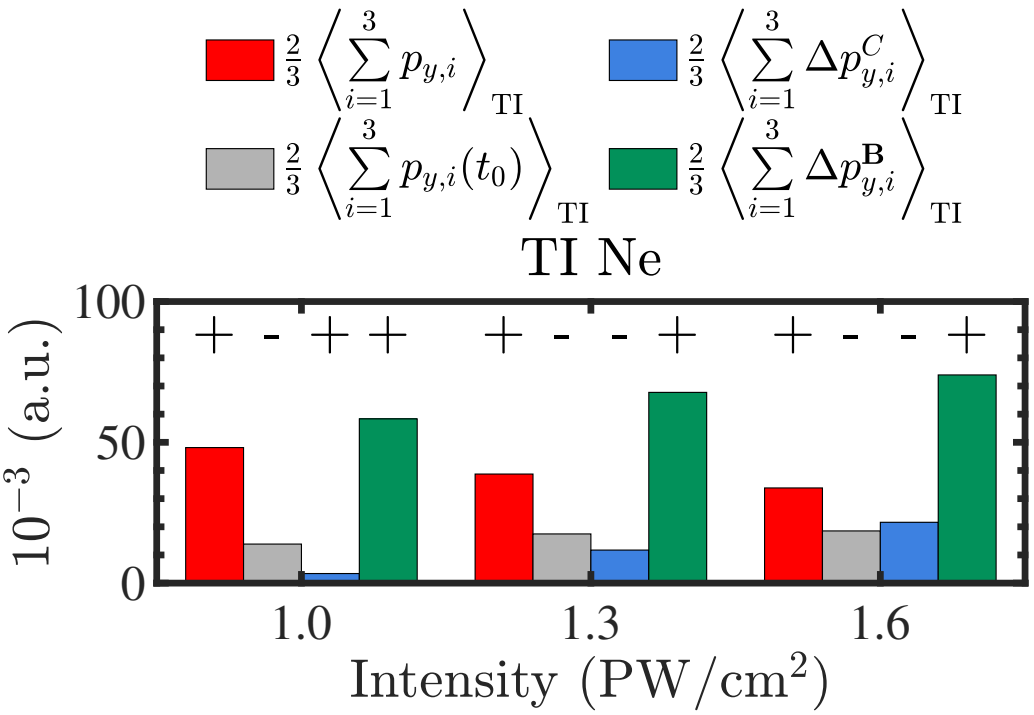

Figure 5.4: For Ne, at each intensity, height of red bar denotes the momentum offset per pair of electrons for TI $2/3\left\langle \sum_{i=1}^{3} p_{y,i} \right\rangle$, and the contributions due to the initial momentum $2/3\left\langle \sum_{i=1}^{3} p_{y,i}(t_0) \right\rangle$ (gray bar), the magnetic field $2/3\left\langle \sum_{i=1}^{3} \Delta p^{\mathbf{B}}_{y,i} \right\rangle$ (green bar) and due to the Coulomb and effective potential forces $2/3\left\langle \sum_{i=1}^{3} \Delta p^{C}_{y,i} \right\rangle$ (blue bar). The plus (+), minus (-) sign above the bar denotes a positive or negative value, respectively, for the given contribution.

Fig. 5.4. At all three intensities, we find that the momentum offset has a significant positive value around 0.035 a.u. We find that this is roughly four times larger than twice (to account for an electron pair) the momentum offset in single ionization.

Next, we identify the reason for the positive value of the momentum offset. To do so, we write the average value of the final electron momentum, $\langle p_{y,i} \rangle$, in terms of three contributions as follows

$$\langle p_{y,i} \rangle = \langle p_{y,i}(t_0) \rangle + \left\langle \Delta p^{C}_{y,i} \right\rangle + \left\langle \Delta p^{\mathbf{B}}_{y,i} \right\rangle . \tag{5.2}$$

The first term, $\langle p_{y,i}(t_0) \rangle$, is the y component of the average value of the initial electron momentum. The next term, $\left\langle \Delta p^{C}_{y,i} \right\rangle$, denotes the y component of the average change in the momentum of electron i in the time interval $[t_0, t_f]$ due to the Coulomb forces and the effective potentials while the term, $\left\langle \Delta p^{\mathbf{B}}_{y,i} \right\rangle$, denotes the corresponding momentum change due to the magnetic field. Fig. 5.4 clearly shows that the positive momentum offset per pair of electrons for TI is due to the momentum change from the magnetic field (green bars). Fig. 5.4 also shows that the momentum change due to the Coulomb and the effective potentials forces (blue bars) is significantly less compared to the momentum change due to the magnetic field. Hence, in what follows, we only focus on the momentum change due to the magnetic field.

The above show that for NSTI in driven Ne the mechanism responsible for the positive momentum offset along the y axis is different from nondipole gated ionization identified in strongly driven He [49]. In the latter case, the significant positive momentum offset in DI was due to the recolliding electron coming in just before recollision mostly from the -y direction with positive momentum p_y and the Coulomb attraction from the core acting to increase p_y. However, the recollisions involved in driven He were glancing ones. For NSTI in driven Ne, we find that the recolliding electron also has a negative average initial momentum along the y axis and also approaches mostly from the -y axis with positive p_y momentum (Fig. 5.5). However, the recollisions in driven Ne are strong ones resulting in the most important contribution to the y component of the momentum change being due to the magnetic field and not due to the Coulomb attraction from the core.

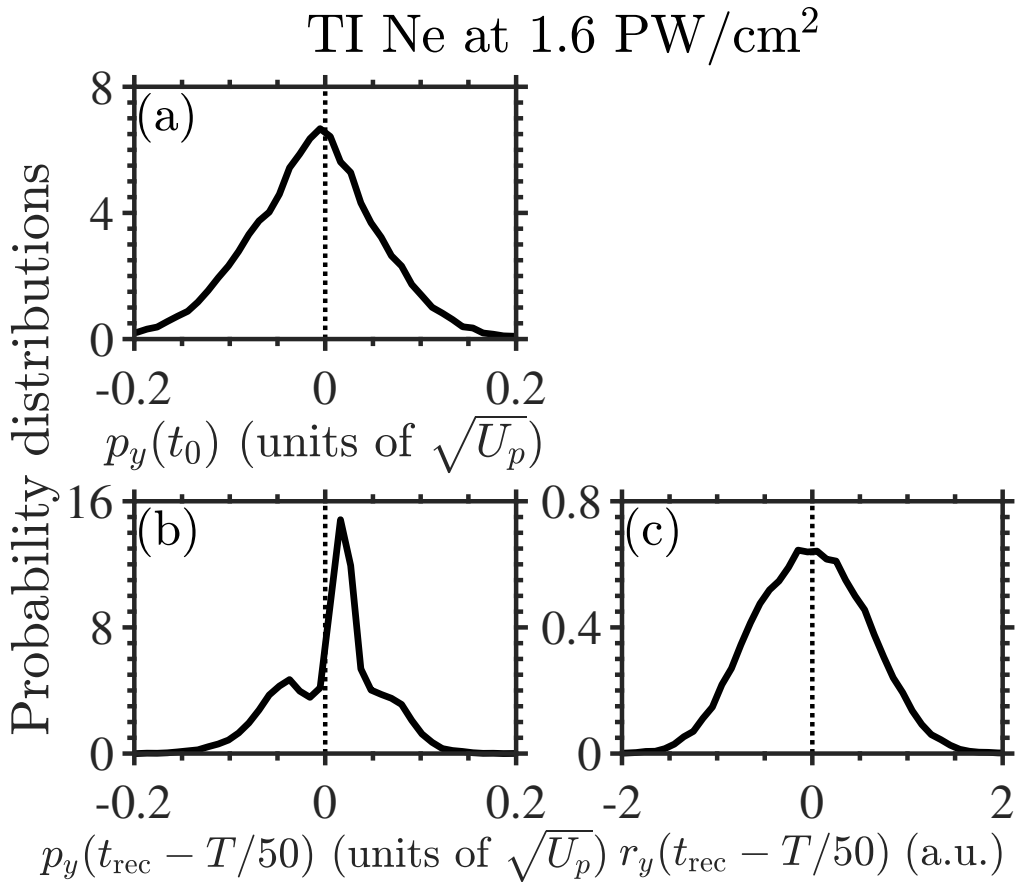

Figure 5.5: Plots of the distribution of the y component of the momentum of the recolliding electron at the time of tunneling t_0 (a), shortly before recollision at time $t_{rec} - T/50$ (b), and of the y component of the position of the recolliding electron shortly before recollision at time $t_{rec} - T/50$ (c) for TI of driven Ne at 1.6 PW/cm^2. T is the period of the laser field.

5.3.3 Momentum change along the y axis

In what follows we identify the main contributions to the term $\left\langle \Delta p^{\mathbf{B}}_{y,i} \right\rangle$ in Eq. (5.2) for the recolliding and bound electrons. We find $\Delta p^{\mathbf{B}}_{y,i}$ using a simple model of an electron inside an electromagnetic field and account for the effect of the Coulomb forces with a sharp change during recollision in the momentum of each electron.

5.3.3.1 Momentum change along the y axis for a recolliding electron

The Lorentz force acting on an electron i is

$$\mathbf{F}_L = -\left[\mathbf{E}(y_i, t) + \mathbf{p}_i \times \mathbf{B}(y_i, t)\right]. \tag{5.3}$$

The momentum of electron i at time t is then given by

$$\mathbf{p}_i(t) = \mathbf{p}_i(t_0) - \int_{t_0}^{t} \left[\mathbf{E}(y_i, t') + \mathbf{p}_i \times \mathbf{B}(y_i, t')\right] dt'. \tag{5.4}$$

Eq. (5.4) does not account for the Coulomb interaction between an electron and the core as well as between electrons. In a simplified model for the recolliding electron, we account for the momentum change due to a recollision and hence due to the Coulomb forces by adding a term in (5.4) as follows

$$\begin{aligned}\mathbf{p}_i(t) = \mathbf{p}_i(t_0) &- \int_{t_0}^{t} \left[\mathbf{E}(y_i, t') + \mathbf{p}_i \times \mathbf{B}(y_i, t')\right] dt' \\ &+ H(t - t_{rec})\Delta\mathbf{p}_i(t_{rec}),\end{aligned} \tag{5.5}$$

with $H(t - t_{rec})$ the Heaviside function [128] and with $\Delta\mathbf{p}_i(t_{rec})$ being the momentum change due to the Coulomb forces just after and before the recollision time, t_{rec}. Then from Eq. (5.5) it follows that the y component of the momentum change due to the magnetic field for $t > t_{rec}$ takes the form

$$\begin{aligned}\Delta p^{\mathbf{B}}_{y,i}(t_0 \to t) &= -\int_{t_0}^{t} p_{z,i}(t')B(y_i, t')dt' \\ &= -\int_{t_0}^{t}\left[p_{z,i}(t_0) - \int_{t_0}^{t'} E(y_i, t'')dt'' + \int_{t_0}^{t'} p_{y,i}(t'')B(y_i, t'')dt'' + H(t' - t_{rec})\Delta p_{z,i}(t_{rec})\right] B(y_i, t')dt' \\ &= -\int_{t_0}^{t}\left[p_{z,i}(t_0) - \int_{t_0}^{t'} E(y_i, t'')dt'' + \int_{t_0}^{t'} p_{y,i}(t'')B(y_i, t'')dt''\right] B(y_i, t')dt' - \Delta p_{z,i}(t_{rec})\int_{t_{rec}}^{t} B(y_i, t')dt' \\ &= \Delta p^{\mathbf{B},1}_{y,i}(t_0 \to t) - \Delta p_{z,i}(t_{rec})\int_{t_{rec}}^{t} B(y_i, t')dt' = \Delta p^{\mathbf{B},1}_{y,i}(t_0 \to t) + \Delta p^{\mathbf{B},2}_{y,i}(t_{rec} \to t)\end{aligned} \tag{5.6}$$

The term $\Delta p^{\mathbf{B},1}_{y,i}(t_0 \to t)$ simplifies when we take into account that in our model the initial momentum of the recolliding electron along the direction of the electric field is zero, $p_{z,i}(t_0) = 0$. Furthermore, for the purposes of this model we neglect terms of the order of $\mathbf{B}^2$, since the ratio of the magnitudes of the electric and magnetic field is $|E(y_i, t)/B(y_i, t)| = c$. Another approximation we make for the purposes of this model is that we compute the integral of the magnetic and electric

field over time at the position $y_i = 0$. That is,

$$E(y_i, t) \approx E(0, t) \equiv E(t) \tag{5.7}$$

$$B(y_i, t) \approx B(0, t) \equiv B(t). \tag{5.8}$$

Given the above approximations we find that

$$\Delta p_{y,i}^{\mathbf{B},1}(t_0 \to t) = \int_{t_0}^{t} \left[\int_{t_0}^{t'} E(t'')dt'' \right] B(t')dt' \tag{5.9a}$$

$$\Delta p_{y,i}^{\mathbf{B},2}(t_{rec} \to t) = -\Delta p_{z,i}(t_{rec}) \int_{t_{rec}}^{t} B(t')dt'. \tag{5.9b}$$

For the recolliding electron, at all three intensities both for TI and DI, we find that the term $\Delta p_{y,i}^{\mathbf{B},2}(t_{rec} \to t_f)$ contributes the most to $\Delta p_{y,i}^{\mathbf{B}}(t_0 \to t_f)$. To do so, we obtain $\Delta p_{z,i}(t_{rec})$ from our full calculations using the ECBB model. Next, we show that $\Delta p_{y,i}^{\mathbf{B},2}(t_{rec} \to t_f)$ is always positive. Indeed, we rewrite Eq. (5.9b) as

$$\begin{aligned} \Delta p_{y,i}^{\mathbf{B},2}(t_{rec} \to t_f) &= -\Delta p_{z,i}(t_{rec}) \int_{t_{rec}}^{t_f} \frac{E(t)}{c} dt \\ &= -\frac{1}{c} \Delta p_{z,i}(t_{rec}) \left[A(t_{rec}) - A(t_f) \right] \\ &= -\frac{1}{c} \Delta p_{z,i}(t_{rec}) A(t_{rec}), \end{aligned} \tag{5.10}$$

where we use $\mathbf{E}(t) = -\frac{\partial \mathbf{A}(t)}{\partial t}$ and $A(t_f \to \infty) = 0$. Moreover, for the tunneling/recolliding electron, we find that

$$\begin{aligned} p_{z,i}(t_{rec}) &= -\int_{t_0}^{t_{rec}} E(t)dt \\ &= -\left[A(t_0) - A(t_{rec}) \right] \\ &= A(t_{rec}), \end{aligned} \tag{5.11}$$

where we have used that $A(t_0) \approx 0$, since the electron tunnels at an initial time t_0

around an extremum of the electric field. Then Eq. (5.10) can be written as

$$\begin{aligned}\Delta p_{y,i}^{\mathbf{B},2}(t_{rec} \to t_f) &= -\frac{1}{c}\Delta p_{z,i}(t_{rec}) p_{z,i}(t_{rec}) \\ &= -\frac{1}{c}\left[p_{z,i}(t_{rec}+\Delta t) - p_{z,i}(t_{rec})\right] p_{z,i}(t_{rec}).\end{aligned} \tag{5.12}$$

During a recollision, the magnitude of the momentum of the recolliding electron after the recollision is always smaller than its magnitude before the recollision. Hence, one can easily show that $\Delta p_{y,i}^{\mathbf{B},2}(t_{rec} \to t_f)$ is always greater than zero.

5.3.3.2 Momentum change along the y axis for a bound electron

Concerning a bound electron, we assume that the electron feels the electric and magnetic field only after it is ionized, i.e. roughly at the recollision time. Hence, for the bound electron, in (5.5) and (5.6) we substitute t_0 by t_{rec}. We also assume that $p_i(t_{rec}) \approx 0$. Given the above, we find that

$$\begin{aligned}\Delta p_{y,i}^{\mathbf{B}}(t_{rec} \to t) &= \int_{t_{rec}}^{t}\left[\int_{t_{rec}}^{t'} E(t'')dt''\right] B(t')dt' \\ &\quad -\Delta p_{z,i}(t_{rec})\int_{t_{rec}}^{t} B(t')dt' \\ &= \Delta p_{y,i}^{\mathbf{B},1}(t_{rec} \to t) + \Delta p_{y,i}^{\mathbf{B},2}(t_{rec} \to t)\end{aligned} \tag{5.13}$$

For both TI and DI, at all three intensities, we find that the term $\Delta p_{y,i}^{\mathbf{B},1}(t_{rec} \to t_f)$ contributes the most to $\Delta p_{y,i}^{\mathbf{B}}(t_{rec} \to t_f)$ for the bound electron. Next, we show that

this term is always positive as follows

$$\begin{aligned}
\Delta p_{y,i}^{\mathbf{B},1}(t_{rec} \to t_f) &= \int_{t_{rec}}^{t_f} \left[\int_{t_{rec}}^{t} E(t')dt' \right] B(t)dt \\
&= \int_{t_{rec}}^{t_f} [A(t_{rec}) - A(t)]\, B(t)dt \\
&= A(t_{rec}) \int_{t_{rec}}^{t_f} B(t)dt - \int_{t_{rec}}^{t_f} A(t)B(t)dt \\
&= \frac{A(t_{rec})}{c} [A(t_{rec}) - A(t_f)] - \int_{t_{rec}}^{t_f} A(t)\frac{E(t)}{c}dt \\
&= \frac{1}{c}\left[A^2(t_{rec}) + \frac{A^2(t_f)}{2} - \frac{A^2(t_{rec})}{2} \right] \\
&= \frac{1}{2c} A^2(t_{rec}) > 0.
\end{aligned} \tag{5.14}$$

where we use $A(t_f \to \infty) = 0$.

5.3.4 Comparison of the offset between double and triple ionization

In Fig. 5.6, for DI of driven Ne, we compute the y component of the average sum of the final momenta of the ionizing electron pair, $\left\langle \sum_{i=1}^{2} p_{y,i} \right\rangle_{DI}$. This momentum offset is denoted by the height of the red bar. At intensities 1.0 and 1.3 PW/cm^2 we find that the momentum offset has a positive value around 0.03 a.u. This is roughly three times larger than twice (to account for the electron pair) the momentum offset in single ionization. At intensity 1.6 PW/cm^2 the value of the positive momentum offset is approximately half its value at the two smaller intensities. Fig. 5.6, clearly shows that the positive momentum offset for DI is due to the momentum change from the magnetic field (green bars), as was the case for TI. At all three intensities, we find that for triple ionization $2/3 \left\langle \sum_{i=1}^{3} \Delta p_{y,i}^{\mathbf{B}} \right\rangle$ ranges roughly between 0.06 to 0.07 a.u. (green bars in Fig. 5.4), while for double ionization $\left\langle \sum_{i=1}^{2} \Delta p_{y,i}^{\mathbf{B}} \right\rangle$ is smaller, ranging roughly between 0.04 to 0.05 a.u. (green bars in Fig. 5.6).

Now, we show that the smaller positive momentum offset due to the magnetic field in double ionization compared to triple ionization is consistent with the simple model developed in Section 5.3.3. Indeed, recollisions are stronger in TI versus

DI. This is evidenced by the higher degree of electron-electron correlation in TI compared to DI, compare top with bottom row in Fig. 5.1. A stronger recollision in TI translates to a larger change of the z component of the momentum of the recolliding electron due to the Coulomb forces during recollision, i.e., to a larger value of $\Delta p_{z,i}(t_{rec})$ in Eq. (5.10). Moreover, a stronger recollision also translates to the time of recollision being around a zero of the electric field, resulting to an extremum of $A(t_{rec})$. Hence, the most important contributions to the momentum offset, for the recolliding electron the term $\Delta p^{\mathbf{B},2}_{y,i}(t_{rec} \to t_f)$ [Eq. (5.10)] and for the bound electron the term $\Delta p^{\mathbf{B},1}_{y,i}(t_{rec} \to t_f)$ [Eq. (5.14)], have larger values for TI compared to DI.

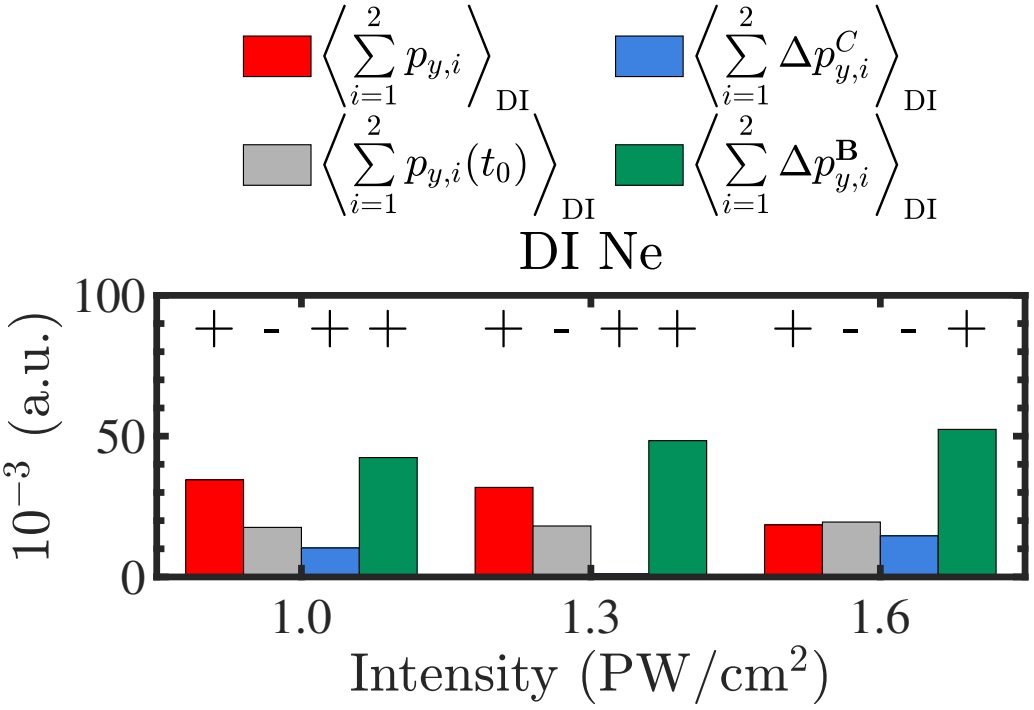

Figure 5.6: For Ne, at each intensity, height of red bar denotes the momentum offset per pair of electrons for DI $\left\langle \sum_{i=1}^{2} p_{y,i} \right\rangle$, and the contributions due to the initial momentum $\left\langle \sum_{i=1}^{2} p_{y,i}(t_0) \right\rangle$ (gray bar) to the magnetic field $\left\langle \sum_{i=1}^{2} \Delta p^{\mathbf{B}}_{y,i} \right\rangle$ (green bar) and due to the Coulomb and effective potential forces $\left\langle \sum_{i=1}^{2} \Delta p^{C}_{y,i} \right\rangle$ (blue bar). The plus (+), minus (-) sign above the bar denotes a positive or negative value, respectively, for the given contribution.

5.3.5 Electron momentum offset for direct versus delayed pathways in double and triple ionization

In what follows, we compare the momentum offset in the direct versus the delayed pathway both in TI and DI. In Fig. 5.7, for TI of driven Ne, we show the momentum offset (red bars), the contribution to this offset from the magnetic field (green bars) as well as the contribution from the Coulomb and effective potential forces (blue bars) for the direct (top row) and the delayed $(e^-, 2e^-)$ pathway (bottom row). For highest two intensities we find that the momentum offset (red bars) is larger in the direct compared to the delayed pathway. Fig. 5.7 clearly shows that this is mainly due to the larger positive values of the momentum change due to the magnetic field (green bars) in the direct compared to the delayed pathway. That is, the term $2/3\left\langle \sum_{i=1}^{3} \Delta p_{y,i}^{\mathbf{B}} \right\rangle$ is larger in the direct compared to the delayed pathway. Fig. 5.8. shows that the same holds true for DI of driven Ne for all three intensities. That is, the momentum offset as well as the contribution to this offset from the magnetic field, $\left\langle \sum_{i=1}^{2} \Delta p_{y,i}^{\mathbf{B}} \right\rangle$, is larger in the direct compared to the delayed pathway. Next, we explain why this is the case. During recollision, the recolliding electron gives more energy to the bound electrons in the direct compared to the delayed pathway. That is, the sharp momentum change of the recolliding electron during recollision, $\Delta p_{z,i}(t_{rec})$, is larger in the direct compared to the delayed pathway. Hence, $\Delta p_{y,i}^{\mathbf{B},2}(t_{rec} \to t_f)$ in Eq. (5.10) for the recolliding electron, is larger in the direct pathway. In addition, for the bound electrons, $\Delta p_{y,i}^{\mathbf{B},1}(t_{rec} \to t_f)$ in Eq. (5.14) is larger in the direct compared to the delayed pathway. The reason is that both bound electrons in the direct pathway ionize soon after the recollision time which is around an extremum of the vector potential A, i.e., maximum value of $A(t_{rec})$. However, in the delayed pathway, most likely, it is one of the bound electrons that ionizes with a delay from the recollision time and hence $A(t_{rec})$ is smaller than its extremum value.

Finally, we note that the contribution of the momentum change due to the Coulomb and effective potential forces along the y axis $\frac{2}{3}\left\langle \sum_{i=1}^{3} \Delta p_{y,i}^{C} \right\rangle$ (see Fig. 5.4) is larger for the delayed versus the direct pathway of TI. This is consistent with the

electrons spending more time around the core in the weaker recollisions that take place in the delayed compared to the direct pathway of TI. Moreover, we find that the contribution of the momentum change due to the Coulomb and effective potential forces along the y axis is larger for the delayed pathway of TI compared to the delayed pathway of DI. This is consistent with the net core charge that is seen by an escaping electron in TI being equal to three versus two in DI.

5.4 Conclusions

In conclusion, we use the ECBB 3D semiclassical model to identify nondipole effects in triple and double ionization in Ne driven by infrared pulses for intensities where recollisions, i.e., electron-electron correlation, prevail. We find a large positive average sum of the final electron momenta along the direction of light propagation. This momentum offset is zero in the absence of the magnetic field. Most importantly, we show this final electron momentum offset to be a probe of electron-electron correlation. Indeed, we find a larger momentum offset for the more correlated electron-electron ionization i) in triple compared to double ionization of driven Ne, especially at high intensities, and ii) in the direct versus the delayed pathway of triple and double ionization of Ne. The nondipole effects identified here in multielectron ionization observables can be accessed and hence verified by future experiments.

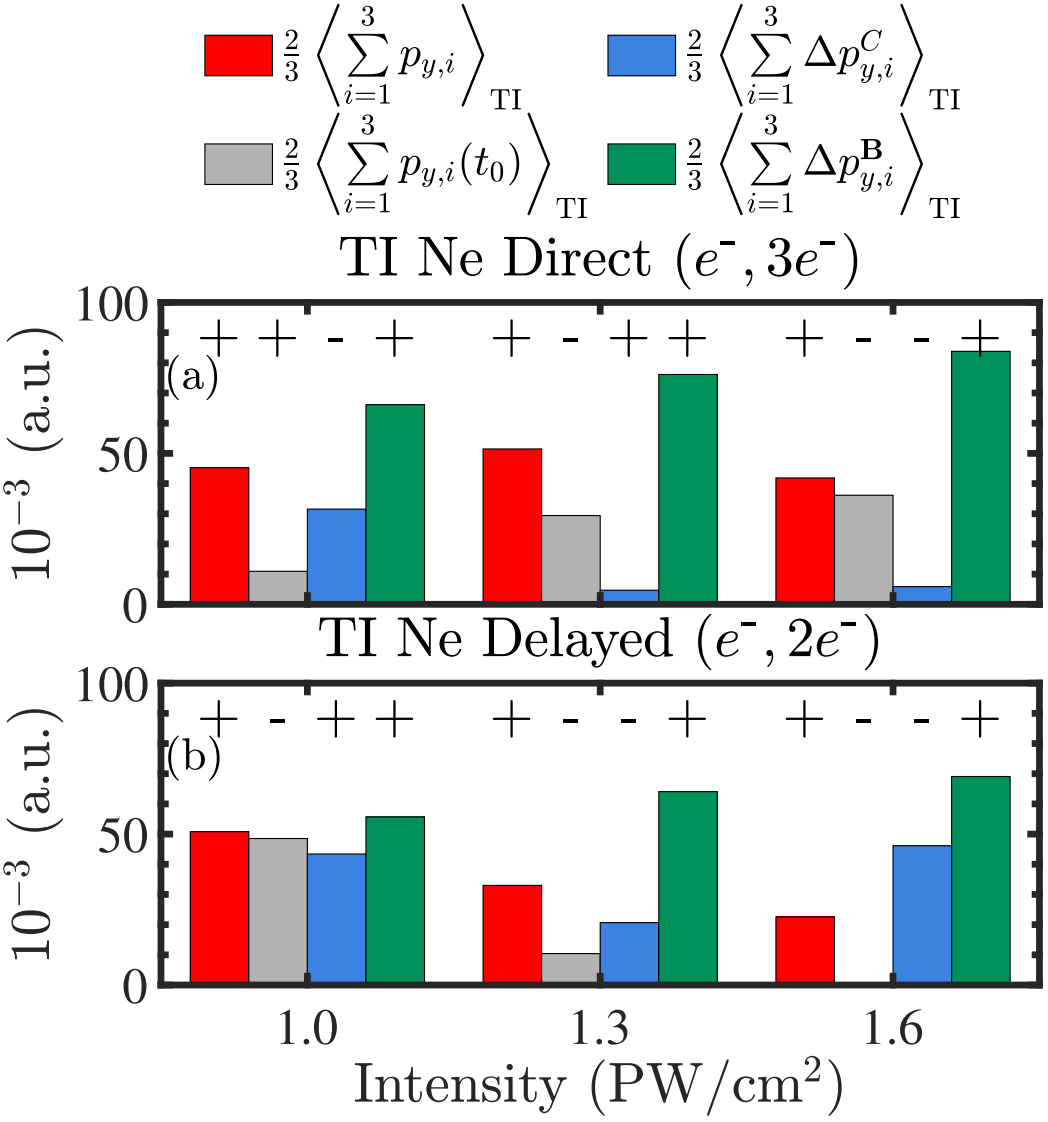

Figure 5.7: For Ne, at each intensity, height of red bar denotes the momentum offset per pair of electrons for TI $2/3\left\langle \sum_{i=1}^{3} p_{y,i} \right\rangle$, the contributions due to the magnetic field $2/3\left\langle \sum_{i=1}^{3} \Delta p^{\mathbf{B}}_{y,i} \right\rangle$ (green bar), due to the initial momentum $2/3\left\langle \sum_{i=1}^{3} p_{y,i}(t_0) \right\rangle$ (gray bar) and due to the Coulomb and effective potential forces $2/3\left\langle \sum_{i=1}^{3} \Delta p^{C}_{y,i} \right\rangle$ (blue bar). The plus (+), minus (-) sign above the bar denotes a positive or negative value, respectively, for the given contribution. The top row corresponds to the direct $(e^-, 3e^-)$ pathway and the bottom row to the delayed $(e^-, 2e^-)$ pathway.

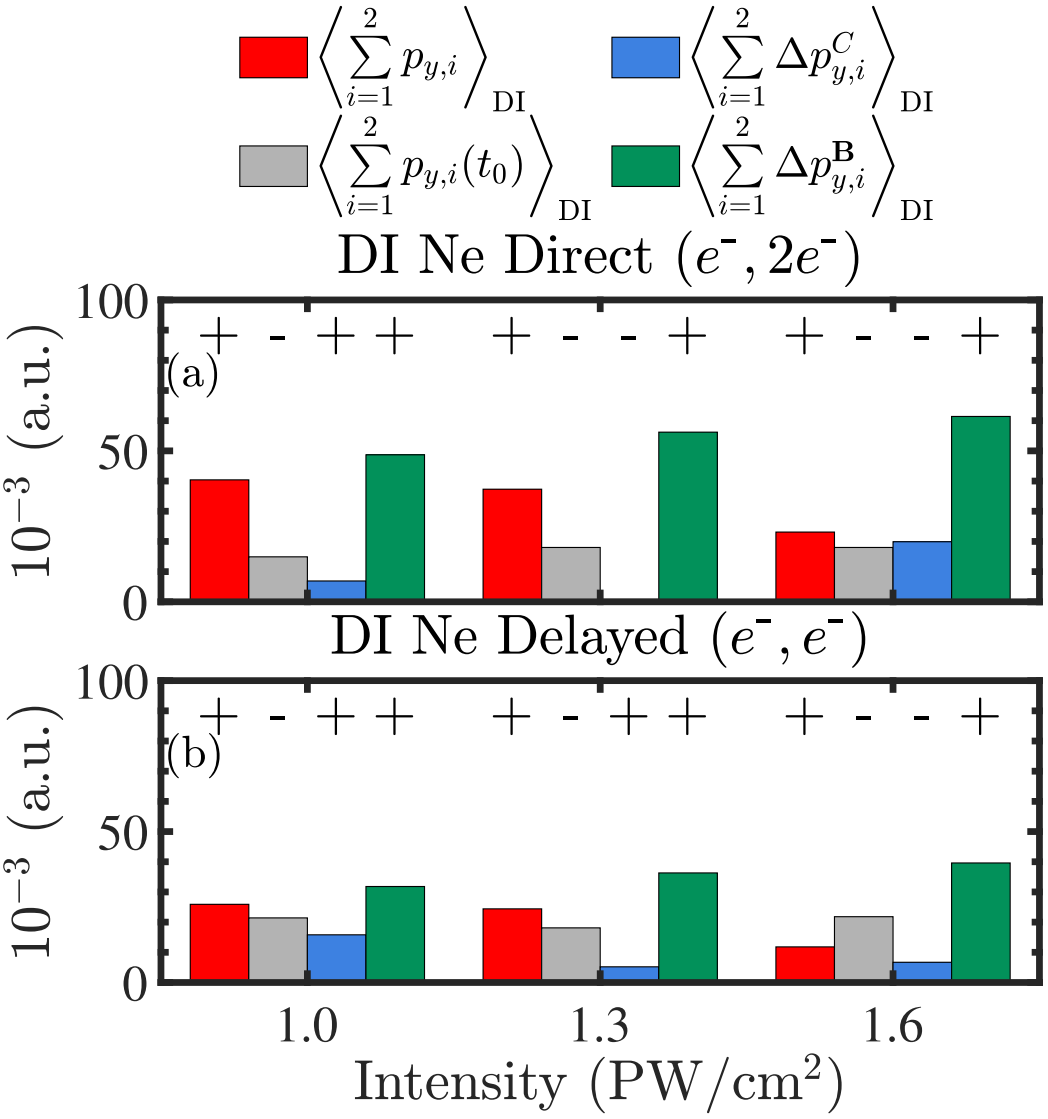

Figure 5.8: For Ne, at each intensity, height of red bar denotes the momentum offset per pair of electrons for DI $\left\langle \sum_{i=1}^{2} p_{y,i} \right\rangle$, the contributions due to the magnetic field $\left\langle \sum_{i=1}^{2} \Delta p^{\mathbf{B}}_{y,i} \right\rangle$ (green bar), due to the initial momentum $\left\langle \sum_{i=1}^{2} p_{y,i}(t_0) \right\rangle$ (gray bar) and due to Coulomb and effective potential forces $\left\langle \sum_{i=1}^{2} \Delta p^{C}_{y,i} \right\rangle$ (blue bar). The plus (+), minus (-) sign above the bar denotes a positive or negative value, respectively, for the given contribution. The top row corresponds to the direct $(e^-, 2e^-)$ pathway and the bottom row to the delayed (e^-, e^-) pathway.

Chapter 6

Conclusions

In this dissertation, we have developed a general model and toolkit to study various attosecond phenomena in three-electron atoms driven by intense and ultra-fast laser pulses. We begin by studying the strongly driven molecule HeH_2^+ and avoid autoionization by turning off the Coulomb force between pairs of electrons. However, we do not account for electron-electron screening between these pairs of bound electrons. Hence, this limits our study to processes which result in one or less electrons remaining bound to the nuclei. Thus, we are only able to describe triple, frustrated triple and double electron ionization in strongly driven HeH_2^+. Motivated by this, we significantly improve upon our previous model by employing effective potentials to describe the interaction between pairs of bound electrons. The interaction between any other pair of electrons is fully described by the Coulomb potential. We use sophisticated methods to determine on the fly during propagation whether electrons are bound or quasifree and also enable smooth switching between effective Coulomb and Coulomb potentials. Thus we fully account for the electron-core Coulomb singularity during propagation and are then able to accurately account for electron recollision dynamics. We have tested this model for Ar and Ne and found the results to outperform other existing semiclassical models and have very good agreement with experiment. Moreover, our model goes beyond the dipole approximation to include nondipole effects. For triple ionization in strongly driven Ne, we find a positive momentum offset of the sum of the ionized electron momenta along the direction of light propagation. This offset being many times larger than what

would be predicted if the electrons were to ionize sequentially. We demonstrate that electron recollisions are responsible for this offset. We propose that this offset can then be used as a probe for correlated electron ionization in strongly driven atoms at medium intensities where magnetic field effects were previously expected to be non-prevalent. In our studies on non-dipole effects, we kept the core fixed since it is not yet known how momentum is shared between the electron and the core during the initial tunnel ionization. We hope our work will motivate future studies to shed light on this.

Multi-electron ionization is currently beyond the reach of quantum mechanical models and is treated inaccurately by other semiclassical models. We consider our model to be an important foundation for future studies in atomic and molecular systems which have been previously untouched due to a lack of appropriate theoretical tools. We note that in its present form, our model currently works for atoms only but can be extended to molecules.

Appendix A

Solving Schrödingers equation in parabolic coordinates

A.1 Derivation of exit point for the tunneling electron

To obtain the exit point for the tunneling electron in our formulation we follow the derivation by Lifshitz [107]. This derivation is detailed below. The Hamiltonian, H, for an electron in 3D with a potential energy due to a net core charge Z=1 and a field along the z axis is

$$\mathrm{H} = \frac{\mathrm{p}^2}{2\mathrm{m}} - \frac{1}{\mathrm{r}} + \mathrm{zE}. \tag{A.1}$$

This can be written in parabolic coordinates

$$\xi = \mathrm{r} + \mathrm{z}, \quad \eta = \mathrm{r} - \mathrm{z}, \quad \mathrm{r} = \frac{1}{2}(\xi + \eta) \quad \text{and} \quad \mathrm{z} = \frac{1}{2}(\xi - \eta), \tag{A.2}$$

where p^2 is described by the corresponding Laplacian operator.

$$\Delta = \frac{4}{\xi + \eta}\left[\frac{\partial}{\partial \xi}\left(\xi \frac{\partial}{\partial \xi}\right) + \frac{\partial}{\partial \eta}\left(\eta \frac{\partial}{\partial \eta}\right)\right] + \frac{1}{\xi \eta}\frac{\partial^2}{\partial \phi^2} \tag{A.3}$$

Schrödinger's equation is given by

$$\left(\frac{1}{2}\Delta - \mathrm{I_p} + \frac{1}{\mathrm{r}} - \mathrm{Ez}\right)\psi = 0 \tag{A.4}$$

$$\frac{4}{\xi+\eta}\left[\frac{\partial}{\partial\xi}\left(\xi\frac{\partial\psi}{\partial\xi}\right)+\frac{\partial}{\partial\eta}\left(\eta\frac{\partial\psi}{\partial\eta}\right)\right]+\frac{1}{\xi\eta}\frac{\partial^2\psi}{\partial\phi^2}+2\left(-\mathrm{I_p}+\frac{2}{\xi+\eta}-\mathrm{E}\frac{\xi-\eta}{2}\right)\psi=0. \tag{A.5}$$

This can be solved by seeking eigenfunctions of the form $\psi=\frac{\mathrm{f_1}(\xi)\mathrm{f_2}(\eta)}{\sqrt{\xi\eta}}\mathrm{e}^{\mathrm{i}m\phi}$, resulting in

$$\left[\frac{\xi}{\mathrm{f_1}}\frac{\mathrm{d}^2\mathrm{f_1}}{\mathrm{d}\xi^2}+\left(-\frac{\xi\mathrm{I_p}}{2}-\frac{\mathrm{m}^2-1}{4\xi}-\frac{1}{4}\mathrm{E}\xi^2\right)\right]+\left[\frac{\eta}{\mathrm{f_2}}\frac{\mathrm{d}^2\mathrm{f_2}}{\mathrm{d}\eta^2}+\left(-\frac{\eta\mathrm{I_p}}{2}-\frac{\mathrm{m}^2-1}{4\eta}+\frac{1}{4}\mathrm{E}\eta^2\right)\right]+1=0 \tag{A.6}$$

or more simply, $-\beta_1-\beta_2+1=0$. This can be split up into 3 main equations for η, ξ and β

$$\begin{aligned}
&\tfrac{\mathrm{d}^2\mathrm{f_1}}{\mathrm{d}\xi^2}+\left(-\tfrac{\mathrm{I_p}}{2}+\tfrac{\beta_1}{\xi}+\tfrac{1}{4\xi^2}-\tfrac{1}{4}\mathrm{E}\xi\right)\mathrm{f_1}=0\\
&\tfrac{\mathrm{d}^2\mathrm{f_2}}{\mathrm{d}\eta^2}+\left(-\tfrac{\mathrm{I_p}}{2}+\tfrac{\beta_2}{\eta}+\tfrac{1}{4\eta^2}+\tfrac{1}{4}\mathrm{E}\eta\right)\mathrm{f_2}=0\\
&\beta_1+\beta_2=1
\end{aligned} \tag{A.7}$$

where we have taken m to be zero. The equation for η can be written in the form of the 1D Schrödinger equation

$$-\frac{1}{2}\frac{\mathrm{d}^2\mathrm{f_2}}{\mathrm{d}\eta^2}+(\mathrm{V}-\varepsilon)\mathrm{f_2}=0, \tag{A.8}$$

where

$$\mathrm{V}=-\frac{\beta_2}{2\eta}-\frac{1}{8\eta^2}-\frac{1}{8}\mathrm{E}\eta \quad \text{and} \quad \varepsilon=-\frac{\mathrm{I_p}}{4}. \tag{A.9}$$

The tunnel exit is found when V=ε. The barrier maximum is found when $\frac{\mathrm{dV}}{\mathrm{d}\eta}=0$. Thus, the exit point $\mathrm{z_{t_0}}(\mathrm{E},\beta_2)$ depends on the field E and β_2, with $\mathrm{t_0}$ being the time of the start of propagation in our model. In previous works [40, 99], β_2 has been set equal to 1/2. The equation for the tunnel exit can be expressed in cubic form

$$\eta^3-\frac{2\mathrm{I_p}\eta^2}{\mathrm{E}}+\frac{4\beta_2\eta}{\mathrm{E}}+\frac{1}{\mathrm{E}}=0 \tag{A.10}$$

where $\mathrm{z_{t_0}}$ is $-\eta_{\mathrm{t_0}}/2$ when the position coordinates of the tunneling electron are assumed to be zero in the x and y axes. This expression for $\mathrm{z_{t_0}}$ is obtained assuming

$\eta >> \xi$. The solutions to cubic equations of the form

$$x^3 + a_2 x^2 + a_1 x + a_0 = 0 \tag{A.11}$$

are well known and given by

$$x = \begin{cases} (s_1 + s_2) - \frac{a_2}{3} \\ -\frac{1}{2}(s_1 + s_2) - \frac{a_2}{3} + i\frac{\sqrt{3}}{2}(s_1 - s_2) \\ -\frac{1}{2}(s_1 + s_2) - \frac{a_2}{3} - i\frac{\sqrt{3}}{2}(s_1 - s_2) \end{cases} \tag{A.12}$$

with $s_1 = \left(r + \sqrt{q^3 + r^2}\right)^{\frac{1}{3}}$, $s_2 = \left(r - \sqrt{q^3 + r^2}\right)^{\frac{1}{3}}$, $q = \frac{a_1}{3} - \frac{a_2^2}{9}$ and $r = \frac{a_1 a_2 - 3a_0}{6} - \frac{a_2^3}{27}$. The coefficients a_2, a_1 and a_0 are found from a comparison between Eqs. (A.10) and (A.11) where $a_2 = -\frac{2I_p}{E}$, $a_1 = \frac{4\beta_2}{E}$ and $a_0 = \frac{1}{E}$. The condition $q^3 + r^2 < 0$ corresponds to the under the barrier regime where all the solutions to Eq. (A.12) are real. The tunneling exit point is the solution from Eq. (A.12) which has the largest magnitude. The over the barrier threshold intensity occurs when $q^3 + r^2 = 0$ and for $q^3 + r^2 > 0$ there is only one real solution to Eq. (A.12). The equation for ξ is given by

$$\xi^3 + \frac{2I_p\xi^2}{E} - \frac{4\beta_2\xi}{E} - \frac{1}{E} = 0. \tag{A.13}$$

The potential curve in η allows for tunneling whereas the potential curve in ξ does not. The authors in Ref. [129] calculated the separation constant β_1 by first obtaining the asymptotic wavefunction of the tunneling electron

$$\psi_C \approx B\frac{2^{-(Z/\kappa)+1}}{|m|!}\xi^{(|m|+1)/2}e^{-\kappa\xi/2}\eta^{Z/\kappa-|m|/2-1/2}e^{-\kappa\eta/2}\frac{e^{im\phi}}{\sqrt{2\pi}} \tag{A.14}$$

and then substituting it in Eq. (A.7). This results in

$$\beta_1 = \frac{(|m|+1)\kappa}{2}, \tag{A.15}$$

assuming that the field is weak, i.e. $E/\kappa^3 << 1$. κ is equal to one in our formulation since we start with neutral atoms. We can then obtain β_2 using Eq. (A.7). In the

case of stronger fields, the authors in Ref. [107] used 2nd order perturbation theory to obtain a correction to the value of β_1.

$$\beta_1 \approx \frac{\kappa}{2} - \frac{E}{2\kappa^2} - \frac{9E^2}{8\kappa^5}. \tag{A.16}$$

Appendix B

Leapfrog Algorithm for time propagation

In what follows, we describe the leapfrog algorithm. First, we initialize the auxiliary variables $\mathbf{W}_0^{\mathbf{q}} = \mathbf{q}_0, \mathbf{W}_0^{\boldsymbol{\rho}} = \boldsymbol{\rho}_0, \mathrm{W}_0^{\mathrm{t}} = \mathrm{t}_0$ and $\mathrm{W}_0^{\mathcal{E}} = \mathcal{E}_0$. Then, we propagate for a time step equal to h, by propagating for half a step each quadruplet of variables $(\mathbf{q}, \mathbf{W}^{\boldsymbol{\rho}}, \mathrm{t}, \mathrm{W}^{\mathcal{E}})$ and $(\mathbf{W}^{\mathbf{q}}, \boldsymbol{\rho}, \mathrm{W}^{\mathrm{t}}, \mathcal{E})$ in an alternating way as follows

$$
\begin{aligned}
\mathbf{q}_{1/2} &= \mathbf{q}_0 + \frac{\mathrm{h}}{2} \frac{\dot{\mathbf{q}}(\mathbf{W}_0^{\mathbf{q}}, \boldsymbol{\rho}_0, \mathrm{W}_0^{\mathrm{t}})}{\Omega(\mathbf{W}_0^{\mathbf{q}})} \\
\mathbf{W}_{1/2}^{\boldsymbol{\rho}} &= \mathbf{W}_0^{\boldsymbol{\rho}} + \frac{\mathrm{h}}{2} \frac{\dot{\boldsymbol{\rho}}(\mathbf{W}_0^{\mathbf{q}}, \boldsymbol{\rho}_0, \mathrm{W}_0^{\mathrm{t}}, \mathcal{E}_0)}{\Omega(\mathbf{W}_0^{\mathbf{q}})} \\
\mathrm{t}_{1/2} &= \mathrm{t}_0 + \frac{\mathrm{h}}{2} \frac{1}{\Omega(\mathbf{W}_0^{\mathbf{q}})} \\
\mathrm{W}_{1/2}^{\mathcal{E}} &= \mathrm{W}_0^{\mathcal{E}} + \frac{\mathrm{h}}{2} \frac{\dot{\mathcal{E}}(\mathbf{W}_0^{\mathbf{q}}, \boldsymbol{\rho}_0, \mathrm{W}_0^{\mathrm{t}}, \mathcal{E}_0)}{\Omega(\mathbf{W}_0^{\mathbf{q}})} \\
\mathbf{W}_1^{\mathbf{q}} &= \mathbf{W}_0^{\mathbf{q}} + \mathrm{h} \frac{\dot{\mathbf{q}}(\mathbf{q}_{1/2}, \mathbf{W}_{1/2}^{\boldsymbol{\rho}}, \mathrm{t}_{1/2})}{\Omega(\mathbf{q}_{1/2})} \\
\boldsymbol{\rho}_1 &= \boldsymbol{\rho}_0 + \mathrm{h} \frac{\dot{\boldsymbol{\rho}}(\mathbf{q}_{1/2}, \mathbf{W}_{1/2}^{\boldsymbol{\rho}}, \mathrm{t}_{1/2}, \mathrm{W}_{1/2}^{\mathcal{E}})}{\Omega(\mathbf{q}_{1/2})} \\
\mathrm{W}_1^{\mathrm{t}} &= \mathrm{W}_0^{\mathrm{t}} + \mathrm{h} \frac{1}{\Omega(\mathbf{q}_{1/2})} \\
\mathcal{E}_1 &= \mathcal{E}_0 + \mathrm{h} \frac{\dot{\mathcal{E}}(\mathbf{q}_{1/2}, \mathbf{W}_{1/2}^{\boldsymbol{\rho}}, \mathrm{t}_{1/2}, \mathrm{W}_{1/2}^{\mathcal{E}})}{\Omega(\mathbf{q}_{1/2})}
\end{aligned}
$$

$$\mathbf{q}_1 = \mathbf{q}_{1/2} + \frac{\mathrm{h}}{2}\frac{\dot{\mathbf{q}}(\mathbf{W}_1^{\mathbf{q}}, \boldsymbol{\rho}_1, \mathrm{W}_1^{\mathrm{t}})}{\Omega(\mathbf{W}_1^{\mathbf{q}})}$$
$$\mathbf{W}_1^{\boldsymbol{\rho}} = \mathbf{W}_{1/2}^{\boldsymbol{\rho}} + \frac{\mathrm{h}}{2}\frac{\dot{\boldsymbol{\rho}}(\mathbf{W}_1^{\mathbf{q}}, \boldsymbol{\rho}_1, \mathrm{W}_1^{\mathrm{t}}, \mathcal{E}_1)}{\Omega(\mathbf{W}_1^{\mathbf{q}})}$$
$$\mathrm{t}_1 = \mathrm{t}_{1/2} + \frac{\mathrm{h}}{2}\frac{1}{\Omega(\mathbf{W}_1^{\mathbf{q}})}$$
$$\mathrm{W}_1^{\mathcal{E}} = \mathrm{W}_{1/2}^{\mathcal{E}} + \frac{\mathrm{h}}{2}\frac{\dot{\mathcal{E}}(\mathbf{W}_1^{\mathbf{q}}, \boldsymbol{\rho}_1, \mathrm{W}_1^{\mathrm{t}}, \mathcal{E}_1)}{\Omega(\mathbf{W}_1^{\mathbf{q}})}$$

The subscripts 0,1/2,1 denote the value of each variable at the start, the middle and the end of the time step h.

Next, we describe the algorithm that incorporates the leapfrog method in the Bulirsch-Stoer extrapolation scheme over a step H, which is split into n sub steps of size $\mathrm{h} = \mathrm{H}/\mathrm{n}$:

$$\mathbf{q}_{1/2} = \mathbf{q}_0 + \frac{\mathrm{h}}{2}\frac{\dot{\mathbf{q}}(\mathbf{W}_0^{\mathbf{q}}, \boldsymbol{\rho}_0, \mathrm{W}_0^{\mathrm{t}})}{\Omega(\mathbf{W}_0^{\mathbf{q}})}$$
$$\mathbf{W}_{1/2}^{\boldsymbol{\rho}} = \mathbf{W}_0^{\boldsymbol{\rho}} + \frac{\mathrm{h}}{2}\frac{\dot{\boldsymbol{\rho}}(\mathbf{W}_0^{\mathbf{q}}, \boldsymbol{\rho}_0, \mathrm{W}_0^{\mathrm{t}}, \mathcal{E}_0)}{\Omega(\mathbf{W}_0^{\mathbf{q}})}$$
$$\mathrm{t}_{1/2} = \mathrm{t}_0 + \frac{\mathrm{h}}{2}\frac{1}{\Omega(\mathbf{W}_0^{\mathbf{q}})}$$
$$\mathrm{W}_{1/2}^{\mathcal{E}} = \mathrm{W}_0^{\mathcal{E}} + \frac{\mathrm{h}}{2}\frac{\dot{\mathcal{E}}(\mathbf{W}_0^{\mathbf{q}}, \boldsymbol{\rho}_0, \mathrm{W}_0^{\mathrm{t}}, \mathcal{E}_0)}{\Omega(\mathbf{W}_0^{\mathbf{q}})}$$
$$\mathbf{W}_1^{\mathbf{q}} = \mathbf{W}_0^{\mathbf{q}} + \mathrm{h}\frac{\dot{\mathbf{q}}(\mathbf{q}_{1/2}, \mathbf{W}_{1/2}^{\boldsymbol{\rho}}, \mathrm{t}_{1/2})}{\Omega(\mathbf{q}_{1/2})}$$
$$\boldsymbol{\rho}_1 = \boldsymbol{\rho}_0 + \mathrm{h}\frac{\dot{\boldsymbol{\rho}}(\mathbf{q}_{1/2}, \mathbf{W}_{1/2}^{\boldsymbol{\rho}}, \mathrm{t}_{1/2}, \mathrm{W}_{1/2}^{\mathcal{E}})}{\Omega(\mathbf{q}_{1/2})}$$
$$\mathrm{W}_1^{\mathrm{t}} = \mathrm{W}_0^{\mathrm{t}} + \mathrm{h}\frac{1}{\Omega(\mathbf{q}_{1/2})}$$
$$\mathcal{E}_1 = \mathcal{E}_0 + \mathrm{h}\frac{\dot{\mathcal{E}}(\mathbf{q}_{1/2}, \mathbf{W}_{1/2}^{\boldsymbol{\rho}}, \mathrm{t}_{1/2}, \mathrm{W}_{1/2}^{\mathcal{E}})}{\Omega(\mathbf{q}_{1/2})}$$
$$\vdots$$
$$\mathbf{q}_{\mathrm{m}-1/2} = \mathbf{q}_{\mathrm{m}-3/2} + \mathrm{h}\frac{\dot{\mathbf{q}}(\mathbf{W}_{\mathrm{m}-1}^{\mathbf{q}}, \boldsymbol{\rho}_{\mathrm{m}-1}, \mathrm{W}_{\mathrm{m}-1}^{\mathrm{t}})}{\Omega(\mathbf{W}_{\mathrm{m}-1}^{\mathbf{q}})}$$

$$
\begin{aligned}
\mathbf{W}^{\boldsymbol{\rho}}_{\mathrm{m}-1/2} &= \mathbf{W}^{\boldsymbol{\rho}}_{\mathrm{m}-3/2} + \mathrm{h}\frac{\dot{\boldsymbol{\rho}}(\mathbf{W}^{\mathbf{q}}_{\mathrm{m}-1}, \boldsymbol{\rho}_{\mathrm{m}-1}, \mathrm{W}^{\mathrm{t}}_{\mathrm{m}-1}, \mathcal{E}_{\mathrm{m}-1})}{\Omega(\mathbf{W}^{\mathbf{q}}_{\mathrm{m}-1})} \\
\mathrm{t}_{\mathrm{m}-1/2} &= \mathrm{t}_{\mathrm{m}-3/2} + \mathrm{h}\frac{1}{\Omega(\mathbf{W}^{\mathbf{q}}_{\mathrm{m}-1})} \\
\mathrm{W}^{\mathcal{E}}_{\mathrm{m}-1/2} &= \mathrm{W}^{\mathcal{E}}_{\mathrm{m}-3/2} + \mathrm{h}\frac{\dot{\mathcal{E}}(\mathbf{W}^{\mathbf{q}}_{\mathrm{m}-1}, \boldsymbol{\rho}_{\mathrm{m}-1}, \mathrm{W}^{\mathrm{t}}_{\mathrm{m}-1}, \mathcal{E}_{\mathrm{m}-1})}{\Omega(\mathbf{W}^{\mathbf{q}}_{\mathrm{m}-1})} \\
\mathbf{W}^{\mathbf{q}}_{\mathrm{m}} &= \mathbf{W}^{\mathbf{q}}{}_{\mathrm{m}-1} + \mathrm{h}\frac{\dot{\mathbf{q}}(\mathbf{q}_{\mathrm{m}-1/2}, \mathbf{W}^{\boldsymbol{\rho}}_{\mathrm{m}-1/2}, \mathrm{t}_{\mathrm{m}-1/2})}{\Omega(\mathbf{q}_{\mathrm{m}-1/2})} \\
\boldsymbol{\rho}_{\mathrm{m}} &= \boldsymbol{\rho}_{\mathrm{m}-1} + \mathrm{h}\frac{\dot{\boldsymbol{\rho}}(\mathbf{q}_{\mathrm{m}-1/2}, \mathbf{W}^{\boldsymbol{\rho}}_{\mathrm{m}-1/2}, \mathrm{t}_{\mathrm{m}-1/2}, \mathrm{W}^{\mathcal{E}}_{\mathrm{m}-1/2})}{\Omega(\mathbf{q}_{\mathrm{m}-1/2})} \\
\mathrm{W}^{\mathrm{t}}_{\mathrm{m}} &= \mathrm{W}^{\mathrm{t}}_{\mathrm{m}-1} + \mathrm{h}\frac{1}{\Omega(\mathbf{q}_{\mathrm{m}-1/2})} \\
\mathcal{E}_{\mathrm{m}} &= \mathcal{E}_{\mathrm{m}-1} + \mathrm{h}\frac{\dot{\mathcal{E}}(\mathbf{q}_{\mathrm{m}-1/2}, \mathbf{W}^{\boldsymbol{\rho}}_{\mathrm{m}-1/2}, \mathrm{t}_{\mathrm{m}-1/2}, \mathrm{W}^{\mathcal{E}}_{\mathrm{m}-1/2})}{\Omega(\mathbf{q}_{\mathrm{m}-1/2})} \\
&\vdots \\
\mathbf{W}^{\mathbf{q}}_{\mathrm{n}} &= \mathbf{W}^{\mathbf{q}}{}_{\mathrm{n}-1} + \mathrm{h}\frac{\dot{\mathbf{q}}(\mathbf{q}_{\mathrm{n}-1/2}, \mathbf{W}^{\boldsymbol{\rho}}_{\mathrm{n}-1/2}, \mathrm{t}_{\mathrm{n}-1/2})}{\Omega(\mathbf{q}_{\mathrm{n}-1/2})} \\
\boldsymbol{\rho}_{\mathrm{n}} &= \boldsymbol{\rho}_{\mathrm{n}-1} + \mathrm{h}\frac{\dot{\boldsymbol{\rho}}(\mathbf{q}_{\mathrm{n}-1/2}, \mathbf{W}^{\boldsymbol{\rho}}_{\mathrm{n}-1/2}, \mathrm{t}_{\mathrm{n}-1/2}, \mathrm{W}^{\mathcal{E}}_{\mathrm{n}-1/2})}{\Omega(\mathbf{q}_{\mathrm{n}-1/2})} \\
\mathrm{W}^{\mathrm{t}}_{\mathrm{n}} &= \mathrm{W}^{\mathrm{t}}_{\mathrm{n}-1} + \mathrm{h}\frac{1}{\Omega(\mathbf{q}_{\mathrm{n}-1/2})} \\
\mathcal{E}_{\mathrm{n}} &= \mathcal{E}_{\mathrm{n}-1} + \mathrm{h}\frac{\dot{\mathcal{E}}(\mathbf{q}_{\mathrm{n}-1/2}, \mathbf{W}^{\boldsymbol{\rho}}_{\mathrm{n}-1/2}, \mathrm{t}_{\mathrm{n}-1/2}, \mathrm{W}^{\mathcal{E}}_{\mathrm{n}-1/2})}{\Omega(\mathbf{q}_{\mathrm{n}-1/2})} \\
\mathbf{q}_{\mathrm{n}} &= \mathbf{q}_{\mathrm{n}-1/2} + \frac{\mathrm{h}}{2}\frac{\dot{\mathbf{q}}(\mathbf{W}^{\mathbf{q}}_{\mathrm{n}}, \boldsymbol{\rho}_{\mathrm{n}}, \mathrm{W}^{\mathrm{t}}_{\mathrm{n}})}{\Omega(\mathbf{W}^{\mathbf{q}}_{\mathrm{n}})} \\
\mathbf{W}^{\boldsymbol{\rho}}_{\mathrm{n}} &= \mathbf{W}^{\boldsymbol{\rho}}_{\mathrm{n}-1/2} + \frac{\mathrm{h}}{2}\frac{\dot{\boldsymbol{\rho}}(\mathbf{W}^{\mathbf{q}}_{\mathrm{n}}, \boldsymbol{\rho}_{\mathrm{n}}, \mathrm{W}^{\mathrm{t}}_{\mathrm{n}}, \mathcal{E}_{\mathrm{n}})}{\Omega(\mathbf{W}^{\mathbf{q}}_{\mathrm{n}})} \\
\mathrm{t}_{\mathrm{n}} &= \mathrm{t}_{\mathrm{n}-1/2} + \frac{\mathrm{h}}{2}\frac{1}{\Omega(\mathbf{W}^{\mathbf{q}}_{\mathrm{n}})} \\
\mathrm{W}^{\mathcal{E}}_{\mathrm{n}} &= \mathrm{W}^{\mathcal{E}}_{\mathrm{n}-1/2} + \frac{\mathrm{h}}{2}\frac{\dot{\mathcal{E}}(\mathbf{W}^{\mathbf{q}}_{\mathrm{n}}, \boldsymbol{\rho}_{\mathrm{n}}, \mathrm{W}^{\mathrm{t}}_{\mathrm{n}}, \mathcal{E}_{\mathrm{n}})}{\Omega(\mathbf{W}^{\mathbf{q}}_{\mathrm{n}})}
\end{aligned}
$$

where m=2,...,n-1.

Appendix C

Compact equations of motion for computational purposes

In Sec. 2.2.4 we have introduced fictitious particles

$$k(i,j) = (i-1)N - \frac{i(i+1)}{2} + j, \tag{C.1}$$

where N is the actual number of particles. In addition, we have defined the parameters α_{ik} and β_{ik}, as $\alpha_{ik} = 1, \beta_{ik} = m_j/M$ and $\alpha_{jk} = -1, \beta_{jk} = -m_i/M$ when $k = k(i,j)$ and j>i, otherwise $\alpha_{ik} = \beta_{ik} = 0$. In order to write Eq. (3.5) in a compact way, we follow the procedure outlined below. We start considering N=3, which corresponds to K=3 and i,j = 1,2,3. In Tab. C.1, we show for what indices of α_{ak} the latter has a non-zero value. Finally, we multiply k and α_{ak} to obtain Tab. C.2. Next, we put the values of k' in a matrix form in Tab. C.2 which has dimensions N×N-1.

a	a′	k	α_{ak}
1	2	1	1
1	3	2	1
2	1	1	-1
2	3	3	1
3	1	2	-1
3	2	3	-1

or more compactly

a	a′	k	α_{ak}
1	(2,3)	(1,2)	(1,1)
2	(1,3)	(1,3)	(-1, 1)
3	(1,2)	(2,3)	(-1,-1)

Table C.1: For N=3 particles, for given values of a, we find the values of a' and k that result in α_{ak} being non-zero. Positive values of α_{ak} occur for $k = k(a,a')$ and negative ones for $k = k(a',a)$.

N=3

a	a′	k′
1	(2,3)	(1,2)
2	(1,3)	(-1,3)
3	(1,2)	(-2,-3)

N=4

a	a′	k′
1	(2,3,4)	(1,2,3)
2	(1,3,4)	(-1,4,5)
3	(1,2,4)	(-2,-4,6)
4	(1,2,3)	(-3,-5,-6)

N=5

a	a′	k′
1	(2,3,4,5)	(1,2,3,4)
2	(1,3,4,5)	(-1,5,6,7)
3	(1,2,4,5)	(-2,-5,8,9)
4	(1,2,3,5)	(-3,-6,-8,10)
5	(1,2,3,4)	(-4,-7,-9,-10)

Table C.2: For N=3,4 and 5 particles, for given values of a, we find the values of a′ and k that result in α_{ak} being non-zero. Positive values of α_{ak} occur for $k = k(a,a')$ and negative ones for $k = k(a',a)$. The column labelled k′ is the product of the k and α_{ak} columns in Tab. C.1.

The dimensions N×N-1 follow from the fact that the index "a" in Tab. C.1 runs over the number of particles and the number of values that k′ takes are N-1 since j>i. Below we write the matrices for N=3, N=4 and N=5 particles.

$$\mathbf{M}_3^k = \begin{pmatrix} 1 & 2 \\ -1 & 3 \\ -2 & -3 \end{pmatrix}, \mathbf{M}_4^k = \begin{pmatrix} 1 & 2 & 3 \\ -1 & 4 & 5 \\ -2 & -4 & 6 \\ -3 & -5 & -6 \end{pmatrix}$$

$$\mathbf{M}_5^k = \begin{pmatrix} 1 & 2 & 3 & 4 \\ -1 & 5 & 6 & 7 \\ -2 & -5 & 8 & 9 \\ -3 & -6 & -8 & 10 \\ -4 & -7 & -9 & -10 \end{pmatrix}$$

In what follows, the entries of the $\mathbf{M}_{\mathrm{N}}^{\mathrm{k}}$ matrix

$$\mathbf{M}_{\mathrm{N}}^{\mathrm{k}} = \begin{pmatrix} M(0,0) & M(0,1) & ... & M(0,N-2) \\ M(1,0) & M(1,1) & ... & M(1,N-2) \\ M(...,0) & M(...,1) & ... & M(...,N-2) \\ M(N-1,0) & M(N-1,1) & ... & M(N-1,N-2) \end{pmatrix}$$

are given by

1. Element M(0,0) is 1.
2. Elements M(m,n) increase according to M(m,m) = M(m − 1,m − 1) + (N-m).
3. Elements M(m + 1,m) = -Elements M(m,m)
4. Elements M(m,n) = M(m − 1,n) -1, if m>n+1 .
5. Elements M(m,n) = M(m,n − 1) +1, if n>m .

This is sufficient to produce the relevant matrix $\mathbf{M}_{\mathrm{N}}^{\mathrm{k}}$ for any number of particles N. Now the first term of Eq. (3.5) can be rewritten as

$$\mathbf{J}_{\mathrm{a}} = \sum_{\mathrm{k}=1}^{\mathrm{K}} \alpha_{\mathrm{ak}} \boldsymbol{\rho}_{\mathrm{k}} = \sum_{\mathrm{d}=0}^{\mathrm{N}-2} \mathrm{sgn}[\mathbf{k}] \boldsymbol{\rho}_{|\mathbf{k}|}, \tag{C.2}$$

with $\mathbf{k} = \mathbf{M}_{\mathrm{N}}^{\mathrm{k}}(\mathrm{a}-1,\mathrm{d})$. The function sgn(x) returns +1 if x>0 and -1 if x<0. We note that the matrix $\mathbf{M}_{\mathrm{N}}^{\mathrm{k}}$ has an index starting from 0, this is the reason why the summation runs from d=0. The advantage of this formulation is that the summation from 0 to N-2 takes less computational time than a summation from 1 to K, and it also removes the addition of zeros in the code. For computational reasons, we define two more matrices in the code, one with $\mathrm{sgn}(\mathbf{M}_{\mathrm{N}}^{\mathrm{k}})$ and one with the absolute value of the entries of $\mathbf{M}_{\mathrm{N}}^{\mathrm{k}}$, i.e. $|\mathbf{M}_{\mathrm{N}}^{\mathrm{k}}|$. In what follows, we illustrate Eq. (C.2) for a few examples.

For N=4 and K=6, what is $\mathbf{J}_{\mathrm{a}} = \sum_{\mathrm{k}=1}^{\mathrm{K}} \alpha_{\mathrm{ak}} \boldsymbol{\rho}_{\mathrm{k}}$ for a=1?

Answer: $\boldsymbol{\rho}_1 + \boldsymbol{\rho}_2 + \boldsymbol{\rho}_3$

For N=4 and K=6, what is $\mathbf{J}_a = \sum_{k=1}^{K} \alpha_{ak}\boldsymbol{\rho}_k$ for a=4?

Answer: -$\boldsymbol{\rho}_3$ - $\boldsymbol{\rho}_5$ - $\boldsymbol{\rho}_6$

For N=5 and K=10, what is $\mathbf{J}_a = \sum_{k=1}^{K} \alpha_{ak}\boldsymbol{\rho}_k$ for a=3?

Answer: -$\boldsymbol{\rho}_2$ - $\boldsymbol{\rho}_5$ + $\boldsymbol{\rho}_8$+ $\boldsymbol{\rho}_9$

Next, we follow a similar procedure as before, to express in a compact way the position vectors $\mathbf{r}_i$, see Eq. (2.15). The method is similar to Eq. (C.2) except that we introduce another matrix $\mathbf{M}_N^m$ with elements being the indices of the masses of the particles. We obtain the matrices for N=3,4 and 5 from Tab. C.1, where for each row, we skip the element corresponding the index plus 1, i.e. for the first row (a=1), we skip 1, for the second (a=2) we skip 2 etc. It seems that the pattern observed for particles up to N=5, where in each row we skip the value of the row index, is a general pattern, however this needs to be verified. The index of the mass can then be computed using the below matrices,

$$\mathbf{M}_3^m = \begin{pmatrix} 2 & 3 \\ 1 & 3 \\ 1 & 2 \end{pmatrix}, \mathbf{M}_4^m = \begin{pmatrix} 2 & 3 & 4 \\ 1 & 3 & 4 \\ 1 & 2 & 4 \\ 1 & 2 & 3 \end{pmatrix}, \mathbf{M}_5^m = \begin{pmatrix} 2 & 3 & 4 & 5 \\ 1 & 3 & 4 & 5 \\ 1 & 2 & 4 & 5 \\ 1 & 2 & 3 & 5 \\ 1 & 2 & 3 & 4 \end{pmatrix}$$

Now the first term of Eq. (2.15) can be rewritten as

$$\mathbf{Q}_a = \sum_{k=1}^{K} \beta_{ak}\mathbf{q}_k = \frac{1}{M}\sum_{d=0}^{N-2} \mathrm{sgn}[\mathbf{k}]\mathbf{q}_{|\mathbf{k}|}m_{a'}. \tag{C.3}$$

with $\mathbf{k} = \mathbf{M}_N^k(a-1,d)$ and $a' = \mathbf{M}_N^m(a-1,d)$.

For N=4 and K=6, what is $Q_a = \sum_{k=1}^{K} \beta_{ak}\mathbf{q}_k$ for i=1?

Answer: $\frac{1}{M}(\mathbf{q}_1 m_2 + \mathbf{q}_2 m_3 + \mathbf{q}_3 m_4)$

For N=4 and K=6, what is $Q_a = \sum_{k=1}^{K} \beta_{ak}\mathbf{q}_k$ for a=4?

Answer: $\frac{1}{M}\left(-\mathbf{q}_3 m_1 - \mathbf{q}_5 m_2 - \mathbf{q}_6 m_3\right)$

For N=5 and K=10, what is $Q_a = \sum_{k=1}^{K} \beta_{ak}\mathbf{q}_k$ for i=3?

Answer: $\frac{1}{M}\left(-\mathbf{q}_2 m_1 - \mathbf{q}_5 m_2 + \mathbf{q}_8 m_4 + \mathbf{q}_9 m_5\right)$

In order to write Eq. (3.20) in a more compact way, we follow the procedure below where Eq. (3.20) is first expressed in regularized coordinates.

$$
\begin{aligned}
\dot{\mathcal{E}}_a(t) &= \sum_{i=2}^{N-1}\sum_{m=i+1}^{N}\left[1-c_{i,m}(t)\right]\frac{Q_i Q_m(\mathbf{r}_i-\mathbf{r}_m)}{|\mathbf{r}_i-\mathbf{r}_m|^3}\left(\delta_{i,a}-\delta_{m,a}\right)\cdot\dot{\mathbf{r}}_a \\
&+\left[-\frac{Q_1 Q_a(\mathbf{r}_1-\mathbf{r}_a)}{|\mathbf{r}_1-\mathbf{r}_a|^3}+\sum_{\substack{i=2\\ i\neq a}}^{N} c_{i,a}(t)\frac{\partial V_{\text{eff}}(\zeta_i,|\mathbf{r}_1-\mathbf{r}_a|}{\partial \mathbf{r}_1}\right]\cdot\dot{\mathbf{r}}_1 \\
&+\sum_{\substack{i=2\\ i\neq a}}^{N}\left[c_{i,a}(t)\frac{\partial V_{\text{eff}}(\zeta_i,|\mathbf{r}_1-\mathbf{r}_a|)}{\partial \zeta_i}\dot{\zeta}_i+\dot{c}_{i,a}(t)V_{\text{eff}}(\zeta_i,|\mathbf{r}_1-\mathbf{r}_a|)\right] \\
&-Q_a\mathbf{r}_a\cdot\dot{\mathbf{E}}\left(\mathbf{r}_a,t\right) \\
&=\sum_{k''=4}^{K}\alpha_{ak''}\left[1-c_{k''}(t)\right]\frac{U_{k''}\mathbf{q}_{k''}}{q_{k''}^3}\cdot\dot{\mathbf{r}}_a-Q_a\mathbf{r}_a\cdot\dot{\mathbf{E}}\left(\mathbf{r}_a,t\right) \\
&+\left[-\frac{U_{k(1,a)}\mathbf{q}_{k(1,a)}}{q_{k(1,a)}^3}+\sum_{\substack{i=2\\ i\neq a}}^{N} c_{i,a}(t)\frac{\partial V_{\text{eff}}(\zeta_i,|\mathbf{r}_1-\mathbf{r}_a|}{\partial(\mathbf{r}_1-\mathbf{r}_a)}\frac{\partial(\mathbf{r}_1-\mathbf{r}_a)}{\partial \mathbf{r}_1}\right]\cdot\dot{\mathbf{r}}_1 \\
&+\sum_{k''=4}^{K}\alpha_{ak''}^2\left[c_{k''}(t)\frac{\partial V_{\text{eff}}(\zeta_{a'},q_{k(1,a)})}{\partial \zeta_{a'}}\dot{\zeta}_{a'}+\dot{c}_{k''}(t)V_{\text{eff}}(\zeta_{a'},q_{k(1,a)})\right] \\
&=\sum_{k''=4}^{K}\alpha_{ak''}\left[1-c_{k''}(t)\right]\frac{U_{k''}\mathbf{q}_{k''}}{q_{k''}^3}\cdot\dot{\mathbf{r}}_a-Q_a\mathbf{r}_a\cdot\dot{\mathbf{E}}\left(\mathbf{r}_a,t\right) \\
&+\left[-\frac{U_{k(1,a)}\mathbf{q}_{k(1,a)}}{q_{k(1,a)}^3}+\sum_{k''=4}^{K}\alpha_{ak''}^2 c_{k''}\frac{\partial V_{\text{eff}}(\zeta_{a'},q_{k(1,a)})}{\partial \mathbf{q}_{k(1,a)}}\right]\cdot\dot{\mathbf{r}}_1 \\
&+\sum_{k''=4}^{K}\alpha_{ak''}^2\left[c_{k''}(t)\frac{\partial V_{\text{eff}}(\zeta_{a'},q_{k(1,a)})}{\partial \zeta_{a'}}\dot{\zeta}_{a'}+\dot{c}_{k''}(t)V_{\text{eff}}(\zeta_{a'},q_{k(1,a)})\right]
\end{aligned}
\tag{C.4}
$$

where

$$\sum_{\substack{i=2\\ i\neq j}}^{N} c_{i,a}(t) f(i) = \sum_{k''=4}^{K} \alpha_{ak''}^2 c_{k''}(t) f(a') \tag{C.5}$$

with a' satisfying either $k''=k''(a,a')$ or $k''=k''(a',a)$ as seen in Tab. C.2. The above summations include all electron pairs that contain electron a. The summation in Eq. (C.4) over fictitious particle k starts from 4 since for N=4 this is the first fictitious particle that corresponds to an electron-electron interaction. In order to write Eq. (3.20) in a more compact form, we follow a similar procedure as outlined earlier in this appendix. The different summations from Eq. (C.4) can be compacted as shown below

$$\sum_{k''=4}^{K} \alpha_{ak''} [1 - c_{k''}(t)] \frac{U_{k''} \mathbf{q}_{k''}}{q_{k''}^3} = \sum_{d=0}^{N_e-2} \mathrm{sgn}(\mathbf{k}^e) \left[1 - c_{|\mathbf{k}^e|}\right] \frac{U_{|\mathbf{k}^e|} \mathbf{q}_{|\mathbf{k}^e|}}{q_{|\mathbf{k}^e|}^3}, \tag{C.6}$$

$$\sum_{k''=4}^{K} \alpha_{ak''}^2 c_{k''} \frac{\partial V_{\mathrm{eff}}(\zeta_{a'}, q_{k(1,a)})}{\partial \mathbf{q}_{k(1,a)}} = \sum_{d=0}^{N_e-2} c_{|\mathbf{k}^e|} \frac{\partial V_{\mathrm{eff}}(\zeta_{a'^e}, q_{k(1,a)})}{\partial \mathbf{q}_{k(1,a)}}, \tag{C.7}$$

$$\begin{aligned} &\sum_{k''=4}^{K} \alpha_{ak''}^2 \left[c_{k''}(t) \frac{\partial V_{\mathrm{eff}}(\zeta_{a'}, q_{k(1,a)})}{\partial \zeta_{a'}} \dot{\zeta}_{a'} + \dot{c}_{k''}(t) V_{\mathrm{eff}}(\zeta_{a'}, q_{k(1,a)}) \right] \\ &= \sum_{d=0}^{N_e-2} \left[c_{|\mathbf{k}^e|}(t) \frac{\partial V_{\mathrm{eff}}(\zeta_{a'^e}, q_{k(1,a)})}{\partial \zeta_{a'^e}} \dot{\zeta}_{a'^e} + \dot{c}_{|\mathbf{k}^e|}(t) V_{\mathrm{eff}}(\zeta_{a'^e}, q_{k(1,a)}) \right], \end{aligned} \tag{C.8}$$

with $\mathbf{k}^e = \mathbf{M}_{N_e}^{k,e}(a-1-N_{\mathrm{nuc}}, d)$ and $a'^e = \mathbf{M}_{N_e}^{m,e}(a-1-N_{\mathrm{nuc}}, d)$. N_e is the number of electrons rather than the number of particles as seen in Eq. (C.2) and N_{nuc} is the number of nuclei. The index "a" starts from N_{nuc} +1 since it describes electrons only. The matrices $\mathbf{M}_{N_e}^{k,e}$ and $\mathbf{M}_{N_e}^{m,e}$ of dimensions $N_e \times (N_e - 1)$ are obtained by removing rows and columns from $\mathbf{M}_N^k$ and $\mathbf{M}_N^m$ which contain particle pairs that include the nucleus. The calculation of $-Q_a \mathbf{r}_a \cdot \left(\frac{\partial \mathbf{E}(\mathbf{r}_a,t)}{\partial \mathbf{r}_a} \cdot \dot{\mathbf{r}}_a \right) - Q_a \mathbf{r}_a \cdot \frac{\partial \mathbf{E}(\mathbf{r}_a,t)}{\partial t} = -Q_a \mathbf{r}_a \cdot \dot{\mathbf{E}}(\mathbf{r}_a, t)$ is given in Sec. D.2.3.

Next, we compact some of the terms in Eq. (3.25). The first term in Eq. (3.25), see Sec. 3.23, is given by

$$\frac{d\mathbf{q}_k}{dt} = 2 \sum_{k'=1}^{K} T_{kk'} \boldsymbol{\rho}_{k'} \tag{C.9}$$

where

$$T_{kk'} = \sum_{a=1}^{N} \frac{\alpha_{ak}\alpha_{ak'}}{2m_a}. \tag{C.10}$$

For a given $k = k(i,j)$, $T_{kk'}$ can only be non-zero when $a = i$ or j, otherwise α_{ak} would be 0 . Thus, we can rewrite Eq. (C.9) as

$$\begin{aligned}
\frac{d\mathbf{q}_{k(i,j)}}{dt} &= \sum_{k'=1}^{K} \left(\frac{\alpha_{ik}\alpha_{ik'}}{m_i} + \frac{\alpha_{jk}\alpha_{jk'}}{m_j} \right) \boldsymbol{\rho}_{k'} \\
&= \sum_{k'=1}^{K} \left(\frac{\alpha_{ik'}}{m_i} - \frac{\alpha_{jk'}}{m_j} \right) \boldsymbol{\rho}_{k'} \\
&= \sum_{k'=1}^{K} \frac{\alpha_{ik'}}{m_i} \boldsymbol{\rho}_{k'} - \sum_{k'=1}^{K} \frac{\alpha_{jk'}}{m_j} \boldsymbol{\rho}_{k'} \\
&= \frac{1}{m_i} \sum_{k'=1}^{K} \alpha_{ik'} \boldsymbol{\rho}_{k'} - \frac{1}{m_j} \sum_{k'=1}^{K} \alpha_{jk'} \boldsymbol{\rho}_{k'} \\
&= \frac{1}{m_i} \mathbf{J}_i - \frac{1}{m_j} \mathbf{J}_j
\end{aligned} \tag{C.11}$$

where we obtain $\mathbf{J}_i$ and $\mathbf{J}_j$ from Eq. (C.2). The terms $-\sum_{a=1}^{N} \frac{Q_a}{m_a} \alpha_{ak} \mathbf{A}(\mathbf{r}_a, t)$ and $\sum_{a=1}^{N} \frac{Q_a}{m_a} [\tilde{\mathbf{p}}_a - Q_a \mathbf{A}(\mathbf{r}_a, t)] \cdot \frac{\partial \mathbf{A}(\mathbf{r}_a, t)}{\partial \mathbf{q}_k}$ from Eq. (3.25) can be simplified using the same logic as in Eq. (C.11), i.e. for a given k=k(i,j), α_{ak} and β_{ak} can only be non-zero for a=i or j. These are simplified as follows

$$\begin{aligned}
-\sum_{a=1}^{N} \frac{Q_a}{m_a} \alpha_{ak} \mathbf{A}(\mathbf{r}_a, t) &= -\frac{Q_i}{m_i} \alpha_{ik} \mathbf{A}(\mathbf{r}_i, t) - \frac{Q_j}{m_j} \alpha_{jk} \mathbf{A}(\mathbf{r}_j, t) \\
&= -\frac{Q_i}{m_i} \mathbf{A}(\mathbf{r}_i, t) + \frac{Q_j}{m_j} \mathbf{A}(\mathbf{r}_j, t)
\end{aligned} \tag{C.12}$$

$$\begin{aligned}
\sum_{a=1}^{N} \frac{Q_a}{m_a} [\tilde{\mathbf{p}}_a - Q_a \mathbf{A}(\mathbf{r}_a, t)] \cdot \frac{\partial \mathbf{A}(\mathbf{r}_a, t)}{\partial \mathbf{q}_k} &= \sum_{a=1}^{N} \frac{Q_a}{m_a} [\tilde{\mathbf{p}}_a - Q_a \mathbf{A}(\mathbf{r}_a, t)] \cdot \frac{\partial \mathbf{A}(\mathbf{r}_a, t)}{\partial \mathbf{r}_a} \beta_{ak} \\
&= \frac{Q_i}{m_i} \mathbf{p}_i \cdot \frac{\partial \mathbf{A}(\mathbf{r}_i, t)}{\partial \mathbf{r}_i} \beta_{ik} + \frac{Q_j}{m_j} \mathbf{p}_j \cdot \frac{\partial \mathbf{A}(\mathbf{r}_j, t)}{\partial \mathbf{r}_j} \beta_{jk} \\
&= \frac{Q_i m_j}{m_i M} \mathbf{p}_i \cdot \frac{\partial \mathbf{A}(\mathbf{r}_i, t)}{\partial \mathbf{r}_i} - \frac{Q_j m_i}{m_j M} \mathbf{p}_j \cdot \frac{\partial \mathbf{A}(\mathbf{r}_j, t)}{\partial \mathbf{r}_j}
\end{aligned} \tag{C.13}$$

Finally, using Eq. (3.26), the term $-\sum_{k'=1}^{K} c_{k'}(t)\frac{\partial V_{k'}}{\partial \mathbf{q}_k}$ from Eq. (3.25) can be written as follows

$$
\begin{aligned}
-\sum_{k'=4}^{K} c_{k'}(t)\frac{\partial V_{k'}}{\partial \mathbf{q}_k} &= -\sum_{k'=4}^{K} c_{k'}(t)\left(\frac{\partial V_{k'(i',j')}}{\partial \mathbf{q}_{k(i,j)}}\delta_{i,1}\delta_{j,i'} + \frac{\partial V_{k'(i',j')}}{\partial \mathbf{q}_{k(i,j)}}\delta_{i,1}\delta_{j,j'}\right) \\
&= -\sum_{k'=4}^{K} c_{k'}(t)\frac{\partial V_{k'}}{\partial \mathbf{q}_{k(i,j)}}\delta_{i,1}\alpha^2_{jk'} \\
&= -\sum_{k'=4}^{K} c_{k'}(t)\frac{\partial V_{k'}}{\partial \mathbf{q}_{k(i,j)}}\delta_{i,1}\alpha^2_{jk'} \\
&= -\sum_{k'=4}^{K} c_{k'}(t)\frac{\partial V_{\mathrm{eff}}\left(\zeta_{a'}, q_{k(i,j)}\right)}{\partial \mathbf{q}_{k(i,j)}}\delta_{i,1}\alpha^2_{jk'} \\
&= -\sum_{d=0}^{N_e-2} c_{|\mathbf{M}^{k,e}_{N_e}(j-1-N_{nuc},d)|}(t)\frac{\partial V_{\mathrm{eff}}(\zeta_{\mathbf{M}^{m,e}_{N_e}(j-1-N_{nuc},d)}, q_{k(i,j)})}{\partial \mathbf{q}_{k(i,j)}}\delta_{i,1}
\end{aligned}
\tag{C.14}
$$

The compacted equations of motion in Eq. (3.25) are given below

$$
\begin{aligned}
\frac{d\mathbf{q}_{k(i,j)}}{dt} &= \frac{1}{m_i}\mathbf{J}_i - \frac{1}{m_j}\mathbf{J}_j - \frac{Q_i}{m_i}\mathbf{A}\left(\mathbf{r}_i,t\right) + \frac{Q_j}{m_j}\mathbf{A}\left(\mathbf{r}_j,t\right) \\
\frac{d\langle\mathbf{q}\rangle}{dt} &= \frac{1}{M}\langle\boldsymbol{\rho}\rangle - \sum_{i=1}^{N}\frac{Q_i}{M}\mathbf{A}\left(\mathbf{r}_i,t\right) \\
\frac{d\boldsymbol{\rho}_{k(i,j)}}{dt} &= [1-c_k(t)]\frac{U_k\mathbf{q}_k}{q_k^3} - \sum_{d=0}^{N_e-2} c_{|\mathbf{M}^{k,e}_{N_e}(j-1-N_{nuc},d)|}(t)\frac{\partial V_{\mathrm{eff}}(\zeta_{\mathbf{M}^{m,e}_{N_e}(j-1-N_{nuc},d)}, q_{k(i,j)})}{\partial \mathbf{q}_{k(i,j)}}\delta_{i,1} \\
&\quad + \frac{Q_i m_j}{m_i M}\mathbf{p}_i\cdot\frac{\partial\mathbf{A}\left(\mathbf{r}_i,t\right)}{\partial\mathbf{r}_i} - \frac{Q_j m_i}{m_j M}\mathbf{p}_j\cdot\frac{\partial\mathbf{A}\left(\mathbf{r}_j,t\right)}{\partial\mathbf{r}_j} \\
\frac{d\langle\boldsymbol{\rho}\rangle}{dt} &= \sum_{i=1}^{N}\frac{Q_i}{m_i}\mathbf{p}_i\cdot\frac{\partial\mathbf{A}\left(\mathbf{r}_i,t\right)}{\partial\mathbf{r}_i},
\end{aligned}
\tag{C.15}
$$

where $\mathbf{r}_i$ and $\mathbf{p}_i$ are found from Eqs. (C.3) and (C.2) combined with Eqs. (2.15), (3.5) and the relation $\mathbf{p}_i = \tilde{\mathbf{p}}_i - Q_i\mathbf{A}\left(\mathbf{r}_i,t\right)$. The derivative $\mathbf{p}_i\cdot\frac{\partial\mathbf{A}\left(\mathbf{r}_i,t\right)}{\partial\mathbf{r}_i}$ is given in Eq. (D.10).

Appendix D

Derivatives of the field terms

The vector potential that we employ is given in Eq. (3.41). For simplicity, we make the following substitution in Eq. (3.41)

$$\tau = \sqrt{2\ln(2)}\tau' \tag{D.1}$$

$$\mathbf{A}(\mathrm{y},\mathrm{t}) = -\frac{\mathrm{E}_0}{\omega}\exp\left[-2\ln(2)\left(\frac{\mathrm{ct}-\mathrm{y}}{\mathrm{c}\tau}\right)^2\right]\sin(\omega\mathrm{t}-\mathrm{ky})\hat{\mathbf{z}} = -\frac{\mathrm{E}_0}{\omega}\exp\left[-\left(\frac{\mathrm{ct}-\mathrm{y}}{\mathrm{c}\tau'}\right)^2\right]\sin(\omega\mathrm{t}-\mathrm{ky})\hat{\mathbf{z}} \tag{D.2}$$

For compactness, we also introduce the variables $\mathcal{K}(\mathrm{y},\mathrm{t}) = \mathrm{E}_0\exp\left[-\mathcal{C}(\mathrm{y},\mathrm{t})^2\right]$, $\mathcal{C}(\mathrm{y},\mathrm{t}) = \frac{\mathrm{ct}-\mathrm{y}}{\mathrm{c}\tau'}$ and $\phi(\mathrm{y},\mathrm{t}) = \omega\mathrm{t}-\mathrm{ky}$ and write the vector potential as

$$\mathbf{A}(\mathrm{y},\mathrm{t}) = -\frac{\mathcal{K}(\mathrm{y},\mathrm{t})}{\omega}\sin(\phi(\mathrm{y},\mathrm{t}))\hat{\mathbf{z}} \tag{D.3}$$

These variables have the following derivatives

$$\begin{aligned}\frac{\partial\mathcal{K}(\mathrm{y},\mathrm{t})}{\partial\mathrm{t}} &= -2\mathcal{C}(\mathrm{y},\mathrm{t})\frac{\partial\mathcal{C}(\mathrm{y},\mathrm{t})}{\partial\mathrm{t}}\mathcal{K}(\mathrm{y},\mathrm{t}) = -\frac{2\mathcal{C}(\mathrm{y},\mathrm{t})}{\tau'}\mathcal{K}(\mathrm{y},\mathrm{t})\\ \frac{\partial\mathcal{K}(\mathrm{y},\mathrm{t})}{\partial\mathrm{y}} &= -2\mathcal{C}(\mathrm{y},\mathrm{t})\frac{\partial\mathcal{C}(\mathrm{y},\mathrm{t})}{\partial\mathrm{y}}\mathcal{K}(\mathrm{y},\mathrm{t}) = \frac{2\mathcal{C}(\mathrm{y},\mathrm{t})}{\mathrm{c}\tau'}\mathcal{K}(\mathrm{y},\mathrm{t})\end{aligned} \tag{D.4}$$

with $\frac{\partial\mathcal{C}(\mathrm{y},\mathrm{t})}{\partial\mathrm{t}} = \frac{1}{\tau'}$ and $\frac{\partial\mathcal{C}(\mathrm{y},\mathrm{t})}{\partial\mathrm{y}} = -\frac{1}{\mathrm{c}\tau'}$. Note that the derivatives of $\phi(y,t)$ are given by $\frac{\partial\phi(\mathrm{y},\mathrm{t})}{\partial\mathrm{t}} = \omega$ and $\frac{\partial\phi(\mathrm{y},\mathrm{t})}{\partial\mathrm{y}} = -\mathrm{k}$.

D.1 Derivatives of the vector potential

D.1.1 Derivative with respect to time

$$\begin{aligned}\frac{\partial \mathbf{A}(\mathrm{y},\mathrm{t})}{\partial \mathrm{t}} &= -\frac{1}{\omega}\left[\frac{\partial \mathcal{K}(\mathrm{y},\mathrm{t})}{\partial \mathrm{t}}\sin(\phi(\mathrm{y},\mathrm{t})) + \mathcal{K}(\mathrm{y},\mathrm{t})\cos(\phi(\mathrm{y},\mathrm{t}))\frac{\partial \phi(\mathrm{y},\mathrm{t})}{\partial \mathrm{t}}\right]\hat{\mathbf{z}} \\ &= -\frac{1}{\omega}\left[-\frac{2\mathcal{C}(\mathrm{y},\mathrm{t})}{\tau'}\mathcal{K}(\mathrm{y},\mathrm{t})\sin(\phi(\mathrm{y},\mathrm{t})) + \mathcal{K}(\mathrm{y},\mathrm{t})\cos(\phi(\mathrm{y},\mathrm{t}))\omega\right]\hat{\mathbf{z}} \\ &= \mathcal{K}(\mathrm{y},\mathrm{t})\left[\frac{2\mathcal{C}(\mathrm{y},\mathrm{t})}{\omega\tau'}\sin(\phi(\mathrm{y},\mathrm{t})) - \cos(\phi(\mathrm{y},\mathrm{t}))\right]\hat{\mathbf{z}}\end{aligned} \tag{D.5}$$

D.1.2 Derivative with respect to position

$$\begin{aligned}\frac{\partial \mathbf{A}(\mathrm{y},\mathrm{t})}{\partial \mathrm{y}} &= -\frac{1}{\omega}\left[\frac{\partial \mathcal{K}(\mathrm{y},\mathrm{t})}{\partial \mathrm{y}}\sin(\phi(\mathrm{y},\mathrm{t})) + \mathcal{K}(\mathrm{y},\mathrm{t})\cos(\phi(\mathrm{y},\mathrm{t}))\frac{\partial \phi(\mathrm{y},\mathrm{t})}{\partial \mathrm{y}}\right]\hat{\mathbf{z}} \\ &= -\frac{1}{\omega}\left[\frac{2\mathcal{C}(\mathrm{y},\mathrm{t})}{\mathrm{c}\tau'}\mathcal{K}(\mathrm{y},\mathrm{t})\sin(\phi(\mathrm{y},\mathrm{t})) - \mathcal{K}(\mathrm{y},\mathrm{t})\cos(\phi(\mathrm{y},\mathrm{t}))\mathrm{k}\right]\hat{\mathbf{z}} \\ &= \frac{1}{\omega}\mathcal{K}(\mathrm{y},\mathrm{t})\left[-\frac{2\mathcal{C}(\mathrm{y},\mathrm{t})}{\mathrm{c}\tau'}\sin(\phi(\mathrm{y},\mathrm{t})) + \cos(\phi(\mathrm{y},\mathrm{t}))\mathrm{k}\right]\hat{\mathbf{z}}\end{aligned} \tag{D.6}$$

D.1.3 Derivative with respect to position vector

The derivative $\dfrac{\partial \mathbf{A}(\mathbf{r}_\mathrm{i},\mathrm{t})}{\partial \mathbf{r}_\mathrm{i}}$ appearing in Eqs. (3.27) and Eq. (3.28) is given by

$$\frac{\partial \mathbf{A}(\mathbf{r}_\mathrm{i},\mathrm{t})}{\partial \mathbf{r}_\mathrm{i}} = \begin{pmatrix} \dfrac{\partial \mathrm{A_x}(\mathbf{r}_\mathrm{i},\mathrm{t})}{\partial \mathrm{x_i}} & \dfrac{\partial \mathrm{A_x}(\mathbf{r}_\mathrm{i},\mathrm{t})}{\partial \mathrm{y_i}} & \dfrac{\partial \mathrm{A_x}(\mathbf{r}_\mathrm{i},\mathrm{t})}{\partial \mathrm{z_i}} \\ \dfrac{\partial \mathrm{A_y}(\mathbf{r}_\mathrm{i},\mathrm{t})}{\partial \mathrm{x_i}} & \dfrac{\partial \mathrm{A_y}(\mathbf{r}_\mathrm{i},\mathrm{t})}{\partial \mathrm{y_i}} & \dfrac{\partial \mathrm{A_y}(\mathbf{r}_\mathrm{i},\mathrm{t})}{\partial \mathrm{z_i}} \\ \dfrac{\partial \mathrm{A_z}(\mathbf{r}_\mathrm{i},\mathrm{t})}{\partial \mathrm{x_i}} & \dfrac{\partial \mathrm{A_z}(\mathbf{r}_\mathrm{i},\mathrm{t})}{\partial \mathrm{y_i}} & \dfrac{\partial \mathrm{A_z}(\mathbf{r}_\mathrm{i},\mathrm{t})}{\partial \mathrm{z_i}} \end{pmatrix} \tag{D.7}$$

Assuming that the vector potential is given by Eq. (3.41), i.e. it only depends on y, Eq. (D.7) reduces to

$$\frac{\partial \mathbf{A}(\mathbf{r}_\mathrm{i},\mathrm{t})}{\partial \mathbf{r}_\mathrm{i}} = \begin{pmatrix} 0 & \dfrac{\partial \mathrm{A_x}(\mathbf{r}_\mathrm{i},\mathrm{t})}{\partial \mathrm{y_i}} & 0 \\ 0 & \dfrac{\partial \mathrm{A_y}(\mathbf{r}_\mathrm{i},\mathrm{t})}{\partial \mathrm{y_i}} & 0 \\ 0 & \dfrac{\partial \mathrm{A_z}(\mathbf{r}_\mathrm{i},\mathrm{t})}{\partial \mathrm{y_i}} & 0 \end{pmatrix} \tag{D.8}$$

and further reduces to

$$\frac{\partial \mathbf{A}(\mathbf{r}_i,t)}{\partial \mathbf{r}_i} = \begin{pmatrix} 0 & 0 & 0 \\ 0 & 0 & 0 \\ 0 & \dfrac{\partial A_z(\mathbf{r}_i,t)}{\partial y_i} & 0 \end{pmatrix} \tag{D.9}$$

since the vector potential considered in this thesis is along the z axis. We calculate the term $\mathbf{p}_i \cdot \dfrac{\partial \mathbf{A}(\mathbf{r}_i,t)}{\partial \mathbf{r}_i}$, arising in Eq. (3.25), as follows

$$\mathbf{p}_i \cdot \frac{\partial \mathbf{A}(\mathbf{r}_i,t)}{\partial \mathbf{r}_i} = (p_{x,i}, p_{y,i}, p_{z,i}) \cdot \begin{pmatrix} 0 & 0 & 0 \\ 0 & 0 & 0 \\ 0 & \dfrac{\partial A_z(\mathbf{r}_i,t)}{\partial y_i} & 0 \end{pmatrix} = \left(0, p_{z,i}\frac{\partial A_z(\mathbf{r}_i,t)}{\partial y_i}, 0\right) \tag{D.10}$$

where $p_{z,i}$ is the z component of $\mathbf{p}_i$, y_i is the y component of $\mathbf{r}_i$ and $\dfrac{\partial A_z(\mathbf{r}_i,t)}{\partial y_i}$ is the derivative of the z component of the vector potential with respect to the y component of particle i.

D.2 Derivatives of the electric field

The electric field $\mathbf{E}(y,t) = -\frac{\partial \mathbf{A}(y,t)}{\partial t}$, see Eq. (D.1.1). In what follows, we calculate the derivative with respect to time and position in order to calculate the term

$$-Q_j \mathbf{r}_j \cdot \left(\frac{\partial \mathbf{E}\left(\mathbf{r}_j,t\right)}{\partial \mathbf{r}_j} \cdot \dot{\mathbf{r}}_j \right) - Q_j \mathbf{r}_j \cdot \frac{\partial \mathbf{E}\left(\mathbf{r}_j,t\right)}{\partial t} = -Q_j \mathbf{r}_j \cdot \dot{\mathbf{E}}\left(\mathbf{r}_j,t\right) \tag{D.11}$$

in Eq. (3.20). Note that we take $\dot{\mathbf{r}}_j = \frac{\mathbf{p}_j}{m_j}$.

D.2.1 Derivative with respect to time

$$\begin{aligned}
&\frac{\partial \mathbf{E}(y,t)}{\partial t} = -\left(\frac{\partial \mathcal{K}(y,t)}{\partial t} \left[\frac{2\mathcal{C}(y,t)}{\omega\tau'} \sin(\phi(y,t)) - \cos(\phi(y,t)) \right] \right. \\
&\left. + \mathcal{K}(y,t) \frac{\partial}{\partial t} \left[\frac{2\mathcal{C}(y,t)}{\omega\tau'} \sin(\phi(y,t)) - \cos(\phi(y,t)) \right] \right) \hat{\mathbf{z}} \\
&= -\left(-\frac{2\mathcal{C}(y,t)}{\tau'} \mathcal{K}(y,t) \left[\frac{2\mathcal{C}(y,t)}{\omega\tau'} \sin(\phi(y,t)) - \cos(\phi(y,t)) \right] \right. \\
&\left. + \mathcal{K}(y,t) \left\{ \frac{2}{\omega\tau'} \left[\frac{\partial \mathcal{C}(y,t)}{\partial t} \sin(\phi(y,t)) + \mathcal{C}(y,t) \cos(\phi(y,t)) \frac{\partial \phi(y,t)}{\partial t} \right] + \sin(\phi(y,t)) \frac{\partial \phi(y,t)}{\partial t} \right\} \right) \hat{\mathbf{z}} \\
&= -\mathcal{K}(y,t) \left(-\frac{4\mathcal{C}(y,t)^2}{\omega\tau'^2} \sin(\phi(y,t)) + \frac{2\mathcal{C}(y,t)}{\tau'} \cos(\phi(y,t)) \right. \\
&\left. + \frac{2}{\omega\tau'^2} \sin(\phi(y,t)) + \mathcal{C}(y,t) \cos(\phi(y,t)) \frac{2}{\tau'} + \sin(\phi(y,t)) \omega \right) \hat{\mathbf{z}} \\
&= \omega \mathcal{K}(y,t) \left(\frac{4\mathcal{C}(y,t)^2}{\omega^2\tau'^2} \sin(\phi(y,t)) - \frac{2\mathcal{C}(y,t)}{\omega\tau'} \cos(\phi(y,t)) \right. \\
&\left. - \frac{2}{\omega^2\tau'^2} \sin(\phi(y,t)) - \mathcal{C}(y,t) \cos(\phi(y,t)) \frac{2}{\omega\tau'} - \sin(\phi(y,t)) \right) \hat{\mathbf{z}} \\
&= \omega \mathcal{K}(y,t) \left(\frac{4\mathcal{C}(y,t)^2}{\omega^2\tau'^2} \sin(\phi(y,t)) - \frac{4\mathcal{C}(y,t)}{\omega\tau'} \cos(\phi(y,t)) \right. \\
&\left. - \frac{2}{\omega^2\tau'^2} \sin(\phi(y,t)) - \sin(\phi(y,t)) \right) \hat{\mathbf{z}} \\
&= \omega \mathcal{K}(y,t) \left(\frac{2\mathcal{C}(y,t)}{\omega\tau'} \left[\frac{2\mathcal{C}(y,t)}{\omega\tau'} \sin(\phi(y,t)) - 2\cos(\phi(y,t)) \right] - \frac{2}{\omega^2\tau'^2} \sin(\phi(y,t)) - \sin(\phi(y,t)) \right) \hat{\mathbf{z}}
\end{aligned} \tag{D.12}$$

D.2.2 Derivative with respect to position

$$
\begin{aligned}
&\frac{\partial \mathbf{E}(y,t)}{\partial y} = -\left(\frac{\partial \mathcal{K}(y,t)}{\partial y}\left[\frac{2\mathcal{C}(y,t)}{\omega\tau'}\sin(\phi(y,t)) - \cos(\phi(y,t))\right]\right.\\
&\left. + \mathcal{K}(y,t)\frac{\partial}{\partial y}\left[\frac{2\mathcal{C}(y,t)}{\omega\tau'}\sin(\phi(y,t)) - \cos(\phi(y,t))\right]\right)\hat{\mathbf{z}}\\
&= -\left(\frac{2\mathcal{C}(y,t)}{c\tau'}\mathcal{K}(y,t)\left[\frac{2\mathcal{C}(y,t)}{\omega\tau'}\sin(\phi(y,t)) - \cos(\phi(y,t))\right]\right.\\
&\left. + \mathcal{K}(y,t)\left\{\frac{2}{\omega\tau'}\left[\frac{\partial \mathcal{C}(y,t)}{\partial y}\sin(\phi(y,t)) + \mathcal{C}(y,t)\cos(\phi(y,t))\frac{\partial\phi(y,t)}{\partial y}\right] + \sin(\phi(y,t))\frac{\partial\phi(y,t)}{\partial y}\right\}\right)\hat{\mathbf{z}}\\
&= -\mathcal{K}(y,t)\left(\frac{4\mathcal{C}(y,t)^2}{c\omega\tau'^2}\sin(\phi(y,t)) - \frac{2\mathcal{C}(y,t)}{c\tau'}\cos(\phi(y,t))\right.\\
&\left. - \frac{2}{c\omega\tau'^2}\sin(\phi(y,t)) - k\mathcal{C}(y,t)\cos(\phi(y,t))\frac{2}{\omega\tau'} - \sin(\phi(y,t))k\right)\hat{\mathbf{z}}\\
&= k\mathcal{K}(y,t)\left(-\frac{4\mathcal{C}(y,t)^2}{\omega^2\tau'^2}\sin(\phi(y,t)) + \frac{2\mathcal{C}(y,t)}{\omega\tau'}\cos(\phi(y,t))\right.\\
&\left. + \frac{2}{\omega^2\tau'^2}\sin(\phi(y,t)) + \mathcal{C}(y,t)\cos(\phi(y,t))\frac{2}{\omega\tau'} + \sin(\phi(y,t))\right)\hat{\mathbf{z}}\\
&= k\mathcal{K}(y,t)\left(-\frac{4\mathcal{C}(y,t)^2}{\omega^2\tau'^2}\sin(\phi(y,t)) + \frac{4\mathcal{C}(y,t)}{\omega\tau'}\cos(\phi(y,t))\right.\\
&\left. + \frac{2}{\omega^2\tau'^2}\sin(\phi(y,t)) + \sin(\phi(y,t))\right)\hat{\mathbf{z}}\\
&= k\mathcal{K}(y,t)\left(\frac{2\mathcal{C}(y,t)}{\omega\tau'}\left[-\frac{2\mathcal{C}(y,t)}{\omega\tau'}\sin(\phi(y,t)) + 2\cos(\phi(y,t))\right] + \frac{2}{\omega^2\tau'^2}\sin(\phi(y,t)) + \sin(\phi(y,t))\right)\hat{\mathbf{z}}
\end{aligned}
\tag{D.13}
$$

D.2.3 Derivative with respect to position vector

The calculation of $\frac{\partial \mathbf{E}(\mathbf{r}_j,t)}{\partial \mathbf{r}_j}\cdot\frac{\mathbf{p}_j}{m_j}$ from Eq. (3.20) follows a similar procedure as in Eq. (D.7). The result is given below

$$
\frac{\partial \mathbf{E}\left(\mathbf{r}_j,t\right)}{\partial \mathbf{r}_j}\cdot\frac{\mathbf{p}_j}{m_j} = \frac{1}{m_j}\begin{pmatrix} 0 & 0 & 0\\ 0 & 0 & 0\\ 0 & \frac{\partial E_z\left(\mathbf{r}_j,t\right)}{\partial y_i} & 0\end{pmatrix}\cdot\begin{pmatrix} p_{x,j}\\ p_{y,j}\\ p_{z,j}\end{pmatrix} = \left(0,0,\frac{p_{y,j}}{m_j}\frac{\partial E_z\left(\mathbf{r}_j,t\right)}{\partial y_j}\right)
\tag{D.14}
$$

where $p_{y,j}$ is the y component of $\mathbf{p}_j$, y_j is the y component of $\mathbf{r}_j$ and $\frac{\partial E_z\left(\mathbf{r}_j,t\right)}{\partial y_j}$ is the derivative of the z component of the electric field with respect to the y component

of particle j.

Appendix E

Derivatives of the Heisenberg potential terms

In this appendix, we calculate the derivatives of the Heisenberg potential, $V_{H,i}$ given by

$$V_{H,i} = \frac{\xi^2}{4\alpha\mu q_{i-1}^2} \exp\left\{\alpha\left[1-\left(\frac{q_{i-1}p_{i,1}}{\xi}\right)^4\right]\right\}. \tag{E.1}$$

with

$$\mathbf{p}_{i,1} = \frac{m_i\mathbf{p}_1 - m_1\mathbf{p}_i}{m_1+m_i}, \tag{E.2}$$

see Sec. 3.2.3. In equation Eq. (3.40) we need to calculate the derivative of $V_{H,i}$ with respect to $\boldsymbol{\rho}_k$. This is given below

$$\begin{aligned}
\frac{\partial V_{H,i}}{\partial \boldsymbol{\rho}_k} &= \frac{\partial V_{H,i}}{\partial p_{i,1}}\frac{\partial p_{i,1}}{\partial \boldsymbol{\rho}_k} \\
&= \frac{\partial V_{H,i}}{\partial p_{i,1}}\frac{\partial p_{i,1}}{\partial \mathbf{p}_{i,1}}\frac{\partial \mathbf{p}_{i,1}}{\partial \boldsymbol{\rho}_k} \\
&= \frac{\partial V_{H,i}}{\partial p_{i,1}}\frac{\partial (\mathbf{p}_{i,1}\cdot\mathbf{p}_{i,1})^{1/2}}{\partial \mathbf{p}_{i,1}}\frac{\partial \mathbf{p}_{i,1}}{\partial \boldsymbol{\rho}_k} \\
&= \frac{\partial V_{H,i}}{\partial p_{i,1}}\frac{\mathbf{p}_{i,1}}{p_{i,1}}\frac{\partial \mathbf{p}_{i,1}}{\partial \boldsymbol{\rho}_k}
\end{aligned} \tag{E.3}$$

with

$$\begin{aligned}\frac{\partial \mathbf{p}_{i,1}}{\partial \boldsymbol{\rho}_k} &= \frac{m_i \frac{\partial \mathbf{p}_1}{\boldsymbol{\rho}_k} - m_1 \frac{\partial \mathbf{p}_i}{\boldsymbol{\rho}_k}}{m_1 + m_i} \\ &= \frac{m_i \frac{\partial \mathbf{p}_1}{\partial \tilde{\mathbf{p}}_1}\frac{\partial \tilde{\mathbf{p}}_1}{\partial \boldsymbol{\rho}_k} - m_1 \frac{\partial \mathbf{p}_i}{\partial \tilde{\mathbf{p}}_i}\frac{\partial \tilde{\mathbf{p}}_i}{\partial \boldsymbol{\rho}_k}}{m_1 + m_i} \\ &= \frac{m_i \frac{\partial \tilde{\mathbf{p}}_1}{\partial \boldsymbol{\rho}_k} - m_1 \frac{\partial \tilde{\mathbf{p}}_i}{\partial \boldsymbol{\rho}_k}}{m_1 + m_i} \\ &= \frac{m_i \alpha_{1k} - m_1 \alpha_{ik}}{m_1 + m_i}\end{aligned} \tag{E.4}$$

where $\frac{\partial \mathbf{p}_1}{\partial \tilde{\mathbf{p}}_1} = 1$ from Eq. (3.2), $\frac{\partial \tilde{\mathbf{p}}_i}{\partial \boldsymbol{\rho}_k} = \alpha_{ik}$ from Eq. (3.5) and

$$\begin{aligned}\frac{\partial V_{H,i}}{\partial p_{i,1}} &= -4\alpha \left(\frac{q_{i-1}}{\xi}\right)^4 p_{i,1}^3 \frac{\xi^2}{4\alpha\mu q_{i-1}^2} \exp\left\{\alpha\left[1 - \left(\frac{q_{i-1}p_{i,1}}{\xi}\right)^4\right]\right\} \\ &= -\frac{q_{i-1}^2 p_{i,1}^3}{\mu\xi^2} \exp\left\{\alpha\left[1 - \left(\frac{q_{i-1}p_{i,1}}{\xi}\right)^4\right]\right\}\end{aligned} \tag{E.5}$$

In equation Eq. (3.40) we also need to calculate the derivative of $V_{H,i}$ with respect to $\mathbf{q}_k$ and $\langle \mathbf{q} \rangle$. These are given below

$$\begin{aligned}\frac{\partial V_{H,i}}{\partial \mathbf{q}_k} &= \frac{\partial V_{H,i}}{\partial q_{i-1}}\frac{\partial q_{i-1}}{\partial \mathbf{q}_k} + \frac{\partial V_{H,i}}{\partial p_{i,1}}\frac{\partial p_{i,1}}{\partial \mathbf{q}_k} \\ &= \frac{\partial V_{H,i}}{\partial q_{i-1}}\delta_{i-1,k}\frac{\partial (\mathbf{q}_{i-1}\cdot\mathbf{q}_{i-1})^{1/2}}{\partial \mathbf{q}_k} + \frac{\partial V_{H,i}}{\partial p_{i,1}}\frac{\partial (\mathbf{p}_{i,1}\cdot\mathbf{p}_{i,1})^{1/2}}{\partial \mathbf{q}_k} \\ &= \frac{\partial V_{H,i}}{\partial q_{i-1}}\delta_{i-1,k}\frac{\mathbf{q}_{i-1}}{q_{i-1}} + \frac{\partial V_{H,i}}{\partial p_{i,1}}\frac{\mathbf{p}_{i,1}}{p_{i,1}}\frac{\partial \mathbf{p}_{i,1}}{\partial \mathbf{q}_k}\end{aligned} \tag{E.6}$$

$$\begin{aligned}\frac{\partial V_{H,i}}{\partial \langle \mathbf{q} \rangle} &= \frac{\partial V_{H,i}}{\partial q_{i-1}}\frac{\partial q_{i-1}}{\partial \langle \mathbf{q} \rangle} + \frac{\partial V_{H,i}}{\partial p_{i,1}}\frac{\partial p_{i,1}}{\partial \langle \mathbf{q} \rangle} \\ &= \frac{\partial V_{H,i}}{\partial q_{i-1}}\frac{\partial (\mathbf{q}_{i-1}\cdot\mathbf{q}_{i-1})^{1/2}}{\partial \langle \mathbf{q} \rangle} + \frac{\partial V_{H,i}}{\partial p_{i,1}}\frac{\partial (\mathbf{p}_{i,1}\cdot\mathbf{p}_{i,1})^{1/2}}{\partial \langle \mathbf{q} \rangle} \\ &= \frac{\partial V_{H,i}}{\partial p_{i,1}}\frac{\mathbf{p}_{i,1}}{p_{i,1}}\frac{\partial \mathbf{p}_{i,1}}{\partial \langle \mathbf{q} \rangle}\end{aligned} \tag{E.7}$$

with

$$\begin{aligned}\frac{\partial \mathbf{p}_{i,1}}{\partial \mathbf{q}_k} &= \frac{m_i \frac{\partial \mathbf{p}_1}{\mathbf{q}_k} - m_1 \frac{\partial \mathbf{p}_i}{\mathbf{q}_k}}{m_1 + m_i} \\ &= \frac{m_i \frac{\partial [\tilde{\mathbf{p}}_1 - Q_1 \mathbf{A}(\mathbf{r}_1,t)]}{\mathbf{q}_k} - m_1 \frac{\partial [\tilde{\mathbf{p}}_i - Q_i \mathbf{A}(\mathbf{r}_i,t)]}{\mathbf{q}_k}}{m_1 + m_i} \\ &= \frac{-m_i Q_1 \frac{\partial \mathbf{A}(\mathbf{r}_1,t)}{\mathbf{q}_k} + m_1 Q_i \frac{\partial \mathbf{A}(\mathbf{r}_i,t)}{\mathbf{q}_k}}{m_1 + m_i}\end{aligned} \tag{E.8}$$

and

$$\begin{aligned}\frac{\partial \mathbf{p}_{i,1}}{\partial \langle \mathbf{q} \rangle} &= \frac{m_i \frac{\partial \mathbf{p}_1}{\langle \mathbf{q} \rangle} - m_1 \frac{\partial \mathbf{p}_i}{\langle \mathbf{q} \rangle}}{m_1 + m_i} \\ &= \frac{m_i \frac{\partial [\tilde{\mathbf{p}}_1 - Q_1 \mathbf{A}(\mathbf{r}_1,t)]}{\langle \mathbf{q} \rangle} - m_1 \frac{\partial [\tilde{\mathbf{p}}_i - Q_i \mathbf{A}(\mathbf{r}_i,t)]}{\langle \mathbf{q} \rangle}}{m_1 + m_i} \\ &= \frac{-m_i Q_1 \frac{\partial \mathbf{A}(\mathbf{r}_1,t)}{\langle \mathbf{q} \rangle} + m_1 Q_i \frac{\partial \mathbf{A}(\mathbf{r}_i,t)}{\langle \mathbf{q} \rangle}}{m_1 + m_i}\end{aligned} \tag{E.9}$$

where $\mathbf{p}_i = \tilde{\mathbf{p}}_i - Q_i \mathbf{A}(\mathbf{r}_i, t)$ from Eq. (3.2) and $\frac{\partial \mathbf{A}(\mathbf{r}_i,t)}{\mathbf{q}_k}$ and $\frac{\partial \mathbf{A}(\mathbf{r}_i,t)}{\langle \mathbf{q} \rangle}$ are found in Eqs. (3.27) and (3.28). The derivative $\frac{\partial V_{H,i}}{\partial p_{i,1}}$ is given in Eq. (E.5) and $\frac{\partial V_{H,i}}{\partial q_{i-1}}$ is given below

$$\begin{aligned}\frac{\partial V_{H,i}}{\partial q_{i-1}} &= -4\alpha \left(\frac{p_{i,1}}{\xi}\right)^4 q_{i-1}^3 \frac{\xi^2}{4\alpha\mu q_{i-1}^2} \exp\left\{\alpha\left[1 - \left(\frac{q_{i-1}p_{i,1}}{\xi}\right)^4\right]\right\} \\ &\quad - \frac{\xi^2}{2\alpha\mu q_{i-1}^3} \exp\left\{\alpha\left[1 - \left(\frac{q_{i-1}p_{i,1}}{\xi}\right)^4\right]\right\} \\ &= \exp\left\{\alpha\left[1 - \left(\frac{q_{i-1}p_{i,1}}{\xi}\right)^4\right]\right\}\left[-\frac{q_{i-1}p_{i,1}^4}{\mu\xi^2} - \frac{\xi^2}{2\alpha\mu q_{i-1}^3}\right].\end{aligned} \tag{E.10}$$

Appendix F

Using Cramers Rule to solve a set of linear equations

The time derivative of the energies of the electrons from Eq. (3.21) is

$$\dot{\mathcal{E}}_j(t) = f_j + \sum_{\substack{i=2 \\ i\neq j}}^{N} c_{i,j}(t) \frac{\partial V_{eff}(\zeta_i, |\mathbf{r}_1 - \mathbf{r}_j|)}{\partial \zeta_i} \dot{\zeta}_i, \tag{F.1}$$

with the time derivative of ζ_j from Eq. (3.22) given by

$$\dot{\zeta}_j = \begin{cases} 0 & \mathcal{E}_j(t) \leq \mathcal{E}_{1s} \\ (Q_1/\mathcal{E}_{1s})\,\dot{\mathcal{E}}_j(t) & \mathcal{E}_{1s} < \mathcal{E}_j(t) < 0. \\ 0 & \mathcal{E}_j(t) \geq 0. \end{cases} \tag{F.2}$$

In order to calculate $\dot{\zeta}_j(t)$, we first substitute Eq. (F.1) into Eq. (F.2) to obtain

$$\begin{aligned} \dot{\zeta}_j(t) &= (1-\mathcal{X})\,(Q_1/\mathcal{E}_{1s})\,f_j + (1-\mathcal{X})(Q_1/\mathcal{E}_{1s}) \sum_{\substack{i=2 \\ i\neq j}}^{N} c_{i,j}(t) \frac{\partial V_{eff}(\zeta_i, |\mathbf{r}_1 - \mathbf{r}_j|)}{\partial \zeta_i} \dot{\zeta}_i \\ &= f'_j + \sum_{\substack{i=2 \\ i\neq j}}^{N} g_{j,i} \dot{\zeta}_i, \end{aligned} \tag{F.3}$$

where $f'_j = (1-\mathcal{X})\,(Q_1/\mathcal{E}_{1s})\,f_j$ and $g_{j,i} = (1-\mathcal{X})(Q_1/\mathcal{E}_{1s})c_{i,j}(t)\frac{\partial V_{eff}(\zeta_i, |\mathbf{r}_1 - \mathbf{r}_j|)}{\partial \zeta_i}$. The variable $\mathcal{X}$ is zero if $\mathcal{E}_{1s} < \mathcal{E}_j(t) < 0$ and one otherwise, in accord with Eq. (F.2).

For three electrons, Eq. (F.3) takes the following form.

$$\begin{pmatrix} \dot{\zeta}_2 \\ \dot{\zeta}_3 \\ \dot{\zeta}_4 \end{pmatrix} = \begin{pmatrix} f'_2 + g_{2,3}\dot{\zeta}_3 + g_{2,4}\dot{\zeta}_4 \\ f'_3 + g_{3,2}\dot{\zeta}_2 + g_{3,4}\dot{\zeta}_4 \\ f'_4 + g_{4,2}\dot{\zeta}_2 + g_{4,3}\dot{\zeta}_3 \end{pmatrix}$$

$$\rightarrow \begin{pmatrix} -f'_2 \\ -f'_3 \\ -f'_4 \end{pmatrix} = \begin{pmatrix} -\dot{\zeta}_2 + g_{2,3}\dot{\zeta}_3 + g_{2,4}\dot{\zeta}_4 \\ g_{3,2}\dot{\zeta}_2 - \dot{\zeta}_3 + g_{3,4}\dot{\zeta}_4 \\ g_{4,2}\dot{\zeta}_2 + g_{4,3}\dot{\zeta}_3 - \dot{\zeta}_4 \end{pmatrix}$$

$$\rightarrow \begin{pmatrix} -f'_2 \\ -f'_3 \\ -f'_4 \end{pmatrix} = \begin{pmatrix} -1 & g_{2,3} & g_{2,4} \\ g_{3,2} & -1 & g_{3,4} \\ g_{4,2} & g_{4,3} & -1 \end{pmatrix} \begin{pmatrix} \dot{\zeta}_2 \\ \dot{\zeta}_3 \\ \dot{\zeta}_4 \end{pmatrix}$$

The general expression for N particles (1 nucleus and N-1 electrons) is given below.

$$\begin{pmatrix} -1 & g_{2,3} & \dots & g_{2,N} \\ g_{3,2} & -1 & \dots & g_{3,N} \\ \vdots & \dots & -1 & \vdots \\ g_{N,2} & g_{N,3} & \dots & -1 \end{pmatrix} \begin{pmatrix} \dot{\zeta}_2 \\ \dot{\zeta}_3 \\ \vdots \\ \dot{\zeta}_N \end{pmatrix} = \begin{pmatrix} -f'_2 \\ -f'_3 \\ \vdots \\ -f'_N \end{pmatrix} \tag{F.4}$$

$$\mathbf{Ax} = \mathbf{b}$$

This can be written in the simple form $\mathbf{Ax} = \mathbf{b}$ with $\mathbf{A}$, $\mathbf{x}$ and $\mathbf{b}$ given in Eq. (F.4). To solve this, we consider Cramers rule which states that the solutions to $\mathbf{x}$ are given by

$$x_i = \frac{\det(\mathbf{A}_i)}{\det(\mathbf{A})}, \tag{F.5}$$

where $\det(\mathbf{A}_i)$ is the matrix obtained by substituting the ith column of $\mathbf{A}$ with $\mathbf{b}$. Finally, we obtain $\dot{\mathcal{E}}_j$ by substituting the solutions for $\dot{\zeta}_j(t)$ back into Eq. (F.1).

Bibliography

[1] M. B. Peters, V. P. Majety, and A. Emmanouilidou, Phys. Rev. A **103**, 043109 (2021).

[2] M. B. Peters, G. P. Katsoulis, and A. Emmanouilidou, Phys. Rev. A **105**, 043102 (2022).

[3] A. Emmanouilidou, M. B. Peters, and G. P. Katsoulis, Phys. Rev. A **107**, L041101 (2023).

[4] G. P. Katsoulis, M. B. Peters, and A. Emmanouilidou, "Nondipole electron momentum offset as a probe of correlated three electron ionization in strongly driven atoms," (2023), arXiv:2210.17394 [physics.atom-ph] .

[5] M. Hentschel, R. Kienberger, C. Spielmann, G. A. Reider, N. Milosevic, T. Brabec, P. Corkum, U. Heinzmann, M. Drescher, and F. Krausz, Nature **414**, 509 (2001).

[6] E. Goulielmakis, M. Schultze, M. Hofstetter, V. S. Yakovlev, J. Gagnon, M. Uiberacker, A. L. Aquila, E. Gullikson, D. T. Attwood, R. Kienberger, *et al.*, Science **320**, 1614 (2008).

[7] H. Mashiko, S. Gilbertson, M. Chini, X. Feng, C. Yun, H. Wang, S. D. Khan, S. Chen, and Z. Chang, Opt. Lett. **34**, 3337 (2009).

[8] M. Nisoli and G. Sansone, Prog. Quantum Electron. **33**, 17 (2009).

[9] L. Gallmann, C. Cirelli, and U. Keller, Annu. Rev. Phys. Chem. **63**, 447 (2012).

[10] F. Calegari, G. Sansone, S. Stagira, C. Vozzi, and M. Nisoli, J. Phys. B: At. Mol. Opt. Phys. **49**, 062001 (2016).

[11] R. Borrego-Varillas, M. Lucchini, and M. Nisoli, Rep. Prog. Phys. **85**, 066401 (2022).

[12] P. B. Corkum, Phys. Rev. Lett. **71**, 1994 (1993).

[13] D. N. Fittinghoff, P. R. Bolton, B. Chang, and K. C. Kulander, Phys. Rev. Lett. **69**, 2642 (1992).

[14] W. Becker and H. Rottke, Contem. Phys. **49**, 199 (2008).

[15] F. Krausz and M. Ivanov, Rev. Mod. Phys. **81**, 163 (2009).

[16] J. S. Parker, B. J. S. Doherty, K. T. Taylor, K. D. Schultz, C. I. Blaga, and L. F. DiMauro, Phys. Rev. Lett. **96**, 133001 (2006).

[17] A. Zielinski, V. P. Majety, and A. Scrinzi, Phys. Rev. A **93**, 023406 (2016).

[18] J. Zhu and A. Scrinzi, Phys. Rev. A **101**, 063407 (2020).

[19] K. Sacha and B. Eckhardt, Phys. Rev. A **64**, 053401 (2001).

[20] P. J. Ho and J. H. Eberly, Phys. Rev. Lett. **97**, 083001 (2006).

[21] J. H. Thiede, B. Eckhardt, D. K. Efimov, J. S. Prauzner-Bechcicki, and J. Zakrzewski, Phys. Rev. A **98**, 031401(R) (2018).

[22] D. K. Efimov, A. Maksymov, M. Ciappina, J. S. Prauzner-Bechcicki, M. Lewenstein, and J. Zakrzewski, Opt. Express **29**, 26526 (2021).

[23] Y. Zhou, Q. Liao, and P. Lu, Opt. Express **18**, 16025 (2010).

[24] Q. Tang, C. Huang, Y. Zhou, and P. Lu, Opt. Express **21**, 21433 (2013).

[25] H. Jiang and F. He, Phys. Rev. A **104**, 023113 (2021).

[26] H. Jiang, D. Efimov, F. He, and J. S. Prauzner-Bechcicki, Phys. Rev. A **105**, 053119 (2022).

[27] R. Moshammer, B. Feuerstein, W. Schmitt, A. Dorn, C. D. Schröter, J. Ullrich, H. Rottke, C. Trump, M. Wittmann, G. Korn, K. Hoffmann, and W. Sandner, Phys. Rev. Lett. **84**, 447 (2000).

[28] A. Rudenko, T. Ergler, K. Zrost, B. Feuerstein, V. L. B. de Jesus, C. D. Schröter, R. Moshammer, and J. Ullrich, J. Phys. B: At. Mol. Opt. Phys. **41**, 081006 (2008).

[29] N. Ekanayake, S. Luo, B. L. Wen, L. E. Howard, S. J. Wells, M. Videtto, C. Mancuso, T. Stanev, Z. Condon, S. LeMar, A. D. Camilo, R. Toth, W. B. Crosby, P. D. Grugan, M. F. Decamp, and B. C. Walker, Phys. Rev. A **86**, 043402 (2012).

[30] O. Herrwerth, A. Rudenko, M. Kremer, V. L. B. de Jesus, B. Fischer, G. Gademann, K. Simeonidis, A. Achtelik, T. Ergler, B. Feuerstein, C. D. Schröter, R. Moshammer, and J. Ullrich, New J. Phys. **10**, 025007 (2008).

[31] K. Zrost, A. Rudenko, T. Ergler, B. Feuerstein, V. L. B. de Jesus, C. D. Schröter, R. Moshammer, and J. Ullrich, J. Phys. B: At. Mol. Opt. Phys. **39**, S371 (2006).

[32] A. Rudenko, K. Zrost, B. Feuerstein, V. L. B. de Jesus, C. D. Schröter, R. Moshammer, and J. Ullrich, Phys. Rev. Lett. **93**, 253001 (2004).

[33] H. Shimada, Y. Nakai, H. Oyama, K. Ando, T. Kambara, A. Hatakeyama, and Y. Yamazaki, Nucl. Instrum. Methods Phys. Res. B **235**, 221 (2005).

[34] R. R. Pandit, V. R. Becker, K. Barrington, J. Thurston, L. Ramunno, and E. Ackad, Phys. Plasmas **25**, 043302 (2018).

[35] R. R. Pandit, Y. Sentoku, V. R. Becker, K. Barrington, J. Thurston, J. Cheatham, L. Ramunno, and E. Ackad, Phys. Plasmas **24**, 073303 (2017).

[36] A. Emmanouilidou, Phys. Rev. A **78**, 023411 (2008).

[37] A. Staudte, C. Ruiz, M. Schöffler, S. Schössler, D. Zeidler, T. Weber, M. Meckel, D. M. Villeneuve, P. B. Corkum, A. Becker, and R. Dörner, Phys. Rev. Lett. **99**, 263002 (2007).

[38] A. Rudenko, V. L. B. de Jesus, T. Ergler, K. Zrost, B. Feuerstein, C. D. Schröter, R. Moshammer, and J. Ullrich, Phys. Rev. Lett. **99**, 263003 (2007).

[39] A. Emmanouilidou, J. S. Parker, L. R. Moore, and K. T. Taylor, New J. Phys. **13**, 043001 (2011).

[40] A. Chen, M. Kübel, B. Bergues, M. F. Kling, and A. Emmanouilidou, Sci. Rep. **7**, 7488 (2017).

[41] G. P. Katsoulis, A. Hadjipittas, B. Bergues, M. F. Kling, and A. Emmanouilidou, Phys. Rev. Lett. **121**, 263203 (2018).

[42] M. Y. Emelin and M. Y. Ryabikin, Phys. Rev. A **89**, 013418 (2014).

[43] C. C. Chirilă, N. J. Kylstra, R. M. Potvliege, and C. J. Joachain, Phys. Rev. A **66**, 063411 (2002).

[44] M. W. Walser, C. H. Keitel, A. Scrinzi, and T. Brabec, Phys. Rev. Lett. **85**, 5082 (2000).

[45] C. H. Keitel and P. L. Knight, Phys. Rev. A **51**, 1420 (1995).

[46] S. Palaniyappan, A. DiChiara, E. Chowdhury, A. Falkowski, G. Ongadi, E. L. Huskins, and B. C. Walker, Phys. Rev. Lett. **94**, 243003 (2005).

[47] H. R. Reiss, Phys. Rev. Lett. **101**, 043002 (2008).

[48] H. R. Reiss, J. Phys. B **47**, 204006 (2014).

[49] A. Emmanouilidou and T. Meltzer, Phys. Rev. A **95**, 033405 (2017).

[50] A. Emmanouilidou, T. Meltzer, and P. B. Corkum, J. Phys. B **50**, 225602 (2017).

[51] A. Emmanouilidou, C. Lazarou, A. Staudte, and U. Eichmann, Phys. Rev. A **85**, 011402(R) (2012).

[52] J. S. Parker, L. R. Moore, D. Dundas, and K. T. Taylor, J. Phys. B: At. Mol. Opt. Phys. **33**, L691 (2000).

[53] G. S. J. Armstrong, D. D. A. Clarke, J. Benda, J. Wragg, A. C. Brown, and H. W. van der Hart, Phys. Rev. A **103**, 053123 (2021).

[54] L.-B. Fu, J. Liu, J. Chen, and S.-G. Chen, Phys. Rev. A **63**, 043416 (2001).

[55] Z.-Q. Yuan, D.-F. Ye, Y.-Q. Gu, J. Liu, and L.-B. Fu, Opt. Express **27**, 3180 (2019).

[56] H. Price, C. Lazarou, and A. Emmanouilidou, Phys. Rev. A **90**, 053419 (2014).

[57] A. Chen, H. Price, A. Staudte, and A. Emmanouilidou, Phys. Rev. A **94**, 043408 (2016).

[58] T. Nubbemeyer, K. Gorling, A. Saenz, U. Eichmann, and W. Sandner, Phys. Rev. Lett. **101**, 233001 (2008).

[59] B. Manschwetus, T. Nubbemeyer, K. Gorling, G. Steinmeyer, U. Eichmann, H. Rottke, and W. Sandner, Phys. Rev. Lett. **102**, 113002 (2009).

[60] W. Zhang, H. Li, X. Gong, P. Lu, Q. Song, Q. Ji, K. Lin, J. Ma, H. Li, F. Sun, J. Qiang, H. Zeng, and J. Wu, Phys. Rev. A **98**, 013419 (2018).

[61] J. McKenna, A. M. Sayler, B. Gaire, N. G. Johnson, K. D. Carnes, B. D. Esry, and I. Ben-Itzhak, Phys. Rev. Lett. **103**, 103004 (2009).

[62] J. McKenna, A. M. Sayler, B. Gaire, N. G. Kling, B. D. Esry, K. D. Carnes, and I. Ben-Itzhak, New J. Phys. **14**, 103029 (2012).

[63] A. M. Sayler, J. McKenna, B. Gaire, N. G. Kling, K. D. Carnes, and I. Ben-Itzhak, Phys. Rev. A **86**, 033425 (2012).

[64] A. Chen, H. Price, A. Staudte, and A. Emmanouilidou, Phys. Rev. A **94**, 043408 (2016).

[65] A. Chen, M. F. Kling, and A. Emmanouilidou, Phys. Rev. A **96**, 033404 (2017).

[66] S. Larimian, C. Lemell, V. Stummer, J. W. Geng, S. Roither, D. Kartashov, L. Zhang, M. X. Wang, Q. Gong, L. Y. Peng, S. Yoshida, J. Burgdörfer, A. Baltuška, M. Kitzler, and X. Xie, Phys. Rev. A **96**, 021403(R) (2017).

[67] G. P. Katsoulis, R. Sarkar, and A. Emmanouilidou, Phys. Rev. A **101**, 033403 (2020).

[68] A. Vilà, J. Zhu, A. Scrinzi, and A. Emmanouilidou, J. Phys. B: At. Mol. Opt. Phys **51**, 065602 (2018).

[69] W. Zhang, X. Gong, H. Li, P. Lu, F. Sun, Q. Ji, K. Lin, J. Ma, H. Li, J. Qiang, F. He, and J. Wu, Nat. Commun. **10**, 757 (2019).

[70] P. Palmieri, C. Puzzarini, V. Aquilanti, G. Capecchi, S. Cavalli, D. De Fazio, A. Aguilar, X. Giménez, and J. Lucas, MOLECULAR PHYSICS **98**, 1835 (2000).

[71] H. J. Werner, P. J. Knowles, G. Knizia, F. R. Manby, and M. Schütz et al., "Molpro, version 2018.1," (2018), a package of ab initio programs (2018), see https://www.molpro.net.

[72] V. P. Majety, A. Zielinski, and A. Scrinzi, J. Phys. B: At. Mol. Opt. Phys. **17**, 063002 (2015).

[73] V. P. Majety and A. Scrinzi, J. Phys. B: At. Mol. Opt. Phys. **48** (2015), 10.1088/0953-4075/48/24/245603.

[74] P. S. I. S. R. M. P. H. Lischka, T. Müller and R. Shepard, WIREs Comput. Mol. Sci. **1** (2011), 10.1002/wcms.25.

[75] R. Y. Rubinstein and D. P. Froese, *Simulation and the Monte Carlo Method*, 3rd ed. (Wiley, New Jersey, 2016).

[76] N. B. Delone and V. P. Krainov, J. Opt. Soc. Am. B **8**, 1207 (1991).

[77] N. B. Delone and V. P. Krainov, Phys.-Uspekhi **41**, 469 (1998).

[78] L. Fechner, N. Camus, J. Ullrich, T. Pfeifer, and R. Moshammer, Phys. Rev. Lett. **112**, 213001 (2014).

[79] A. Chen, C. Lazarou, H. Price, and A. Emmanouilidou, J. Phys. B: At. Mol. Opt. Phys. **49**, 235001 (2016).

[80] H. Niikura, F. Légaré, R. Hasbani, A. D. Bandrauk, M. Y. Ivanov, D. M. Villeneuve, and P. B. Corkum, Nature **417**, 917 (2002).

[81] T. Zuo and A. D. Bandrauk, Phys. Rev. A **52**, R2511(R) (1995).

[82] T. Seideman, M. Y. Ivanov, and P. B. Corkum, Phys. Rev. Lett. **75**, 2819 (1995).

[83] D. M. Villeneuve, M. Y. Ivanov, and P. B. Corkum, Phys. Rev. A **54**, 736 (1996).

[84] E. Dehghanian, A. D. Bandrauk, and G. L. Kamta, Phys. Rev. A **81**, 061403(R) (2010).

[85] D. C. Heggie, Celest. Mech. **10**, 217 (1974).

[86] G. P. Katsoulis, M. B. Peters, A. Staudte, R. Bhardwaj, and A. Emmanouilidou, Phys. Rev. A **103**, 033115 (2021).

[87] J. G. Leopold and I. C. Percival, J. Phys. B: At. Mol. Opt. Phys. **12**, 709 (1979).

[88] C. L. Kirschbaum and L. Wilets, Phys. Rev. A **21**, 834 (1980).

[89] J. Guo and X.-S. Liu, Phys. Rev. A **78**, 013401 (2008).

[90] P. J. Ho and J. H. Eberly, Opt. Express **15**, 1845 (2007).

[91] J. S. Prauzner-Bechcicki, D. K. Efimov, M. Mandrysz, and J. Zakrzewski, J. Phys. B: At. Mol. Opt. Phys. **54**, 114001 (2021).

[92] A. Emmanouilidou and J. M. Rost, J. Phys. B: At. Mol. Opt. Phys. **39**, 4037 (2006).

[93] A. Emmanouilidou, P. Wang, and J. M. Rost, Phys. Rev. Lett. **100**, 063002 (2008).

[94] J. Colgan and M. S. Pindzola, Phys. Rev. Lett. **108**, 053001 (2012).

[95] J. Colgan, A. Emmanouilidou, and M. S. Pindzola, Phys. Rev. Lett. **110**, 063001 (2013).

[96] J. S. Cohen, Phys. Rev. A **51**, 266 (1995).

[97] J. S. Cohen, Phys. Rev. A **54**, 573 (1996).

[98] V. J. Montemayor and G. Schiwietz, Phys. Rev. A **40**, 6223 (1989).

[99] L. Sarkadi, Phys. Rev. A **103**, 053113 (2021).

[100] D. F. Ye, X. Liu, and J. Liu, Phys. Rev. Lett. **101**, 233003 (2008).

[101] D. H. Kobe and K.-H. Yang, Europ. J. Phys. **8**, 236 (1987).

[102] E. Yakaboylu, M. l. Klaiber, H. Bauke, K. Z. Hatsagortsyan, and C. H. Keitel, Phys. Rev. A **88**, 063421 (2013).

[103] P. Pihajoki, Celest. Mech. Dyn. Astron. **121**, 211 (2015).

[104] L. Liu, X. Wu, G. Huang, and F. Liu, Mon. Not. R. Astron. Soc. **459**, 1968 (2016).

[105] W. H. Press, S. A. Teukolsky, W. T. Vetterling, and B. P. Flannery, *Numerical recipes: The Art of Scientific Computing*, 3rd ed. (Cambridge University Press, Cambridge, 2007).

[106] R. Bulirsch and J. Stoer, Numer. Math. **8**, 1 (1966).

[107] L. D. Landau and E. M. Lifshitz, *Quantum Mechanics: Non-Relativistic Theory*, 2nd ed. (Pergamon, Oxford, 1965).

[108] X. M. Tong, Z. X. Zhao, and C. D. Lin, Phys. Rev. A **66**, 033402 (2002).

[109] B. HuP, J. Liu, and S.-G. Chen, Phys. Lett. A **236**, 533 (1997).

[110] Y. Zhou, C. Huang, Q. L., and P. Lu, Phys. Rev. Lett. **109**, 053004 (2012).

[111] Y. Zhou, Q. Zhang, C. Huang, and P. Lu, Phys. Rev. A **86**, 043427 (2012).

[112] A. Tong, Y. Zhou, and P. Lu, Opt. Express **23**, 15774 (2015).

[113] C. O. Reinhold and C. A. Falcón, Phys. Rev. A **33**, 3859 (1986).

[114] A. l'Huillier, L. A. Lompre, G. Mainfray, and C. Manus, Phys. Rev. A **27**, 2503 (1983).

[115] P. Wang, A. M. Sayler, K. D. Carnes, B. D. Esry, and I. Ben-Itzhak, Opt. Lett. **30**, 664 (2005).

[116] X. M. Tong and C. D. Lin, J. Phys. B: At. Mol. Opt. Phys **38**, 2593 (2005).

[117] C. T. L. Smeenk, L. Arissian, B. Zhou, A. Mysyrowicz, D. M. Villeneuve, A. Staudte, and P. B. Corkum, Phys. Rev. Lett. **106**, 193002 (2011).

[118] A. Ludwig, J. Maurer, B. W. Mayer, C. R. Phillips, L. Gallmann, and U. Keller, Phys. Rev. Lett. **113**, 243001 (2014).

[119] S. Chelkowski, A. D. Bandrauk, and P. B. Corkum, Phys. Rev. Lett. **113**, 263005 (2014).

[120] B. Wolter, M. G. Pullen, M. Baudisch, M. Sclafani, M. Hemmer, A. Senftleben, C. D. Schröter, J. Ullrich, R. Moshammer, and J. Biegert, Phys. Rev. X **5**, 021034 (2015).

[121] B. Willenberg, J. Maurer, B. W. Mayer, and U. Keller, Nat. Commun. **10**, 5548 (2019).

[122] F. Sun, X. Chen, W. Zhang, J. Qiang, H. Li, P. Lu, X. Gong, Q. Ji, K. Lin, H. Li, J. Tong, F. Chen, C. Ruiz, J. Wu, and F. He, Phys. Rev. A **101**, 021402(R) (2020).

[123] K. Lin, S. Brennecke, H. Ni, X. Chen, A. Hartung, D. Trabert, K. Fehre, J. Rist, X.-M. Tong, J. Burgdörfer, L. P. H. Schmidt, M. S. Schöffler, T. Jahnke, M. Kunitski, F. He, M. Lein, S. Eckart, and R. Dörner, Phys. Rev. Lett. **128**, 023201 (2022).

[124] K. Lin, X. Chen, S. Eckart, H. Jiang, A. Hartung, D. Trabert, K. Fehre, J. Rist, L. P. H. Schmidt, M. S. Schöffler, T. Jahnke, M. Kunitski, F. He, and R. Dörner, Phys. Rev. Lett. **128**, 113201 (2022).

[125] A. Hartung, S. Eckart, S. Brennecke, J. Rist, D. Trabert, K. Fehre, M. Richter, H. Sann, S. Zeller, K. Henrichs, G. Kastirke, J. Hoehl, A. Kalinin, M. S. Schöffler, T. Jahnke, L. P. H. Schmidt, M. Lein, M. Kunitski, and R. Dörner, Nat. Phys. **15**, 1222 (2019).

[126] S. Chelkowski, A. D. Bandrauk, and P. B. Corkum, Phys. Rev. A **92**, 051401(R) (2015).

[127] S. Brennecke and M. Lein, J. Phys. B: At. Mol. Opt. Phys **51**, 094005 (2018).

[128] M. Abramowitz and I. Stegun, *Handbook of Mathematical Functions: With Formulas, Graphs, and Mathematical Tables*, Applied mathematics series (Dover Publications, 1965).

[129] C. Z. Bisgaard and L. B. Madsen, Am. J. Phys **72**, 249 (2004).